The Behaviour of Fibre Reinforced Concrete (SHCC) under Biaxial Compression and Tension

By

Willie Swanepoel

UNIVERSITEIT • STELLENBOSCH • UNIVERSITY

Thesis presented in partial fulfilment of the requirements for the degree of Master of Science (Structural Engineering) at the University of Stellenbosch.

Project Leader: Prof G.P.A.G van Zijl

December 2011

Declaration

By submitting this thesis electronically, I declare that the entirety of the work contained therein is my own, original work, that I am the owner of the copyright thereof (unless to the extent explicitly otherwise stated) and that I have not previously in its entirety or in part submitted it for obtaining any qualification.

Date: .....

Abstract

Strain hardening cement-based composites (SHCC) are fibre-reinforced composites designed to form multiple fine cracks under tensile and flexural load. The cracks are controlled to small widths, whereby significant toughness, or energy dissipation, is realised on the one hand, and high resistance to gas and liquid ingress is maintained on the other hand. These two physical phenomena define application fields of SHCC, i.e. for instance elements of buildings and infrastructure for enhanced earthquake resistance, and protection of steel bars under service loads which lead to crack formation. Also exploiting the potential protection offered by SHCC to existing structures, thin overlays have been applied to existing dam faces, reinforced concrete retaining walls, water channels and RC road pavements. The layers vary between 20 and 40 mm in thickness. Considering the fibre length, usually 8 or 12 mm, as well as the application method, such thin layers may have dominantly two dimensional fibre orientation, with little or no component in the layer thickness direction. While several research groups have performed uniaxial tensile tests and flexural tests on SHCC specimens, little or no information is available on SHCC response to biaxial loading, as is to be expected in road pavement repair layers, or other repair layers. This paper reports the results of biaxial testing of 20 mm thick SHCC specimens produced in such a way to have dominantly two-dimensional fibre orientation, and another group of specimens produced by cutting from larger specimens, whereby three-dimensional fibre orientation was preserved in the resulting 20 mm thick specimens. Biaxial tests were performed in three quadrants, i.e. compression-compression, compression-tension, and tension-tension. A clear fibre orientation-related difference in the failure patterns involves out-of-plane splitting under biaxial compression of specimens with two-dimensional fibre orientation, at significantly lower load, as opposed to in-plane tensile splitting of specimens containing three-dimensional fibre orientation.

Abstrak

Vervormingsverhardende sement-gebaseerde saamgestelde materiale (SHCC) is veselversterke saamgestelde materiale wat ontwerp is om verskeie fyn krakies te vorm onder trekspanning en buig spanning. Die kraakbreedtes word beheer, waardeur betekenisvolle taaiheid verkry, of energie verlies beheer word aan die een kant, en die hoë weerstand teen die gas en die vloeistof penetrasie aan die ander kant gehandhaaf word. Hierdie twee fisiese verskynsels definieer die toepassingsvelde van SHCC, d.w.s vir byvoorbeeld elemente van geboue en infrastruktuur vir verbeterde aardbewing weerstand, en die beskerming van staal stawe onder die dienslaste wat lei vorming te kraak. By eksploitasie van die potensiële beskerming aangebied deur SHCC aan bestaande strukture, is dun oorlae op bestaande dam walle, versterkte beton keermure, water kanale en staal-versterkte beton paaie gebruik. Die SHCC lae wissel tussen 20 en 40 mm in dikte. Met inagneming van die vesel lengte, gewoonlik 8 of 12 mm, sowel as die toepassingsmetode, kan so 'n dun lag ‘n oorheersend tweedimensionele vesel oriëntasie hê, met min of geen komponent in die rigting van die laag dikte nie. Terwyl verskeie navorsingsgroepe eenassige trektoetse en buigtoetse op SHCC monsters gedoen het; is daar min of geen inligting beskikbaar op SHCC se reaksie op biaksiale belasting, soos verwag kan word in die pad herstel lae, of ander herstel lae. Hierdie verslag rapporteer die resultate van die biaksiale toetsing van 20 mm dik SHCC monsters wat op so 'n manier gemaak word om dominante twee-dimensionele vesel oriëntasie te he, en 'n ander groep monsters wat deur die sny van groter monsters, waarvolgens die drie-dimensionele vesel oriëntasie verseker is. Biaksiale toetse is uitgevoer in drie kwadrante, d.w.s druk-druk, druk-trek en trek-trek. 'n Duidelike verskil in die falingspatrone, aan die hand van vesel oriëntasie, behels uit-vlak splyting onder biaksiale toetsing van monsters met twee-dimensionele vesel oriëntasie, op 'n aansienlik laer lading, in teenstelling met die in-vlak trek splyting van monsters wat ‘n drie-dimensionele vesel oriëntasie het.

Acknowledgements

Sika South Africa (Pty) Ltd for their kind contribution of epoxy resin solutions.

Dion Viljoen and Johan van der Merwe for their assistance in building the biaxial setup.

My family, for all their support and prayers throughout the project.

Table of Contents

List of Figures

List of Tables

Nomenclature

SHCC – Strain hardening cement composite

FRC – Fibre reinforced concrete

ITZ – Interfacial transition zone

V_f^{crit} – Critical volume of fibres

PVA – Polyvinyl alcohol

1. Introduction

Much information regarding failure of advanced concrete materials under biaxial and triaxial states of stress is still desired. This research will focus on a particular kind of fibre reinforced concrete, strain hardening cement composite, SHCC. The material will be tested biaxially in order to investigate its stress-strain behaviour as well as its failure behaviour. The study of the biaxial behaviour of concrete is necessitated by effects noticed in practice, which include confinement-induced increased resistance, potential reduced resistance in compression-tension, and in particular in SHCC, large deformation associated with multiple crack formation.

The confinement effect occurs for instance in the region of the bond between rebar and concrete (Coulomb-frictional behaviour), and in concrete confined by shear links, as accounted for in shear wall design. The confinement effect leads to increased resistance in 2D and 3D compressive stress states. Practical examples of these stress states would be structures in the sea (hydrostatic), suspended slabs (floors) and slabs used as pavements (dominantly biaxial). Another important yet simple reason for the research is simply to accurately define the behaviour to enable the definition of failure limit surfaces for computer models.

More complex structures are constructed using concrete and high strength concrete in particular. Due to the complicated nature of the structural shape, the design and analysis of such structures necessitates the use of finite element analysis. The use of the finite element method, however, requires a thorough understanding of the material in use (Hussein and Marzouk, 2000).

As there are numerous differences between normal concrete and SHCC's, these differences must be quantified and understood to enable the correct and effective use of the material. The most important aspects include elasticity, Poisson's ratio, failure behaviour and mechanisms, ductility and post peak-stress behaviour.

The addition of fibres in the concrete mix plays a significant role in the limitation of and prevention of micro cracks which form during setting (Illston and Domone, 2001) and under imposed strain. In SHCC not only setting cracks are arrested, but also those that arise due to mechanical load. These fibres extend across these cracks and thus add to the capacity of the concrete by extending the time and strain level to which the concrete can carry a specific load. The problem herein is however, that this fibre reinforced concrete (FRC) will behave differently to standard concrete, subjected to stresses, due to

inherently different material properties, especially when submitted to tension-dominated loading. The aim of this research would then be to investigate failure under biaxial tension and compression loading, and hence propose a model for failure.

Investigation into compression behaviour of SHCC and the effects of loading platens yielded interesting results and conclusions such as failure mechanisms caused, for example. This research project is the continuation thereof and the completion of the so called failure envelope of SHCC. Below, Figure 1, the result of above mentioned investigation.

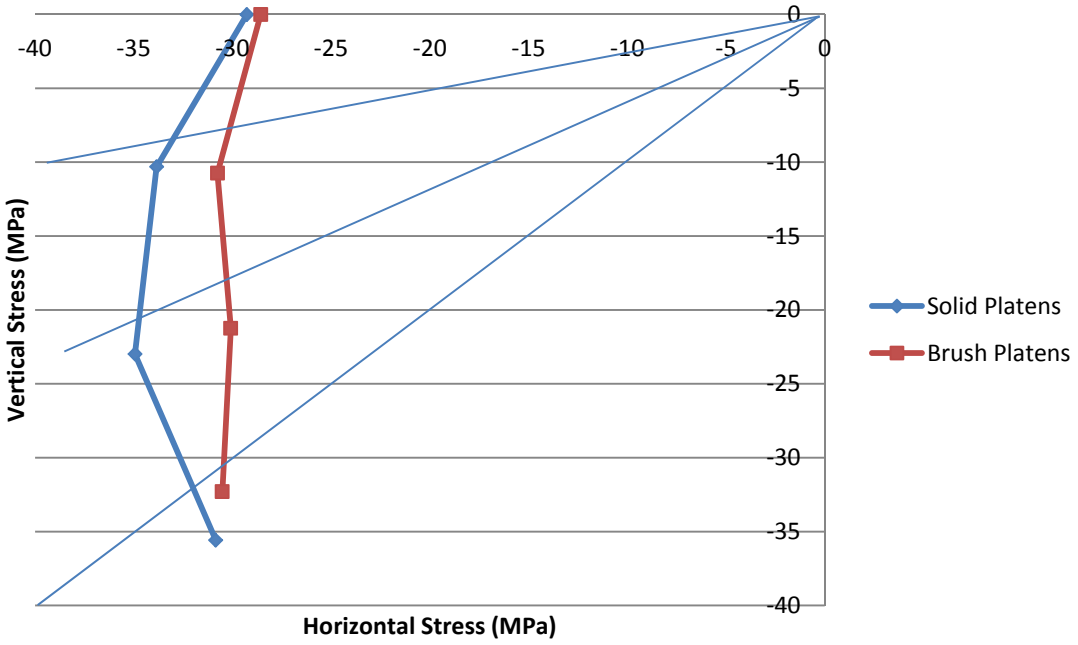

Figure 1 - Biaxial failure envelope for 3rd quadrant, symmetry assumed about the 45° line

The primary goal of this research project is the completion of the failure envelope for SHCC, using improved methods and procedures. This means testing for ratios of compression and tension, as opposed to only compression as in Figure 1.

A 45° line of symmetry, in the failure envelope, will be assumed and thus testing regimes will be within three of the four quadrants. This assumption is not uncommon to this field of study and has been used by other authors as well, refer to Figure 2.

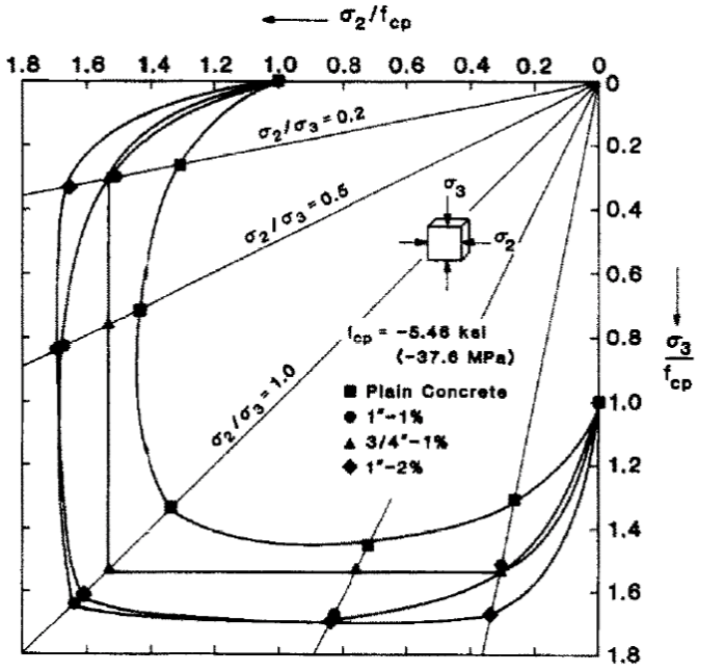

Figure 2 - Symmetrical biaxial failure envelope (Yin et al. 1990)

A significant difference in the failure curve that is determined by this research with the one by Yin et al., and that of Figure 1, is that tension testing will be included, which implies that the curve will not only occupy the 3rd quadrant, but the 1st, 3rd and 4th quadrants.

The loading scheme that will be followed for this research ranges from 45° - 235°. This includes zones of tension-tension, compression-tension and compression-compression. The loading ratios are applied as ratios of σ_2/σ_1. With $\sigma_2/\sigma_1 = 0$ (uniaxial compression) and $\sigma_2/\sigma_1 = \infty$ (uniaxial tension). This method will enable one to define the generalised biaxial response, and find the ratio which yields the maximum biaxial stress. Figure 3 shows the loading scheme mentioned above.

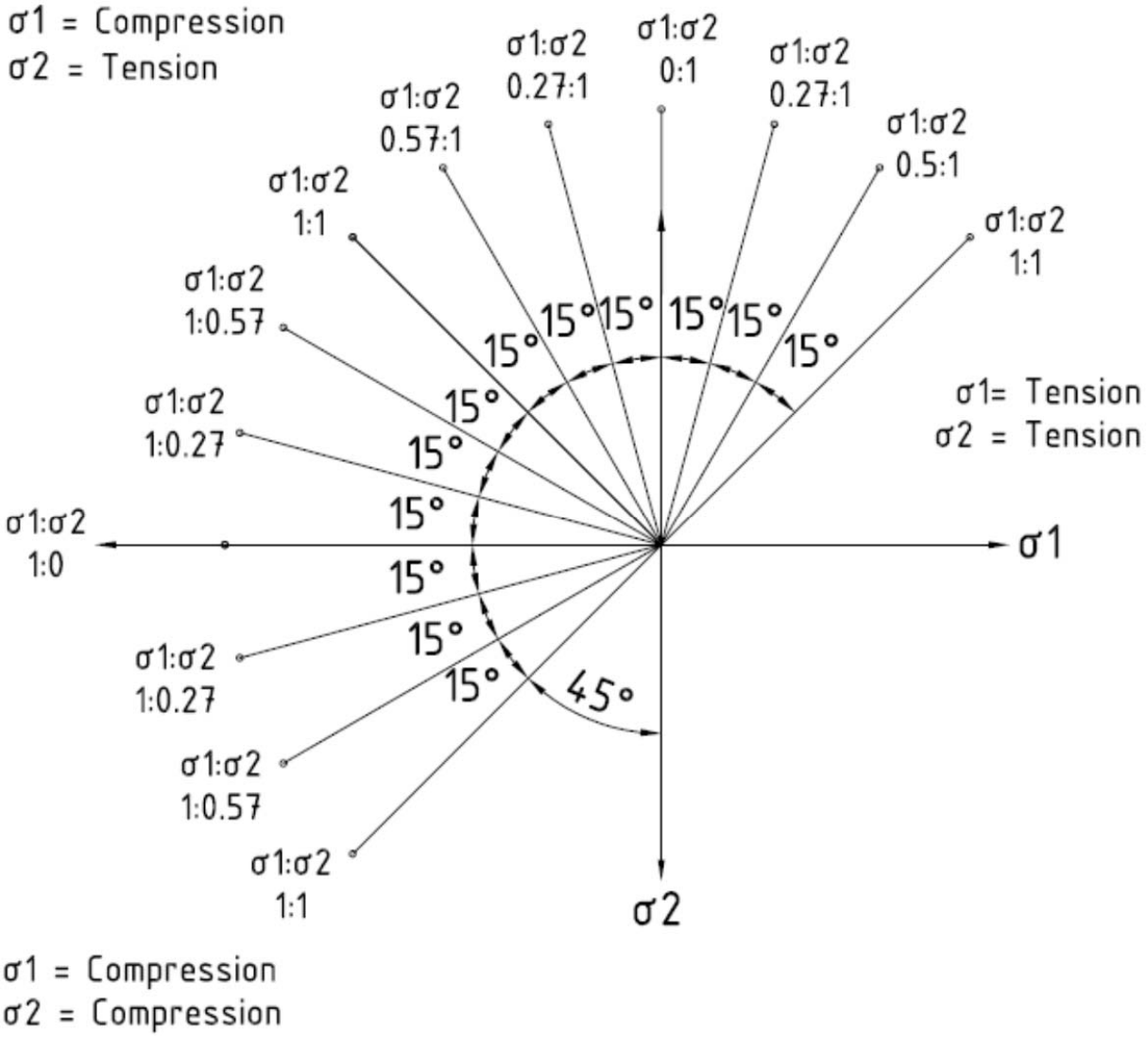

Figure 3 - Loading Scheme for the biaxial testing of SHCC (tension and compression)

2. Literature Survey

2.1.FRC Characteristics and Classification

Recently, many developments have been made towards the understanding and classification of FRC materials and various materials have thus been introduced. SHCC or strain-hardening cement-composites have been developed not for high strength, like ultra high-performance fibre-reinforced concrete (UHPFRC), but for crack control, ductility and energy dissipation. The appropriate use thereof requires that that particular criteria for strength, ductility and durability must be met (Van Zijl & Boshoff, 2008).

The use of FRC is becoming more popular as a result of the current trend of increased structural member size, prefabrication and the potential reduction of rebar in concrete members. What also makes it attractive is that it has become possible, through more thorough understanding, to design tailor made FRC's for specific purposes (Van Zijl & Boshoff, 2008).

The tensile strength and ductility properties of FRC could be exploited by the design engineer, bearing in mind that the material was initially introduced as a solution to tensile strength and brittleness problems. It is now possible to design SHCC's with moderate tensile and compressive strength but significant ductility (up to and beyond 3% of tensile strain). Figure 4 shows the increased tensile strain of two SHCC's in uniaxial tension compared to an UHPFRC (Van Zijl & Boshoff, 2008).

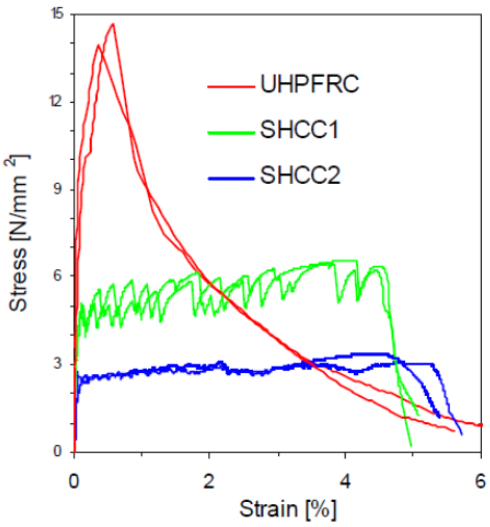

Figure 4 - SHCC and UHPFRC Uniaxial Tensile Behaviour (Van Zijl & Boshoff, 2008)

Naaman & Reinhardt (2006) have recently proposed a useful classification of FRC. The proposal is based on tensile strength classes, much like compressive strength classes of normal concrete, but with a minimum tensile strain of 0.5% at full tensile resistance. This then defines a pragmatic tensile strain capacity which is based on an average strain level in steel bar reinforced flexural members for which these FRC's are intended. This classification has been criticized as these members may not be required to operate in the non-linear regime, meaning that such a high tensile capacity is not necessary (Van Zijl & Boshoff, 2008).

Figure 5 shows the abovementioned classification of FRC along with a simplified bilinear tension model for FRC.

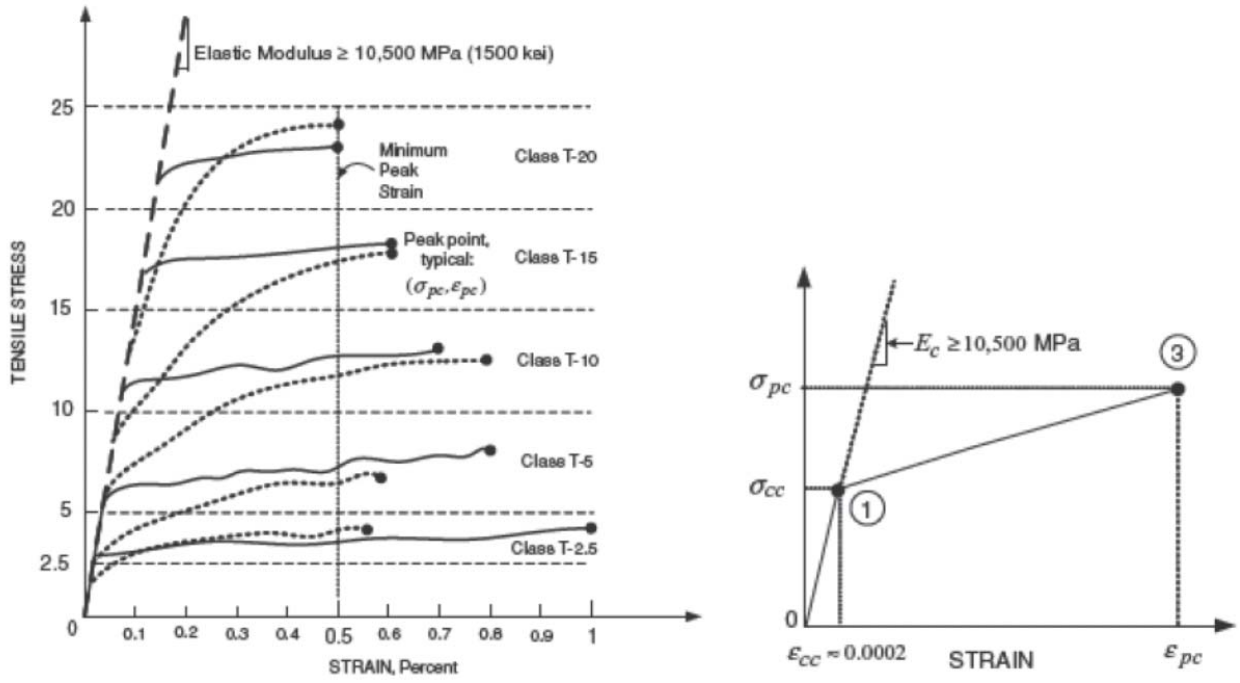

Figure 5 - FRC (a) Classification and (b) Simplified Bilinear Tension Model (Naaman & Reinhardt, 2006).

2.2. Structural Nature of Cement-Based Fibre Reinforced Materials

A composite material cannot simply be described without a thorough and complete understanding of its constituents. One should know exactly what constituents are included in the composite, how they all react to loading and what influence, if any, they have on the loading response of the composite. According to several authors, eg Li et al. (2001) and Bentur & Mindess (2007), the properties of fibre reinforced concrete are dependent on three components, namely:

2.2.1. The Structure of the Bulk Cementitious Matrix

The matrix could be divided into two types: paste (cement/sand and water mix) and concrete (cement-sand-coarse aggregate-water mix), depending on the aggregate contained. Discrete cement particles with diameter in the order of 1-100µm (average size of about 10µm) are found in the matrixe, which upon hydration form mostly colloidal Calsium silicate hydrate (CSH, abbreviated from $C_3S_2H_3$) particles and larger Calsium hydroxide (CH, abbreviated from Ca(OH)2) crystals. CSH provides most of the strength of the concrete and CH raises the pH of the pore water but does not contribute to the strength (Addis, 2007).

2.2.2. The Orientation and Distribution of the Fibres

The distribution of the fibres in the matrix will influence the strength of the hardened composite drastically. The PVA fibres used form a fibre assembly, made up of bundles of fibres or filaments. This formation is common with man-made fibres. If the ratio of fibre length to thickness of the composite is sufficiently large, the fibres will assume a predominantly 2D distribution, a matter discussed in depth in this research. The uniformity of the fibres position in the composite is sensitive to the mixing, production and consolidation process. A uniform distribution is rarely achieved in practice (eg. Bentur & Mindess, 2007), but careful design and manufacture can overcome this (eg. Van Zijl & Boshoff, 2008)

Fibre reinforced cement pastes are usually used for thin sheet applications and the fibre content is usually about 1-15% of the mix volume, with the most recent trend in using moderate to low (1% to 3%) fibre contents. Such a thin sheet application is investigated as a thin-cast specimen in this research. The amount of fibres per volume plays an important role as this will affect the rheology and the microstructure of the composite, but importantly, the post-cracking behaviour of the hardened composite.

2.2.3. The Structure of the Fibre-Matrix Interface

Whereas the ITZ in concrete is dominantly between course aggregate particles and the hardened cement paste (hcp), FRC has an additional ITZ region, namely between the fibres and the hcp. In this zone the microstructure of the paste is significantly different from the rest of the bulk paste matrix in the body, away from any fibres. The extent and nature of the zone depends on the matrix composition, the fibre type and the method of concrete production.

Failure may be initiated in the direct interface, i.e. the ITZ, (adhesive failure) or, in cases of weakness in the surrounding matrix, further away in the interfacial zone (cohesive failure) (Gao Song, 2004). Cohesive failure is initiated by the porous layer rather than the interface itself. The changing nature of concrete due to the continuous hydration is, in part, the cause of embrittlement in some FRC with time, due to the strengthening of the interfacial zone, whereby fibres may not be pulled out, but break in brittle fashion (Illston & Domone, 2001).

Considering the interactions between the cement-matrix and the fibre after setting and hardening of the concrete, the adhesion and frictional influence by the fibres is greatly increased when the fibres have a high surface to volume area. This is the case for PVA fibres, as they are synthetic micro-fibres. This means that PVA fibres may be susceptible to cause the abovementioned, undesired, brittle fracture, if the matrix becomes too strong or tough (Li et al. 1995; Bentur & Mindess, 2007).

Fibre pull-out is enabled for PVA fibres as the fibres are specially treated (chemical modification) so as to reduce the strong bond with the matrix. The modification is motivated by the superior composite behaviour due to pull out rather than fibre breakage due to the high natural bond (Li et al., 1995). Refer to Section 2.5, SHCC characteristics for more information on the fibres and fracture and a likely failure mode.

2.3. Change in Mechanical Response of Concrete by the Addition of Fibres

Consider Figure 6; in order for fibre addition to successfully modify the mechanical behaviour of the hardened concrete, it is required that the composite tensile response matches that of response B in Figure 6. This requires that the fibres must be able to bridge a crack and in doing so, effectively transfer the cracking force (Van Zijl & Boshoff, 2008). This transfer is only possible with a minimum volume of fibres, given by

$$V_f^{crit} = \frac{\sigma_{cr}}{\sigma_{fu}}, \qquad [1]$$

Eq. (1) has been derived from simple equilibrium across a crack. In eq. [1], σ_{cr} is the composite cracking stress and σ_{fu} is the fibre strength or pull-out resistance. For eq. [1] to guarantee strain hardening response and the formation of multiple, rather than one large single crack, the fibre resistance must be mobilised at the same strain level as the matrix, at $\sigma_{cr.}$. If the difference in E modulus between the matrix and the fibre is too great, i.e. the fibre E modulus is much lower, then a significant strain increase would be required of the fibres to reach the composite cracking stress (dashed line XB), this response is accompanied by a single wide open crack, the undesired response (Van Zijl & Boshoff, 2008).

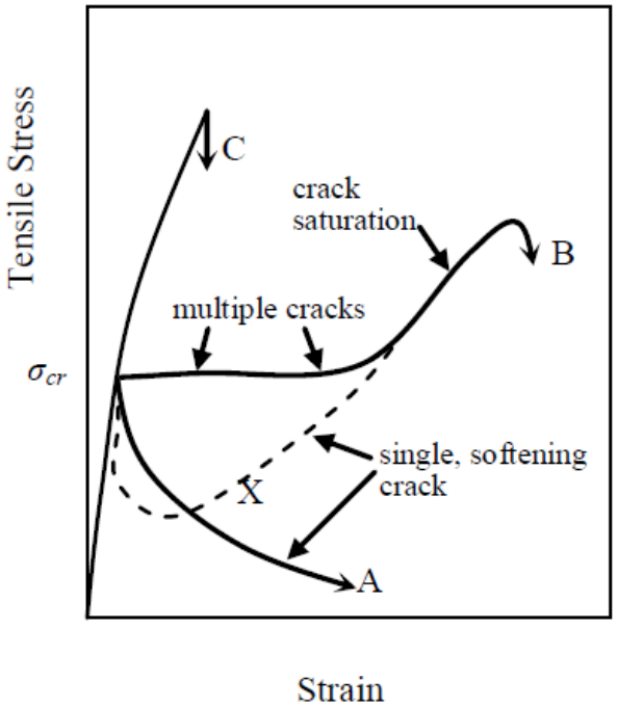

Figure 6 - Uniaxial Tensile Behaviour of FRC (Van Zijl & Boshoff, 2008)

2.4. Biaxial Behaviour of Cement-Based Materials

In concrete, the state of stress experienced within the material is not merely uniaxial, but multi-axial. This can result in considerable modifications to the failure stresses, primarily by influencing the cracking pattern (Illston & Domone, 2006). Research indicates an increase in compressive strength of biaxially tested concrete as compared to uniaxially tested concrete, which hints at the idea that the use of concrete in structural design may be subjected to conservative, over-design if design parameters are found from uniaxial tests. Note that this is for compression, while for tension, equal or reduced tensile resistance is usually accounted for under conditions for biaxial tension-tension, and compression-tension in computational models.

2.4.1. Biaxial Behaviour of FRC and the Confinement Effect

Assume that a biaxial state of stress is applied to a specimen, with the two orthogonal stresses being referred to as σ_1 and σ_2. Research shows that there is a significant increase in compressive biaxial strength due to the addition of fibres, (Yin et al., 1990). Under biaxial loading, the fibres reinforce the material in the out of plane direction which causes an amount of compressive stress in this unloaded direction.

This "compressive stress" is aptly referred to as the confinement effect or the confinement stress (σ_3, i.e. the third principal direction). This stress state thus implies a triaxial state of stress as a result of the applied biaxial stress state. Van Mier (1984) demonstrated by triaxial compression testing, by applying a very small compressive load in the third direction (about 5-10% of principal stress), that a biaxial stress ratio of $\sigma_2/\sigma_1 = 0.2$, by analogy, had a 35% increase in biaxial compressive strength for the specific concrete. Such an increase in strength was found to be equivalent to an out of plane stress of only about 3.5% of the major stress σ_1 (Yin et al., 1990).

It was proposed that this small out-of-plane stress could conceivably be supplied passively by the added steel fibres. Murugappan et al. (1993) reported that steel fibres provide an "equivalent confining pressure" which acts perpendicular to the applied stress plane. This out of plane stress had only to be in the order of 5% to cause an increase of about 40% in biaxial strength. It was proposed that the strength envelope for FRC under a biaxial stress state is equivalent to the failure envelope for an analogous plain concrete under triaxial compression (Hu et al, 2003). These statements regarding biaxial loading and the effect of the fibres would imply that this confinement pressure is large enough to be assumed as the third principal stress.

2.4.2. The Confinement Effect and the Euro-Code Design Standard

The confinement effect is undeniably a phenomenon which deserves attention in the design of elements. The Euro-Code states that, "confinement of concrete results in a modification of the effective stress-strain relationship: higher strength and higher critical strains are achieved." In reinforced concrete this confinement can be brought about or generated by adequately closely spaced links or cross ties (BS EN 1992-1-1, 2004).

The code also provides equations, [2]-[5], which can be used to calculate the confined characteristic strength ($f_{ck,c}$) and strains ($\varepsilon_{c2,c}$, $\varepsilon_{cu2,c}$). Refer to Figure 7 for stress-strain relationships and Appendix A for parameters used in equations. It should be noted that f_{ck} is the characteristic cylinder strength.

$$f_{ck,c} = f_{ck}\left(1.0 + 5.0\,{}^{\sigma_2}/_{f_{ck}}\right) \; for\; \sigma_2 \leq 0.05 f_{ck} \qquad [2]$$

$$f_{ck,c} = f_{ck}\left(1.125 + 2.50\,{}^{\sigma_2}/_{f_{ck}}\right) \; for\; \sigma_2 \geq 0.05 f_{ck} \qquad [3]$$

$$\varepsilon_{c2,c} = \varepsilon_{c2}\left({}^{f_{ck,c}}/_{f_{ck}}\right)^2 \qquad [4]$$

$$\varepsilon_{cu2,c} = \varepsilon_{cu2} + 0.2\,{}^{\sigma_2}/_{f_{ck}} \qquad [5]$$

Where σ_2 (=σ_3) is the effective lateral compressive stress at the ultimate limit state due to confinement and ε_{c2} and ε_{cu2} follow from Table 3.1, Appendix A.

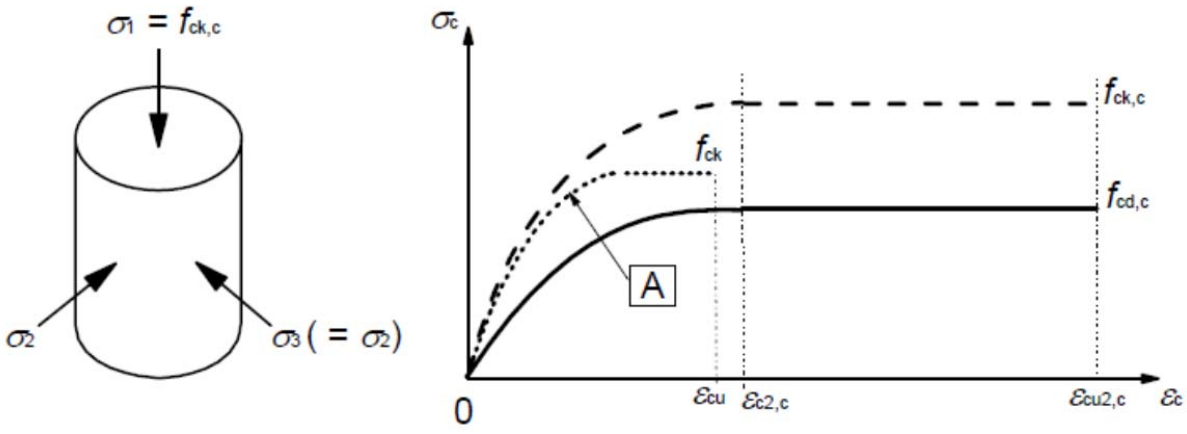

Figure 7 - Stress-Strain Relationship for Confined Concrete (Curve A - Unconfined) (BS EN 1992-1-1, 2004)

This allows the designer to calculate the increased characteristic stress in a member, provided that the characteristic strength and the confining or out of plane stress is known. The result is then that a member could be designed less conservatively, thus saving on material costs.

It should be noted that the code makes specific mention that for design, the other basic material characteristics may be considered as unaffected.

2.5. Strain Hardening Cement Composite (SHCC) Characteristics

2.5.1. PVA Fibre Characteristics

For this research, Polyvinyl Alcohol fibres are used. Of importance to the reader is the interface between these fibres and the concrete matrix and the reader should be aware that there are difficulties to overcome in order to use these fibres successfully, refer to discussion in Section 2.2. Illston & Domone (2001) summarise typical properties of cement-based matrices and fibres, this table is regenerated in Table 1. See the last row in Table 1 for properties of the PVA fibres used in this study.

Table 1 - Typical Properties of cement based matrices and fibres, Illston & Domone (2001)

Material or fibre	Relative density	Length (mm)	Elastic Modulus (GPa)	Tensile strength (MPa)	Failure strain (%)	Volume in composite (%)
Concrete matrix	1.8 – 2.0	-	10 - 30	1 - 10	0.01 – 0.05	97
PVA	1 - 3	12	12 - 40	700 - 1500	6 - 13*	3
PVA (Kuraray)	*	12	40	1600	*	2

*http://www.kuraray.co.jp/kii/english/

It is important to notice, from Table 1, the difference in strength of the PVA fibres in relation to the concrete matrix. The differences in failure strain also hint at the fact that the concrete will fail before the fibres do. A point to consider is that when a fibre is stretched along its axis, it will contract radially. This leads to high lateral tensile stresses at the fibre-matrix interface, which might cause the fibre, which is short and of circular section, to delaminate and pull out (Illston & Domone, 2001). Delamination of the PVA fibres used in this study is more likely to occur as a result of the significant elongation it undergoes at a crack to enable stress transfer across the crack.

High strength fibres were developed, originally, primarily for the replacement of asbestos fibres, as the use of asbestos is known to be extremely harmful. The fibre surface is treated to enhance its compatibility with the concrete matrix and to enable efficient dispersion. Both properties are of great importance to the successful use of the fibre. This surface treatment in combination with the polymer fibre's inherent affinity for water, due to the presence of OH^- (hydroxide ion) groups, leads to both efficient dispersion and a strong bond between fibre and matrix in the hardened composite (Bentur & Mindess, 2007). PVA fibres rupture rather than pull-out of a cementitious material as a result of the strong chemical bond and the resulting slip hardening response during pull-out (Li et al., 2001; Bentur & Mindess, 2007). However, this is rectified by surface treatment. On the other hand, high modulus polyethylene (PE) fibres are prone to have too low bond with the matrix, and are treated to improve the bond (Li et al., 2001).

2.5.2. SHCC Mix Design Characteristics

The SHCC used for this study has the mix proportions given in Table 2.

Table 2 - Mix properties of SHCC

	Mass	Unit (kg/m^3)	Notes
Water	380	kg	
Cement (CEM I 42.5)	380	kg	
Fly Ash (Durapozz)	678.8	kg	
Silica Sand (Consol nr2) with maximum particle size 0.2mm	530	kg	
Fibre: PVA RECS 15, 12mm	26	kg	
Viscosity Modifying Agent	1	kg	0.075% of cement
Chryso Premia 310	1.5	kg	0.4% of cement
Total	1997.3	kg	

The concrete is designed to have a low water-to-binder ratio (w/b = 380 / (380+678.8) = 0.359). As a consequence it may behave as a self healing material. If the water to binder ratio is low, therefore there is excess binder available which may cause self healing, some SHCC's have even lower w/b ratios and do

indeed show self healing. If damage is undergone, upon wetting, the concrete can re-hydrate and in doing so regain its former strength before the deformation has occurred (Li et al., 1995). It might be that not all the fly ash acts as binder but merely as filler material, thus if all the cement has hydrated, the pozzolanic reaction will not continue.

2.5.3. Mechanical Behaviour of SHCC

As the name suggests, SHCC by definition has strain hardening tensile behaviour, which is brought about by multiple cracking. During cracking, it is crucial that steady state cracks occur, which would then let fibre pull out resistance overcome the matrix fracture toughness at the crack tip. The unstable crack growth by the successive loss of fibres through breakage is then prevented. Refer to Figure 8 where the idea of fibres successfully bridging and stabilising the crack is shown.

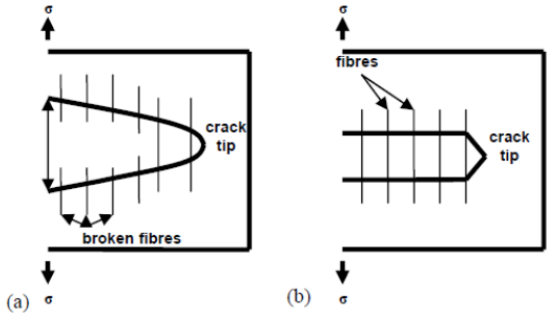

Figure 8 - (a) Griffith Type Cracking vs. (b) Steady State Cracking, Li et al. (1995)

It is this steady crack concept which has led to the development of SHCC. SHCC exhibits multiple, fine cracking under tensile deformation, see Figure 9. When deformation is increased beyond the point of first cracking, several more cracks arise successively instead of simply widening the already existing cracks. When crack saturation occurs, a short fibre pull-out phase and widening of all the cracks occurs, followed by localisation of a single crack. At this point, the fibres will then either break or pull out completely. These cracks are generally spaced at about 1-5mm and are generally restricted to less than 0.1mm in width (van Zijl & Boshoff, 2008).

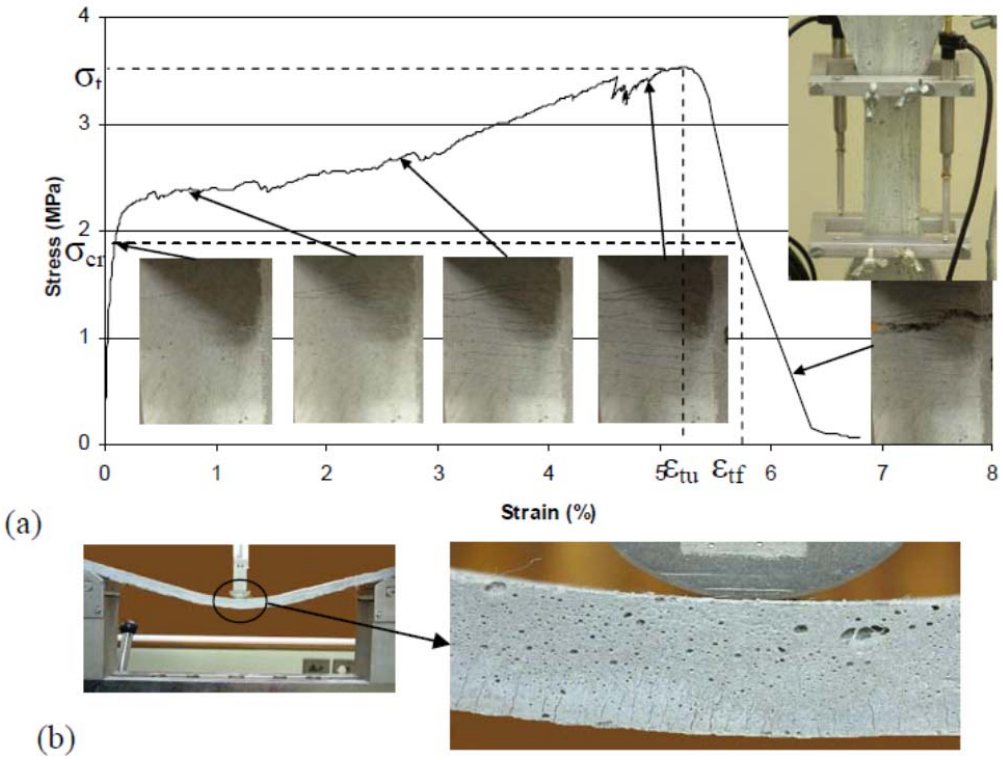

Figure 9, (a) Multiple, Fine Cracks in SHCC under (a) Tension, (b) Bending (van Zijl & Boshoff, 2008)

According to van Mier (1984), micro cracks are classified as one of three types. These cracks are 'bond-cracks' (cement-paste to aggregate interface), 'mortar-cracks' (which run through the cement-paste) and 'aggregate cracks'. No large aggregates are used in the material of this study, and it is considered unlikely that cracks will run through small sand particles. In SHCC it means that cracks are either in the paste or at the interface of paste to sand.

Microscopic cracking occurs even before the concrete has experienced any loading and then continues to increase in size and number as loading progresses. Van Mier found that these cracks start growing at about 30% of peak stress. This process continues until failure, with the strain increasing and the stress decreasing. This is known as softening. The micro cracks develop and also join up, or coalescent, eventually leading to failure. This coalescence of separate micro cracks is a major step in the rupture propagation of concrete (Van Mier, 1984).

2.5.4. Applications for SHCC

Non-structural applications of FRC include its use for large surface slabs where it controls plastic shrinkage cracking. This is actually a two-fold solution; the fibres change the consistency of the mix and bridge cracks. This application requires a rather low volume of fibres, less than 1% (van Zijl & Boshoff, 2008). Other non-structural applications include improving impact resistance and repair layers (poured or sprayed).

The structural applications include soil stabilisation, fibre boards (asbestos replacers), prefabricated formwork (extruded permanent formwork panels), bridge decks and earthquake engineering applications. An example of a PVA SHCC application is the 972m long (340m central span) Mihara Ohashi Bridge which was built in in 2004-2005 in the Hokkaido prefecture, Japan. The bridge has a composite deck consisting of a 40mm PVA SHCC upper layer, connected to a steel plate by shear connectors. A reported total of 800m^3 of SHCC was poured at 30m^3 per day, Figure 10.

Figure 10 - Mihara Ohashi SHCC-Steel Composite Bridge (Courtesy of K Rokugo, van Zijl & Boshoff, 2008)

This use of thin, high strength, continuous concrete slab pavements is currently being investigated by the South African National Roads Acency Ltd. (SANRAL) to minimise road pavement maintenance. The same application has been seen also in Europe, where UHPFRC has been used to increase bridge deck capacities through its high strength and dense mix. It has also been used for pedestrian bridge decks in Canada, New Zealand, Japan and France.

2.6. Investigation of fracture of SHCC

Thin-cast SHCC specimens were tested in biaxial compression and the failure mechanisms investigated. The broken samples were then used to explain some of the observed phenomena.

Figure 11 - Fractured biaxial compression specimen showing the fibres on the failure plane

It appears from inspection of the specimen in Figure 11, the failure mechanism seems to show a combination of brittle fracture of the concrete with pull-out of the fibres and fibre rupture.

The large number of fibres sticking out of the matrix can possibly indicate pull-out, which implies that the fibres did not exceed their failure strain but deformed elastically. This may in turn be due to a suitable matrix design enabling steady state cracking and eventual fibre pull-out, or that the concrete matrix surrounding the fibres merely crushed, enabling free pull-out from the damaged matrix. The desired evidence of fibre pull cannot be seen clearly with the naked eye as the fibre diameter and the matrix pores are in the order of tens of micro meters, so a SEM (Scanning Electron Microscope) photo analysis will be required to spot the embedment holes in the matrix, to confirm fibres pull out.

A study by Shah et al. (1999) compared PVA fibre (by Kuraray, also in this study) reinforced SHCC composites produced by extrusion to those produced by casting. They found that for casting, a longer fibre was beneficial and increased the composite tensile strength. A SEM photograph of the fibres pulled out from cast specimens suggested that the matrix to fibre bond is probably controlled by interfacial shear. This would account for the increase in strength due to the length increase of the fibres

in their testing. It was also found that 6mm fibres were longer than the critical length required for fibre pull-out (they tested 2mm and 6mm fibres) and so this lead to a greater amount of fibre fractures, at the cost of fibre pull-out. The addition of fly ash reduced the detrimental effect of the increase in length by reducing the fibre to matrix bond (including the bond as a result of surface treatment).

This would then explain why the observed fractures would seem like pull-out fractures. In the design of the mix, given in Table 2, which was done by the research group at Stellenbosch University, care was taken to ensure that ductile tensile failure occurs, by using $V_f > V_{crit}$ and a fibre-matrix combination which leads to fibre pull-out instead of fracture. The resulting failure as discussed thus appears to have achieved the mix design goals, but should be confirmed with SEM.

2.6.1. Failure Mechanisms and Effects of Fibre Orientation

Biaxial compression tests on thin cast specimens are shown in Figures 12 through 14. If the specimen in Figure 12 is inspected, one notices that a wedge formed and broke through the face of the specimen. It was noticed that some samples crack in a more defined plane parallel to the free face, meaning that the failure plane sometimes extends over the entire specimen height and length. If viewed from the sides, the wedge forms anywhere from the centre to close to the edge. See Figures 13 and 14.

Figure 12 – Biaxial compression test, showing crack pattern

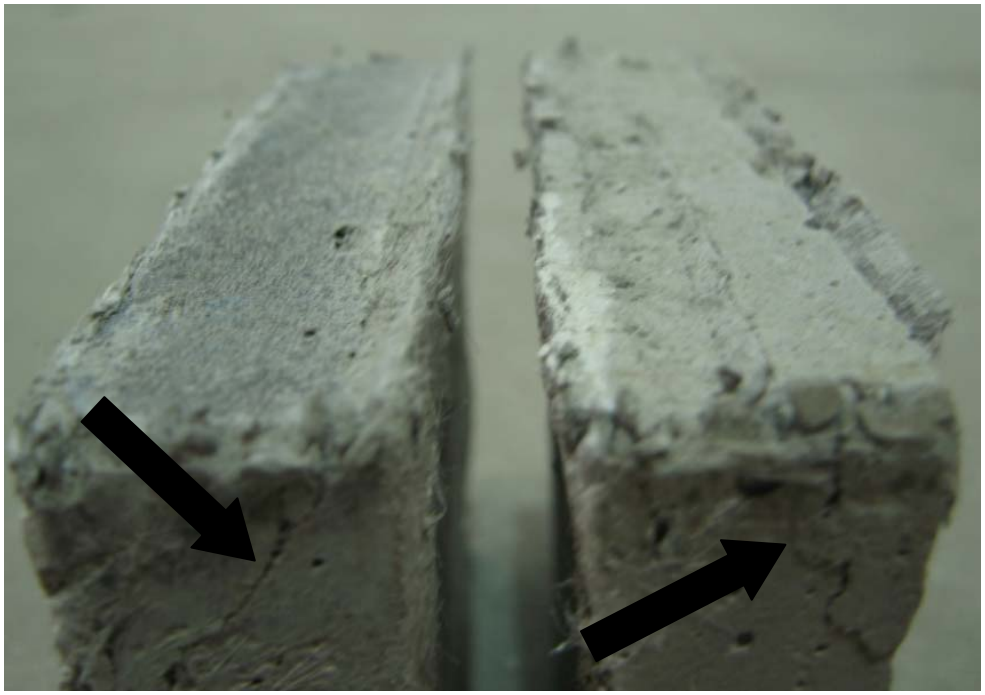

Figure 13 - Side view of specimen failure, failure plane or wedge can be seen for solid platens (left) and brush platens (right)

Figure 14 - Splitting of the test sample under biaxial load

Figure 14 shows a splitting phenomenon where the sample tends to split along a plane through the entire specimen. The reason for this splitting phenomenon can be attributed to the fact that not enough fibres were 3D orientated to prevent splitting. The fibres thus align in plane with the mould and thus very little 3D fibre orientation is present. The fibre distribution and orientation thus plays an important role in the mechanical properties of the concrete. De Koker (2004) found that fibre orientation enhances the mechanical properties of the fibre composite in the direction of the fibre

alignment. Torrenti & Djebri (1995) mention in their research that it is favourable if there are also fibres oriented perpendicular to the plane of loading, in order to prevent splitting. It should however; be noted that Yin el al. (1989) and Traina & Mansour (1991) found that failure occurred in oblique shear bands rather than fracture planes parallel to the free surface (splitting), see Figures 15 and 16.

If Figure 13 is studied, one can deduce that the oblique plane failure mode is more noticeable on the left (solid platen) than on the right (brush platen). Figure 14 then appears more like splitting than shearing at an oblique angle; this splitting mechanism can be seen more clearly as depicted in Figure 16.

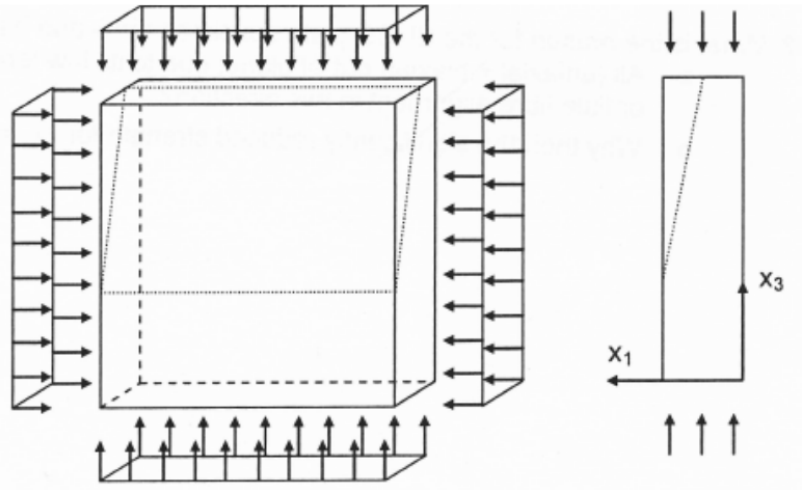

Figure 15 - Oblique shear failure planes identified

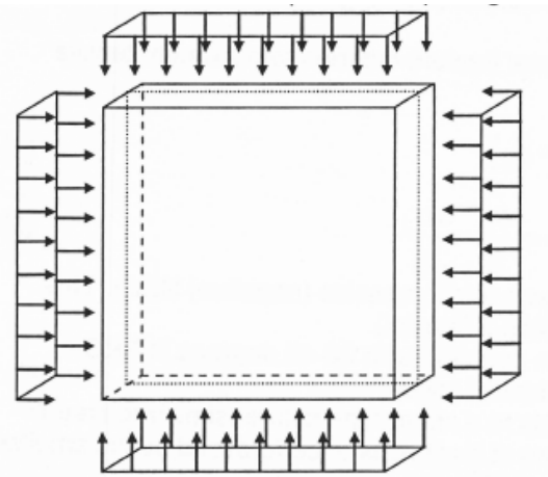

Figure 16 - Biaxial splitting fracture

Work done by Kölle et al. (2004) on steel fibre reinforced concrete in biaxial and uniaxial stress fields yielded a similar splitting failure mechanism identified by the author, see Figure 17. This was identified as a typical splitting fracture in the plane of loading, parallel to the free edge. The samples used were of size 205mm x 205mm x 50mm, cast in a special steel mould, in the same fashion as investigated by the author (initial testing) and Molapo (2010). De Koker (2004) concluded that in standard cast and vibration applications, which are used for casting the specimens for this study, fibres orientate randomly, unless influenced by the geometrical boundaries of the mould.

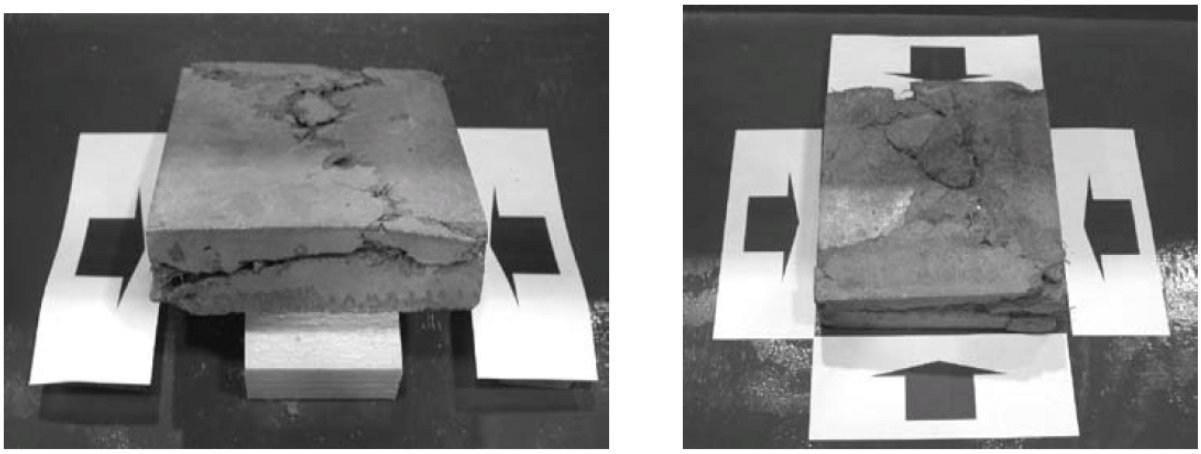

Figure 17 - Uniaxial and biaxial failure modes (Kölle et al., 2004)

It is important to understand that the fibre orientation causes specific failure mechanisms and the fibre orientation is affected by the casting method. The casting method is in turn determined by the use of the SHCC, thus the intended use of SHCC will determine the desired fibre orientation in order to prevent undesired failure mechanisms.

All the specimens shown and discussed above are relatively thin, cast elements. If the intended use for the SHCC was a thin protective layer, there would be no way of obtaining a 3D fibre orientation. Had the specimens been cut from a thicker cast element, this 3D fibre orientation would have been obtained.

From literature it can be concluded that the method of production and the fibre orientation desired or expected will influence the fracture mechanics. Thin cast members might make sense if the intended application is a thin overlay and extrusion might be an option if certain desired behaviour is required.

In this study both thin-cast specimens and larger-cast and cut specimens were tested only in compression-compression ratios to investigate the failure mechanisms caused by the loading platens. The larger-cast and cut specimens were used at all test ratios for the investigation into strength, strain, cracking and failure mechanisms.

2.7.Proposed Research

The purpose of this research project is to investigate the abovementioned phenomena of failure mechanisms, failure stresses and strains, post peak behaviour, crack formation and development, deformation response and also the ductility of SHCC under biaxial loading.

The tests will be carried out in biaxial tension and compression and thus much data will be available for analysis of the entire spectrum of loading. The final goal of the research is to propose an appropriate biaxial failure limit. Analytical expressions suitable for design and finite element analysis (see chapter 4) may be derived for the experimentally determined failure limits. In addition to the expected increased resistance in biaxial compression, increased resistance under biaxial compression-tension can be studied, to explain the enhanced shearing resistance found for SHCC (van Zijl, 2007).

3. Test Setup and Experimental Procedure

This chapter describes the methods and experimental apparatus used. Section 3.1 describes the experimental setup required to induce a biaxial state of stress within a sample. The boundary conditions are discussed in Section 3.2. The chapter also addresses other topics related to the physical testing of the samples. The biaxial setup at the University of Stellenbosch is shown in Figures 18 and 19.

Figure 18 - Biaxial Testing Setup

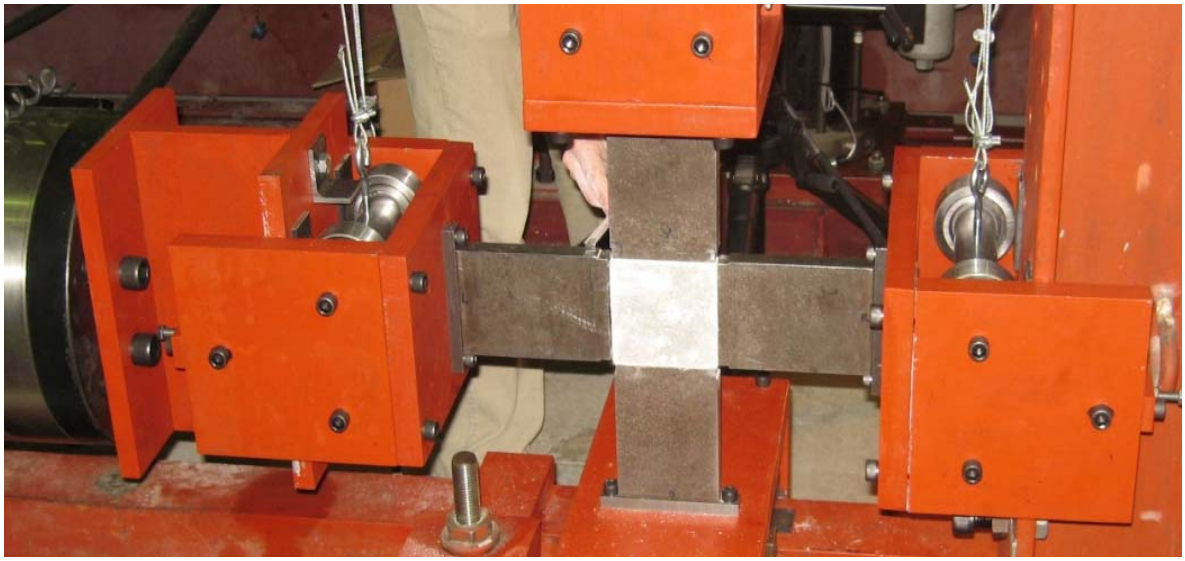

Figure 19 - Close-Up View of Biaxial Setup, Loading Platens

3.1. Experimental Setup for Biaxial Testing of Concrete

In order to induce a biaxial state of stress within a sample, two (of many) methods of load application are investigated. One approach is to use notched cube samples in a wedge splitting jig (Elser et al. 1995 & 1996). Another is to apply stress biaxially using hydraulic jacks (Yin et al., 1990; Hussein & Marzouk, 2000; and Calixto, 2002).

The hydraulic jack loading method is preferred. The use of four high capacity jacks, (Ehm & Schneider, 1985), is preferred, but expensive; therefore only two hydraulic jacks were used in conjunction with a bearing and support system for the loading platens that would accommodate specimen deformation, see Figures 18 and 19.

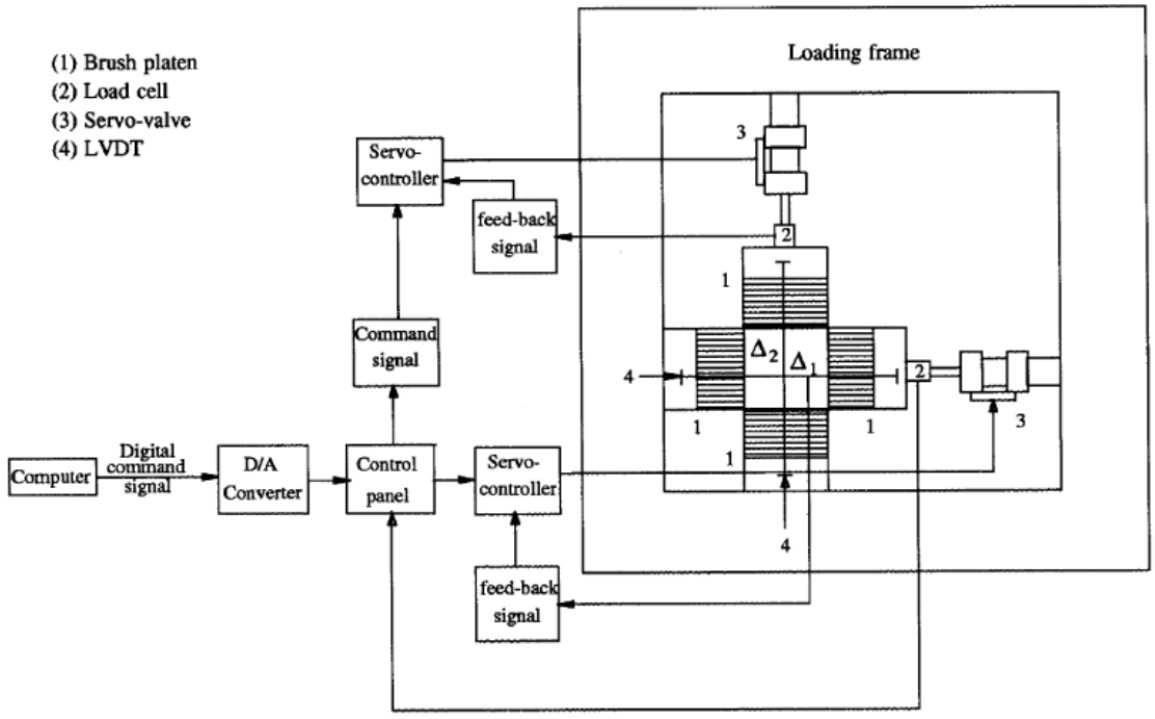

Figure 20 - Block Diagram Highlighting the Details of the Closed-Loop Tests Scheme (Hussein & Marzouk, 2000)

A setup including two 500kN hydraulic jacks (Instron), controlled by the Instron Console software (Instron Wave Matrix) is used, which operates on a closed-loop with internal LVDT's inside the load cells on each of the jack faces. The layout consists of a frame containing the jacks at 90° to each other, with specially built head pieces that hold the loading platens in position whilst allowing motion of the platens due to specimen deformation (refer to Section 3.2), see Figures 20. A complete set of drawings of the setup can be found in Appendix B.

3.2. Boundary Conditions

The boundary conditions at the interface of the loading platens and the specimen need careful consideration. The head pieces for each of the loading platens had to be specially designed to allow for the correct simulation of the boundary conditions whilst the sample deforms under loading. The setup has to allow for in-plane translation only, whilst avoiding any out-of-plane motion. Translational movement is allowed by making use of bearings, while movement perpendicular to the hydraulic jack orientation (in other words along the jack axis) is controlled by the jack movement.

A design for the bearing system was proposed and the final design can be seen in Figures 21 and 22. Care had to be taken to ensure that limited deformation of the loading train relative to the sample deformation occurs. Calculations were performed in order to choose a suitable thickness for steel used, as well as bolt- and bearing sizes. Hardened plates were used under the bearings to ensure that they do not cause local depression deformation into the steel sections. These hardened plates were hardened to Rockwell 48. This procedure had to be followed to avoid the resistance due to bearing breakaway force required. Experts from the bearing manufacturers industry were consulted to order the most suitable bearings for the application. A calculation of the breakaway force (Fv) can be seen below.

$$Fv = \frac{2(fr.Fr+Mr)}{D} \quad [6]$$

where f_r is the rolling friction coefficient for raceways made of hardened steel: f_r = 0.05mm

Fr is the radial load, N

D is the outside diameter of the track roller, mm

M_r is the frictional torque of the track roller, Nmm

and

$$Mr = f.Fr.\frac{dm}{2} \quad [7]$$

with d_m the mean bearing diameter (d+D)/2 of track roller, mm

f the coefficient of friction

For the needle rollers NART 40R, and the values of fr = 0.05mm, a value for breakaway force, Fv = 86.25N is calculated from Eqs [6] & [7]. As this force is considered to be acceptably small, the chosen bearings are NART 40R track rollers from IKO.

These boundary conditions would then allow for the concrete specimen to deform in-plane according to the displacement of the two actuators whilst also allowing for relatively unhindered expansion in the orthogonal direction. The frictional effects in this orthogonal direction between the platens and the specimen are to be minimised. Several authors, eg. Elser et al. (1996) and Kölle et al. (2004) have used Teflon sliding layers to allow for frictionless lateral expansion of the samples, with Kölle et al. (2004) reporting damage to the layers. These layers are of course, only to be used in the compressive testing regimes.

The minimisation of this frictional force is also addressed by using brush-type loading platens (Swaddiwudhipong and Seow, 2006; Van Mier, 1984; Calixto, 2002; Torrenti and Djebri, 1995; Yin et al. 1990; and Hussein and Marzouk, 2000). Refer to section 3.6 for more on the effects on the brush-type loading platens.

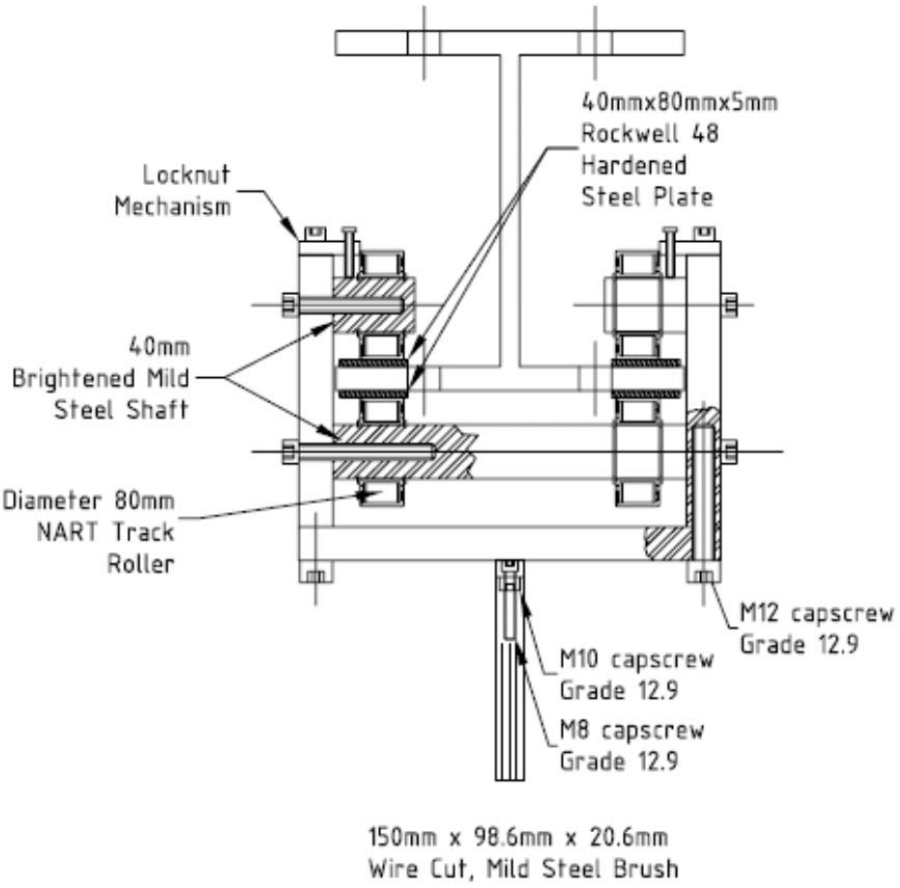

Figure 21 - In-plane view of bearing system

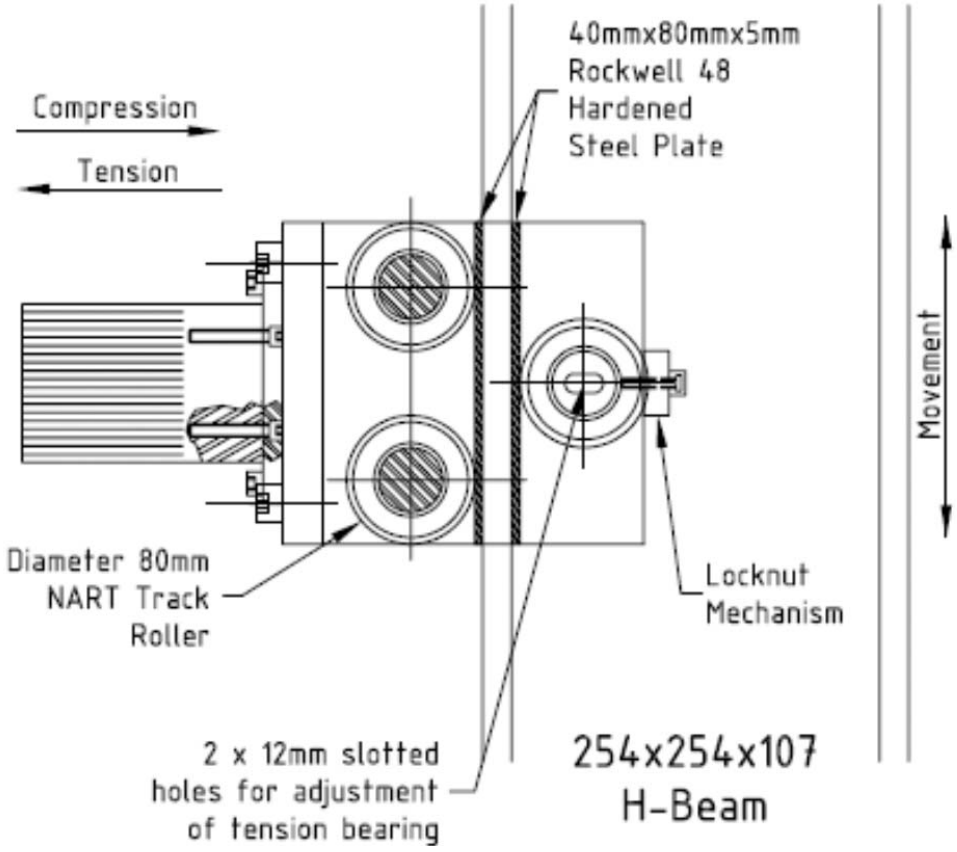

Figure 22 - Front view of bearing system

3.2.1. Teflon Sliding Layers

With reference to Section 3.6, it was found that there is a lateral friction force induced locally at the specimen to loading platen edge when in a compressive state. It was decided to put Teflon layers in between these to ensure a close to frictionless lateral expansion of the specimen under load. This layer has also been used by Elser et al. (1996), who found the best results using a Teflon cardboard layer combination. This then allows for a very nearly free transverse strain.

The Teflon used is Chemstik® CF203 (Tygaflor 308A/03T) from Quadrant Chemplast Pty Ltd. The Teflon layer has a thickness of 0.070mm; see Appendix C for more data.

3.2.2. Epoxy Resin Layer in Tension Testing

In order to enable successful tension testing, a means to hold the specimen whilst being under plane stress requires careful consideration of the epoxy's bond strength. Two-part epoxies have been successfully used (Stander, 2007) but as the surface area in this case is small, epoxy on the edges only does not yield a sufficient overall bonded tensile force for destructive tensile testing of the specimen.

The solution is to have plates on the sides of the loading platens that extend about 20mm past the specimen edge. This would mean that there is about three times the area for bonding to the concrete specimen, see Figure 23.

Figure 23 - Epoxy application on specimen

The Epoxy used is Sika AnchorFix®-2, a high-performance anchoring adhesive from Sika®. Two of the main reasons for product choice would be that the two-part epoxy is mixed automatically in the applicator nozzle and the fast curing time. At room temperature, the curing time is about 40minutes. See Appendix D for data on the product and Appendix B for design drawings.

3.3. Test Control and Safety Mechanisms

Control of the system is a hybrid method whereby a force is applied at a given rate (force load control) and the displacement of the jack faces is then limited. Once the maximum displacement is reached in either of the two directions, the system automatically shuts down; this is for both the safety of the system and for the protection of the specimens after failure.

For compression, a force is applied at 3.4kN/s until failure. The dominant axis constantly applies this 3.4kN/s while the slave axis applies a ratio thereof. For compression-tension tests, the dominant axis constantly applies a force of 0.1kN/s and the slave, ratios thereof. Finally, for tension-tension tests, the same force rate as for compression-tension is applied. The stresses caused by these forces are referred to as the in-plane stresses henceforth. The biaxial test ratios can be seen in Figure 3.

3.4. Measurement

The LVDT's contained by the Instron load cells measure only displacements in the direction of the movement. Thus we have displacement values in the two in-plane directions. The software package is able to calculate various parameters and plot the results, stress-time as well as stress-strain to name but two options. The question is however, if these are the desired parameters and if the Instron software is the only measurement tool used, whether this will enable adequate description of the specimen response.

An issue would be that the loading train is not infinitely stiff, thus the Instron LVDT's do not measure deformation of the specimens only. Only total deformation is measured by LVDT's over a set guage length. It is desirable to measure local response on the specimen to quantify crack patterns in terms of spacing and width throughout the load-deformational response. The limitation of having measurements of total deformation only, as well as limited space count against the use of only LVDT's.

There is an optical solution to strain measurement. Deformations of the specimens can be optically recorded using the ARAMIS system. This system uses two high definition cameras mounted a distance apart, so that a 3 dimensional picture is created of the face of the specimen. The cameras take photographs at a prescribed frequency, which can be changed at will up to a maximum frequency of 2Hz, and record the deformation by means of tracking pixels (of which the size can de set by changing the definition in the software). Measurement is facilitated in the software by pattern recognition of

stochastic black spots sprayed onto a white specimen face. Care must be taken in the spray painting process as blotches will cause gaps in the data collected by the system.

Two dimensional deformations are measured by selecting a block on the specimen face without any, or as little as possible, interference from the fracture. The block would be in the central part of the sample face. The coordinates of 4 grid points at the outer ends of this central block with a cross central to each specimen, can be used to calculate total deformation in each principal direction (horizontal and vertical) over the block dimensions. Subsequently, average strain in each principal direction was calculated by division of the total deformation by the length. However, detailed information of local deformation is also available, from which crack widths and local strains can be derived with high precision.

3.5. Cutting of Specimens from Larger-Cast Members as Solution to Wall Effects

A possible solution to the fibre orientation aligning with mould sides is to cast a larger body of concrete and then to cut slices of material into the desired specimen size. This would then be representative of the material as cast in situ, which has been pointed out as extremely important for this research (van Mier, 1984). It should however, be noted that for thin walled applications, such as precast permanent formwork shells or thin-layered repair layers, casting of thin specimens is most realistic. If the structural application will, however allow for 3 dimensional fibre orientation, specimens cut from larger blacks are more representative of the field material.

Torrenti and Djebri (1995), had specimens sawn from large blocks (102 x 92 x 56cm) to avoid wall effects. This same method was followed by Elser et al. (1996), where samples were cut from rectangular slabs so that the casting orientation was at 90° to the orientation of loading.

Yin et al. (1990) used larger, (15 x 15 x 50-cm) steel moulds for casting, and the desired plate specimens were then cut from these concrete blocks using a precision diamond saw. Before cutting, the concrete blocks were stored in a water tank at 26°C and the sawing was performed a week before testing. Following the cutting, the concrete specimens were coated with two thin layers of sealant to prevent the evaporation of water from the edges.

Calixto (2002) used larger cast samples of the same size, which were cut into the desired samples size. He stated that the samples were cut slightly larger than the final size and were then ground down. The edges were sandblasted, roughening them up, using silica sand so as to facilitate a good bond between the epoxy resin and the sample edge (Calixto, 2002).

Van Mier (1984) considered the options and provides us with insight into why cutting is considered above simply casting specimens. Mentioned in Section 3.6, is the fact that specimen edges have to be perfectly accurate in order to ensure accurate load transfer between loading platens and the specimen. Van Mier recommended two methods of manufacture: either the specimens were to be cast in accurate stiff moulds, or larger blocks were to be casted and then the specimens cut from them.

The use of brush platens for load transfer would mean that the cast method would be preferred as the high load concentration at the specimen surface caused by the small cross sectional area of the brush bristles would be “smoothed out” by the soft cement-matrix layer at the surface of the specimen, brought about by segregation whilst drying. Also, the penetration of these bristles into the soft concrete (found to be present) would aid in preventing buckling of these bristles. However; the use of these cast specimens would cause that one has a heterogeneous material with various kinds of segregation effects. The edges would then have to be prepared by sawing in some cases to ensure a perfect load application surface (Van Mier, 1984).

Van Mier (1984) thus preferred the sawing method. Larger specimens were cast in 700 x 135 x 135-mm prisms from which 6 cubes (about 103 x 103 x 103-mm) were sawn after 28 days of hardening under water. The opposite sides were then precision-sawn to have a perfect 100 x 100 x 100-mm block. This cutting off of the sides (thickness greater than aggregate size) ensured that segregation did not introduce any softer material into the specimens. This edge preparation provided the best boundary conditions for tensile testing (Van Mier, 1984).

It is then deduced that no perfect method exists for yielding ideal results, but one must agree that a homogenous specimen is favourable. See Figure 24 for the proposed cutting of concrete blocks from a larger cast prism by Van Mier (1984).

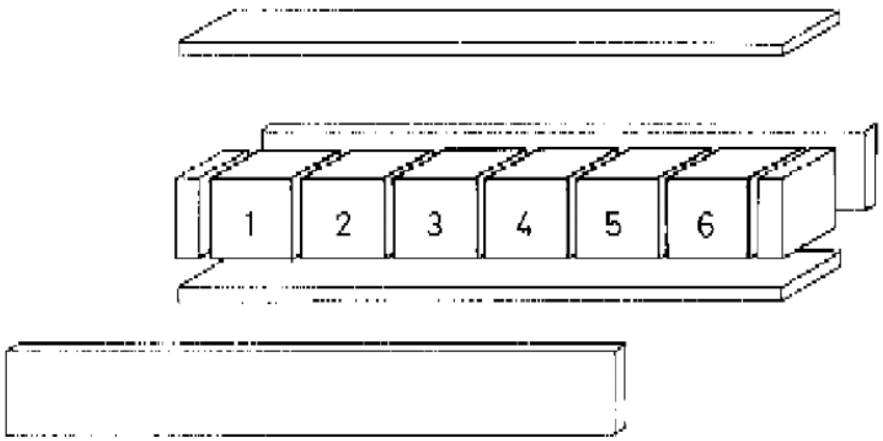

Figure 24 - Cubes sawn from larger initial prisms (Van Mier, 1984)

A closer look should, however, be taken at the surface of both cast- and sawn specimens. A problem regarding cast specimens is that drying and associated shrinkage occur quicker at the surface. In conjunction with a totally different behaviour between the core material and material close to the surface, yields different deformation behaviour. Sawn samples also do not perform perfectly either in this context as splitting off of segments of aggregate caused by cutting can occur at the sawn surface. This splitting can be seen in Figure 25, the sawed off sample edge is on the left, and the cast sample edge is on the right.

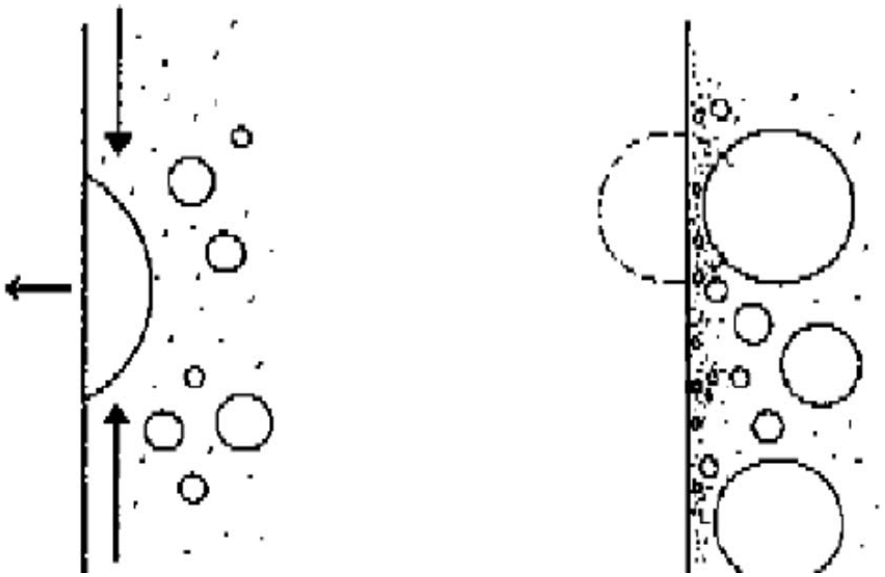

Figure 25 - Sawn- and moulded specimen edges (Van Mier, 1984)

Referring to the SHCC mix design, Table 2, one can assume that the sawn off edge preparation would be preferred. The absence of large aggregate in the SHCC mix used would eliminate the problem portrayed in Figure 25.

What has however, been found with tensile tests carried out by the author on cast sample edges was that the top layer of finer material is pulled off when an epoxy resin is used to test bond strength. This top layer is the so called soft cement-matrix layer at the surface of the specimen, as mentioned above and by Van Mier (1984).

3.5.1. Specimen preparation for experiments

As tension and compression testing falls within the scope of this research, in the light of the discussion in Section 3.5, attention has to be paid to the preparation of the edges of the specimens. Calixto (2002) sand blasted the edges with silica sand to roughen the mating surfaces before applying an epoxy adhesive.

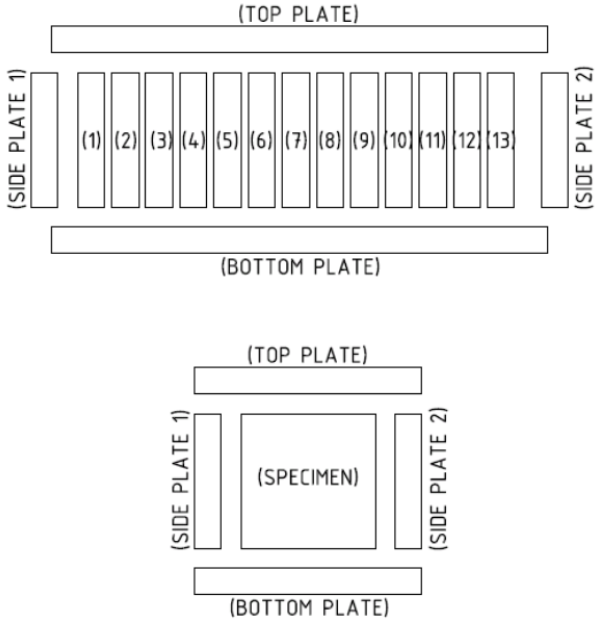

Figure 26 - Cutting scheme for specimens cut from larger cast prisms

Referring to Section 3.5; Van Mier (1984) found that cutting of samples from larger cast specimens was sufficient for edge preparation. The final sample size is to be 102.6 x 102.6 x 20.6mm. These will be cut from a larger cast specimen, much like that of Van Mier, Figure 24. Refer to Figure 26 for proposed

cutting scheme for the samples. About 20mm should be cut off from all external surfaces so that the material will consist of material from the core of the prisms only, thus ensuring a more homogeneous specimen. After the samples have been cut, the corners of the samples must be chamfered slightly for safety reasons, as this will allow space for the loading platens not to touch each other during deformation.

SHCC beams (750mm x 150mm x 150mm) were casted and allowed to set for a day, in a temperature and moisture controlled room. The moulds were removed after a day and the beams were placed in a water (20°) bath for 28days. A proposed method of storage could also be that the samples should be placed in plastic and kept in a temperature controlled room until testing (Van Mier, 1984).

3.5.2. 3D Fibre Orientation Effects

As discussed in Section 3.5.1, samples were cast and then cut to size. This means that a 3D fibre orientation should be achieved in the core of the beam. The 3D fibre orientation changes the fracture mechanics of the specimens drastically. The failure mechanism is no longer a flaking or splitting-off of pieces of the sample, but rather a shear-type fracture as is expected from FRC (Yin et. al., 1990), see Figure 27 and 28.

Figure 27 - Uniaxial Compression Tested Specimen, 3D Fibre Orientation.

Figure 28 – Biaxial compression failure, specimen shows shear failure

Figure 27 shows the face of a typical fractured specimen after a uniaxial compression test. This figure should be compared to Figures 12 through 17 in Section 2.7.

The failure thus occurs as it is expected to, which means that the wall effect problem has been successfully addressed by casting a large member of the SHCC and then cutting the specimens from the core.

It is important to realise that the uniaxial tensile tests (results are give and discussed later in this thesis) performed on standard dumbbell specimens are not cut from the core of a larger element, but rather a thin-cast specimens. This means that a 2D fibre distribution is achieved and will thus affect the behaviour and resistance. This differs completely from the specimens as cut for the biaxial tests and thus the specimens will behave differently under load. For the biaxial specimens, fewer cracks are expected (a.r.o. 3D fibre orientation) because fewer fibres are effective at bridging cracks. This effect of fibre orientation can be seen in the equation for ultimate strength, equ. [8].

$$f_t = f \; x \; V_f \; x \; \frac{L_f}{d_f} \; x \; \tau \qquad [8]$$

where f_t = ultimate strength (MPa)

f = efficiency factor (1 for 1D fibre orientation, 0.64 for 2D fibre orientation and 0.5 for 3D fibre orientation (Hannant, 1978))

L_f = Length of fibre (mm)

d_f = diameter of fibre (mm)

τ = bond shear stress (MPa)

3.5.3. Specimen Fracture Due to Dimensional Imperfections

If the fractured specimens are investigated, one often finds that some samples have undergone failure in such a way that cracking seems to have propagated from a corner of the specimen. A v-shaped crack pattern is observed, see Figure 27. This v-shaped failure type is similar to the failure shown in Figure 13, except that it occurred from two directions, thus breaking off a corner as opposed to an entire edge splitting off.

In the testing procedure, it was also noted, by inspection, that when the platens are adjusted into position, some of the corners touched the platens before the rest of the side (loading face) touched. Sample edge preparation by cutting samples into a perfectly parallel and rectangular sample would ensure uniform load application (Van Mier, 1984), although it is virtually impossible to prepare flawless specimens and perfectly uniform load transfer.

It is proposed that this is because it is impossible to cast specimens with exactly perpendicular sides and so the load is not applied uniformly and thus the sample must deform considerably before the entire edge becomes loaded. It was found to be a considerable problem for Swaddiwudhipong and Seow (2006) and they had rockers installed in their loading platens to accommodate up to 4.5° rotations. It is unlikely for such large rotations to occur in this case, as very small variations in dimension, in the order 0.5mm, were recorded by measurement of individual specimens.

3.6. Effects of Loading Platen Type on Specimen Fracture

To investigate the effects that either a solid-or brush-type loading platen will have on the fracture and loading capacity, both solid and brush platens were used. Various other authors such as Van Mier (1984), Ehm and Schneider (1985), M Calixto (2002) and Kölle et al. (2004) to name a few, had used the same approach to compare the effects to choose a method to minimise the boundary effects. Figure 29 shows typical examples of the abovementioned loading platen types.

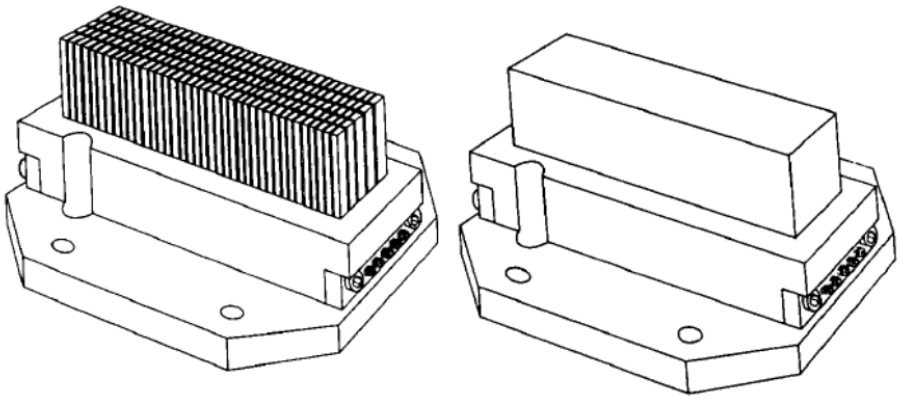

Figure 29 - Brush-type and Solid-type Loading Platen (Ehm and Schneider, 1985)

Tests yielded that the loading platen definitely had an effect on the nature of the fracture of the specimen. It was reported that the solid platens also contribute to the capacity of the samples, due to the friction-induced confinement in the regions of the specimen-platen interface, and thus the failure stress in compression is overestimated (Kölle et al., 2004). This would make it seem that the brush-type platens are better, but the brushes tend to undergo permanent deformation, damaging the bristles and thus the loading surface is different for each test, making the results unreliable (Kölle et al., 2004). In biaxial testing, it was found that damage did occur and the brushes were permanently deformed, Figure 30.

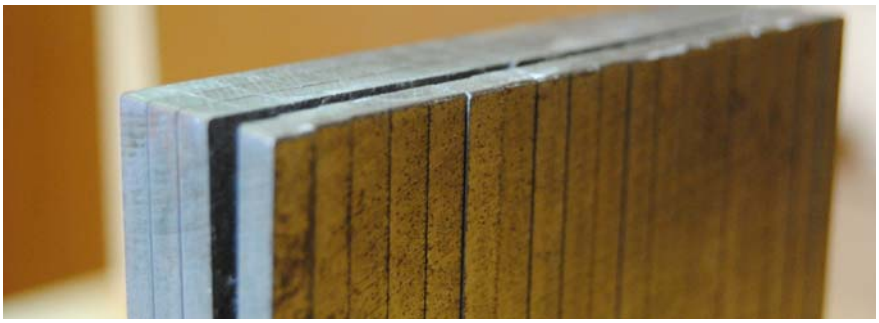

Figure 30 - Permanently deformed brush-type loading platen

Figure 31 shows how the solid platens could contribute to the failure of the specimens by the wedging off of pieces of the specimen. As the compression load increases, the concrete cracks in a plane parallel to the free surfaces, where after the platen forces a wedge in between the sides and causes an oblique shear failure mechanism. The frictional forces between the platen and the concrete cause the interface to remain intact.

Figure 31 - Wedging caused by 2D fibre alignment (primarily) and friction with solid platens

This effect then has to be countered or limited to ensure that it does not cause a mechanism. A recommendation was to make the loading platens thicker, rather than the same thickness as the specimens. This will ensure that there is enough space on the face of the platen for the specimen edge to deform laterally, without interference from the platen edge, whilst still allowing for the identified failure mechanism to develop. In other words the platen should only be made thicker than the sample to avoid interference with the failure mechanism.

Another observation is the crushing effect of the brush platens. After the test, it was found that the bristles penetrated the concrete and fibres as well as matrix had become lodged in between the bristles. The bristles also had the same effect as the edge of the solid loading platen. This occurred as lengthwise lines, with protruding matrix and fibres, across the specimen edge, as seen in Figure 32.

This phenomenon was found also by Van Mier (1984), he stated that high load concentration at the specimen surface caused by the small cross sectional area of the brush bristles would cause the penetration of these bristles into the soft concrete, refer to Section 3.4.

Figure 32 - Brush Platen Bristle Wedging Effect on Specimens

This penetration of the bristles would indicate then that brush platens are not the perfect solution to the challenge of allowing laterally free boundary conditions. The penetration by the bristles into the softer cement-matrix layer at the surface of the specimen, brought about by segregation, causes deformation which is independent of the deformation of the core, influencing the deformation response, and the result (Van Mier, 1984). It should be known that only thin-cast specimens were tested with the brush platens and not the larger cast and cut specimens, thus segregation did occur at the free edges of the specimen.

The final choice for this research is a combination of thicker solid platens (thicker than specimens), with thin Teflon "sliding layers" between the platen and the specimen for compressive cases. The idea of using Teflon sliding layers on such a friction surface is not unfamiliar to the research topic and has been used in combination with cardboard (Elser et al. 1994 & 1996).

4. Finite Element Analysis Model of Biaxial Setup

4.1. Need for Model

Finite element modelling can yield useful results when a reasonable representation of the physical behaviour is modelled. The model can be used for prediction of problem areas where small changes can be made to investigate their influence on the results.

Although the biaxial response of this particular FRC is the purpose of the experimental test programme, it is useful to use existing biaxial models to study the expected behaviour in anticipation of the experimental results. The model is created using existing material laws, crack models and a multi-surface failure criterion. Accurate uniaxial stress-strain models characterised from uniaxial experimental responses of SHCC were implemented. By accurate simulation of the physical conditions in the experiments, and by as accurate as possible simulation of the material behaviour, problems with the setup can be foreseen. The final objective of computational modelling might not be achieved within the limitations of this study, as the experimental data should be used to develop an accurate biaxial model for FRC tested here. Computational modelling falls beyond the scope of this study. It may, however turn out that biaxial behaviour of FRC can be captured by existing biaxial models, by appropriate model parameter characterisation.

4.2. Computational Software

Various factors have to be taken into account in order to build a FE model of the biaxial test of SHCC. These include the pseudo-plastic material behaviour, interface mechanics, confinement effects, as well as cracking. A FE Analysis software package, TNO DIANA, is used for the creation and analysis of the model in this research. This chapter will discuss these factors and other phenomena that need to be accounted for.

4.3. Total Strain Rotating Crack Model

With reference to the material behaviour, it is important to distinguish the stress-strain response from failure criterion, which in this case is a multi-surface limit function to capture the different limits to linear elastic behaviour found for SHCC in tension from that in compression. Figure 33 shows the Total strain rotating crack model and Figure 34 the multi-surface failure criterion.

The total strain rotating crack model is used as the input in Diana to serve as the basis for material behaviour in both compression and tension. For each test, this serves as the basic material behaviour. At every biaxial stress situation, a different curve is however obtained due to the biaxial interaction. This means that for each of these curves there is a biaxial stress condition and a unique failure point defined by the biaxial limit function. If all the possible failure points are plotted, one obtains a failure criterion. It should then be noted that the two curves in the Figures 33 and 34 are inter-dependent.

To show how the curves influence each other, a point on the curve in Figure 34, point (1), would follow the original stress-strain law in Figure 33, given as curve (1). Another point on Figure 34, point (2), would correspond to a different stress-strain law in Figure 33, given as curve (2).

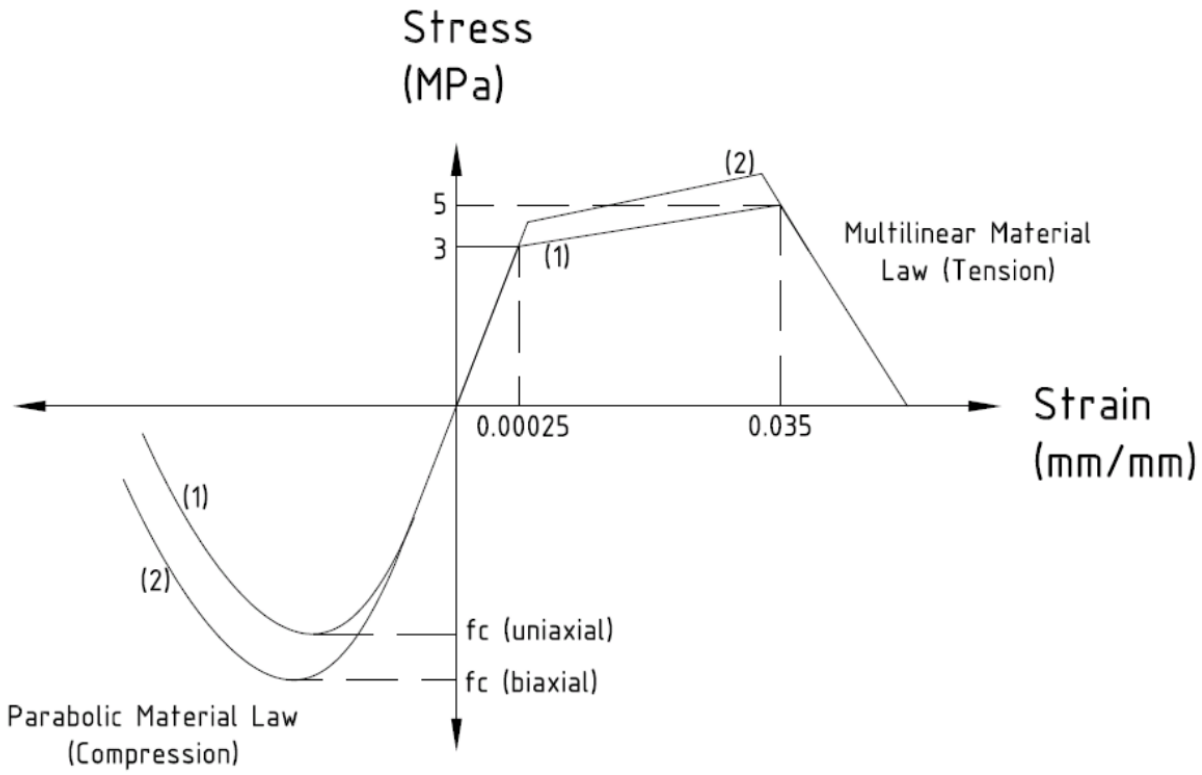

Figure 33 – Material law (stress-strain curve) implemented in the total strain rotating crack model

The multi-surface failure criterion is given in Figure 34. Due to different behaviour of SHCC in compression and tension, the same limit functions cannot hold. The failure criterion given in Figure 34 is a combination of the Rankine and Von Mises failure criteria. The criterion states that for compression and partially compression-tension, the Von Mises function is the limit and for tension and partially tension-compression, the Rankine function is the limit.

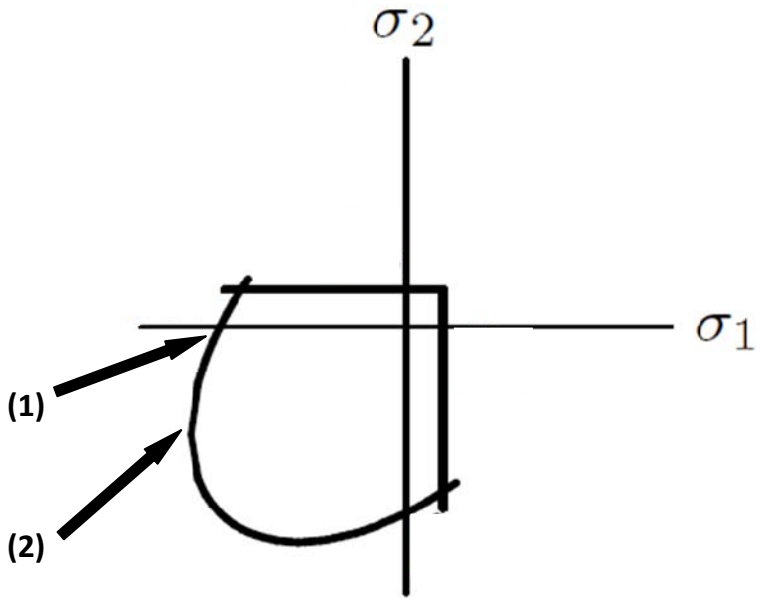

Figure 34 – Rankine-Von Mises failure criterion

The bulge in the Von Mises (compressive) curve, Figure 34, is brought about by the confinement effect. Thus, minimum principal stress is not the failure stress which would require that compressive limit function would also be straight lines parallel to the Rankine tensile limit function, as has been proposed for simplicity and lack of characterisation data on biaxial behaviour of SHCC by van Zijl (2009).

4.3.1. Material Law

The total strain crack model allows the user to prescribe the stress-strain law for both compression and tension. One of the attractive attributes of the model is that the model describes the tension and compression behaviour of the material in a single material law (but as different functions), Figure 33. The model requires as input the basic properties such as Young's modulus, but also the definition of the general material behaviour in compression, shear and tension.

As discussed in section 4.3, a multi-surface plasticity model is required as it addresses several physical phenomena rather than compressive and tensile behaviour individually. This enables realistic simulation of biaxial response in all quadrants (compression-compression, compression-tension, tension-tension) using the total strain rotating crack model.

The total strain rotating crack model has the functionality of incorporating smeared cracking and rotating crack concepts; refer to section 4.3.2. The stress-strain law for tension has to be able to

incorporate hardening as required for SHCC. The model offers such functionality, which makes the model attractive for this study.

4.3.1.1. Material Law for Tensile Behaviour

The model requires the user to prescribe the material law that the material would follow under load. Physical uniaxial tests thus have to be investigated in order to propose a suitable material law.

Figure 35 shows tests results for uniaxial tension testing of similar SHCC as used in this research, performed in the same research group. It can be deduced that the graph follows a trilinear trend (indicated by dashed lines). The curve starts with a linear portion until yield (f_t), extends to ultimate stress and strain (f_{tu} & ε_{tu}) and then the end of the test.

The tension behaviour of SHCC is thus assumed to be multilinear and values for the yield stress (f_t), yield strain (ε_t), ultimate stress (f_{tu}) and ultimate strain (ε_{tu}) can be proposed in Diana, which will then prescribe the material law, as shown in Figure 33.

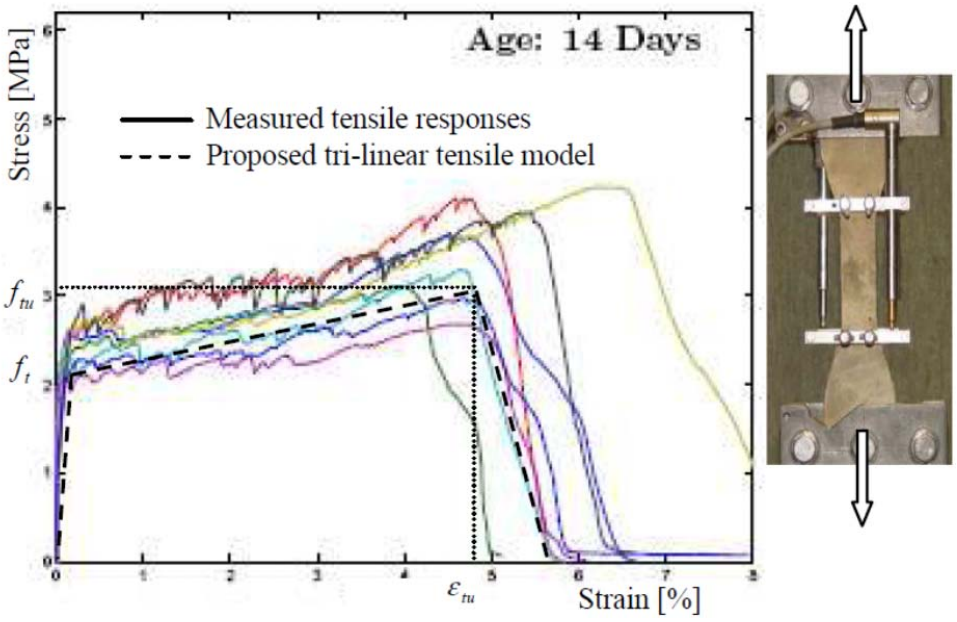

Figure 35 – Uniaxial tensile behaviour of SHCC dumbbells, gauge 80mm, section 30x15mm (Van Zijl & Stander, 2009)

With reference to Figure 35, the linear –elastic response is limited by the first cracking stress, after which the strain hardening branch starts. The pseudo-strain hardening behaviour is caused by the effective crack bridging by the fibres. This is achieved by multiple fine cracks forming at increasing

resistance with increased deformation. Softening starts at the ultimate stress and strain. This is the point at which the fibres either pull out or break in a single crack (Van Zijl &Stander, 2009).

Confinement Effect in Tensile Behaviour

The confinement effect has an influence on compressive as well as tensile behaviour. With reference to Figure 34, the limit function in tension is a straight line. If there is confinement, these straight lines will become curved as a result of the increased or reduced stresses. This study aims to determine the line experimentally, see section 5.

4.3.1.2. Material Law for Compressive Behaviour

The uniaxial compressive behaviour of SHCC has been investigated and the results are shown in Figure 36. Although the curve for specimen 1 would seem more multilinear, the curve for specimen 2 hints at a parabolic material law for uniaxial compression. The curves indicate that beyond the linear-elastic range, strain hardening follows until peak response followed by either gradual, near linear strain softening, or more pronounced strain softening as shown by specimen 2. Note that the tests were stopped at roughly 1mm and 0.75mm deformation respectively for the tests shown in this graph. The two responses represent the range in post-peak response for this type of SHCC, and a parabolic material law was considered to be suitable for uniaxial compression.

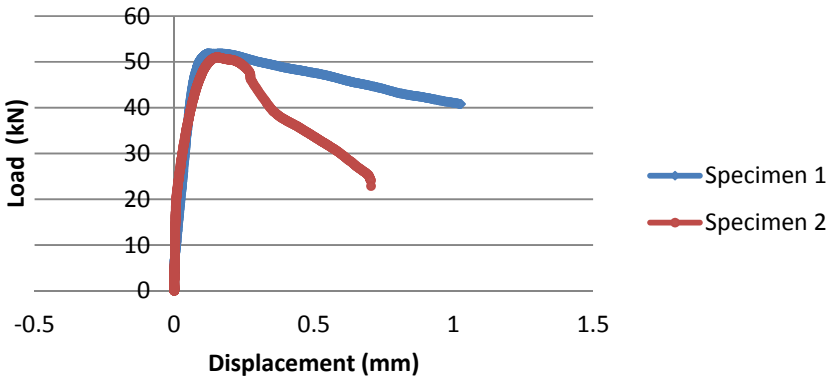

Figure 36 - Load-displacement curve for SHCC cylinder specimens under uniaxial compression (Molapo, 2010)

As one of the parameters in the particular stress-strain model input, the fracture energy must be given, G_{fc}. This fracture energy is calculated from a uniaxial compression curve as the area (excluding elastic

behaviour) under the curve. An average parabolic compressive response is used in the stress-strain model.

One must be careful when dealing with fracture energy as it is defined as the amount of energy released per square meter on the face of the crack. In compression, there are more but smaller cracks than in tension; it would seem that the so called fracture energy is much larger, even up to 100 times larger. Had one dealt with tension, the fracture energy would have to have been prescribed for each crack. This concept of fracture energy is thus only a numerical one, to allow for the softening curve to be calculated with reasonable agreement with the physical response.

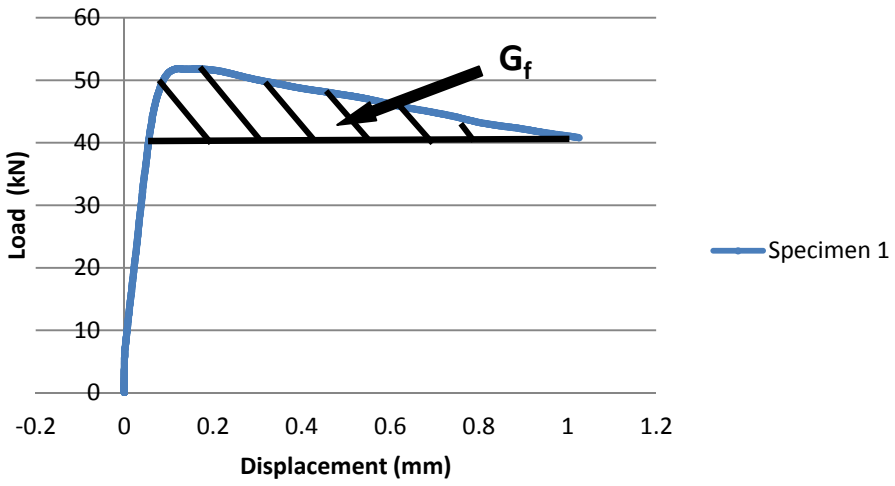

Figure 37 - Uniaxial compressive curve for SHCC, showing fracture energy calculation, Molapo (2010)

In order to calculate the fracture energy, one must be aware that the softening part of the stress-inelastic strain curve must be integrated, i.e. the strain calculated from Eq. [9], shown in Figure 37.

$$\varepsilon_i = \varepsilon - \frac{\sigma}{E} \qquad [9]$$

Confinement Effect in Compressive Behaviour

Diana implements the confinement effect (or lateral influence) in several stress-strain models, except for a multilinear stress-strain law. As per Figures 33 and 36, the material law for compression is assumed to be parabolic; other laws are available (such as multilinear), but more experimental data is needed in order to specify the multilinear stress-strain curve.

Diana allows for the lateral influence due to confinement to be implemented in the parabolic stress-strain law as part of the total strain rotating crack model. The Diana user manual states that not all stress-strain laws can be combined with the lateral influence model. This lateral influence model by which confinement is incorporated in the compression model was proposed by Selby and Vecchio (1993).

4.3.2. Cracking

As the total strain rotating crack model name suggests, the cracking model implemented is of utmost importance. In order to discuss a suitable crack model, one must turn to the finite elements used in the mesh. The DIANA Element Library offers various elements of which the Q8MEM (four node quadrilateral) is used here. This is an isoparametric plane-stress element based on linear interpolation and Gauss integration. Strains are constant in one direction and linear in the other, and visa-versa, with constant shear strain across the element. Refer to Figure 38. The element was chosen above triangular elements as the edges of the triangular elements would be aligned in one direction, which could influence crack propagation lines when non-regularised material models are used.

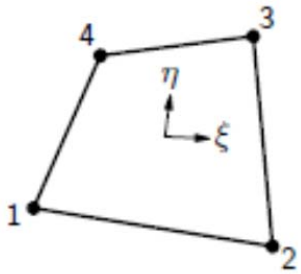

Figure 38 - Q8MEM (Quadrilateral, 4 Nodes), Diana User's Manual - Element Library, Release 9.4, Dec 4, 2009

The constant to linear strain as a result of the linear interpolation functions is limiting in accurate representation of stress and strain gradients and thus an element with a higher interpolation scheme would seem a more attractive choice. A small element size would, however make up for this to an extent, while avoiding numerical difficulties associated with higher order elements in physically non-linear problems. The element size is chosen to be 2.5 x 2.5mm, which is roughly the potential saturated crack spacing in SHCC.

The cracking is modelled as Smeared cracking (Bazant and Oh, 1983 and Rots, 1988) which allows continuum modelling of cracking, by assuming that a localised crack is spread or "smeared" across the

width of a continuum element. This then would enable that a certain area experiencing high stress can be modelled with a crack band.

The smeared crack models provide for fixed (single or multiple) or rotating crack concepts. In the rotating crack concept cracks form perpendicular to the principal stresses, and subsequently may change orientation as the stress field changes in the post-crack initiation response in order to remain perpendicular to the principal stress. The analysis identifies areas of greatest principal stress, thus the zones in which cracks are expected, and the crack band propagates from that area.

In modelling the crack band, DIANA assumes a default crack bandwidth equal to the square root of twice the element area, which can be overruled by the user, if need be.

Softening response in a crack band may be objective if the above method of linking the crack width or band to the finite element size. It has been shown that, if it is not done, reduced element size leads to increasingly brittle computed response, which is a clear inobjectivity, or dependence on the finite element size used in the analysis. Such a crack band approach may not be sufficient for objectivity, and more sophisticated regularisation methods may be required. Such models are considered to fall beyond the scope of this thesis.

4.3.3. Degrees of Freedom and Interface Behaviour

The interface between the SHCC and the loading platens is modelled as a line, with the only degrees of freedom being in plane displacements. Modelling the support conditions for the interface element must be limited in displacement to have the correct degrees of freedom (DOF), refer to Figure 39 for the DOF of the interface element used in this research.

Considering the interface formulation, the material law for interfaces is written in terms of tractions (stresses) and relative displacements. The interface should be considered to represent an interaction in the model during compression, and the epoxy in tension. It must comply with the overall stiffness of the system. In this work, the interface is modelled as sufficiently stiff to prevent material penetration through the interface. Hereby the finite stiffness of the epoxy is ignored, but this is considered not to be of significance in modelling the specimen response to the biaxial loading.

The interface element theory is described in detail in sections 9.3 and 12 of the Diana Material Library and Element Library. The element of choice is L8IF, which is a linearly interpolated Line Interface

Element. These elements can be used for plane stress, bond-slip, plane strain or axisymmetry. In this case, plane stress is considered. Figure 39 shows the L8IF element topology along with the abovementioned DOF's.

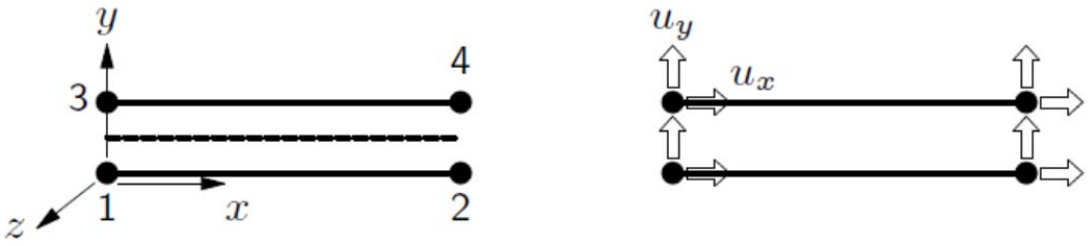

Figure 39 - L8IF Topology and Relative Displacements, Diana User's Manual - Element Library, Release 9.4, Dec 4, 2009

In modelling these elements, various geometrical (thickness), integration (scheme and integration points) and material model parameters are required. For the material behaviour, the linear elastic normal and shear stiffness must be prescribed, which was considered to be infinite as described above. These then set the multi-linear relation between the respective tractions and displacements. For this model, the interface represents the epoxy which glues the platens to the concrete. The FEM results for only the concrete are desired, thus the interface will not be modelled for failure criteria and hardening or softening. Only a normal and tangential stiffness will be given to the interface. The function of the interface is purely connecting the platen to the concrete, which is obviously required in tension.

4.4.Loading

The load is applied in the model by means of Force-control, see Figure 40.

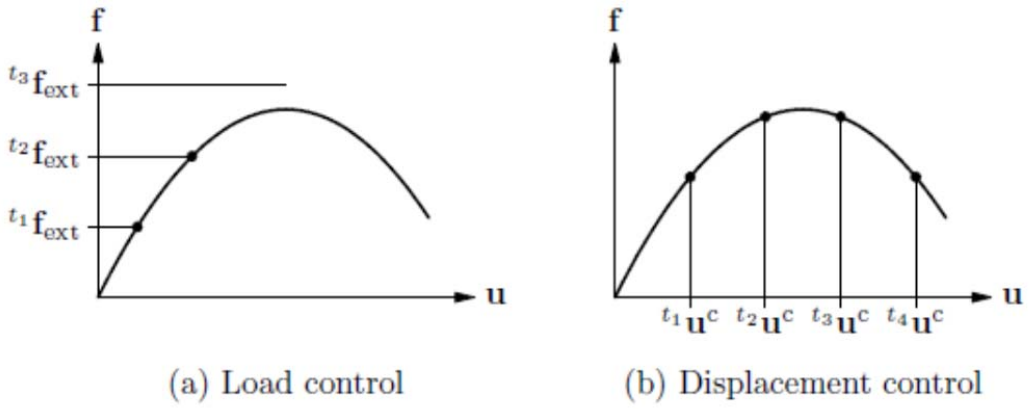

Figure 40 - Load control (a) vs. Displacement control (b)

In order to use force-controlled load application that allows for post-peak behaviour, an interpolation scheme other than for e.g. Newton-Raphson must be used. The arc-length method, which facilitates the possibility of post-peak behaviour (such as snap-back behaviour), smaller load steps and ultimately, convergence of every analysis (found in this particular model to not always be the case for displacement-control).

It is assumed in the physical setup that the edges of platens remained in plane and that the load application remained constant along the edge of the platen. A vertical platen remains vertical, with no rotation and a horizontal platen will remain horizontal with no rotation. This enables a simple way of load application, a master and slave system. This means that one node is prescribed as the master and the surrounding nodes act as slaves to that prescribed node. In the model the load is applied to one node and the other slave nodes follow this node. This means that for all these slave-nodes, the displacement would be equal to the master node. This master and slave system is built into the model in DIANA by the use of "tyings."

4.4.1. Non Linear Solution – Iteration Processes

As the system response is non-linear, an iterative solution process is called for. Iterative solutions work by the prediction and subsequent correction of results. Such a non-linear solution is called an incremental-iterative solution. The stress-strain relationship is incrementally updated, Eq. [10], Figure 41.

$$[\Delta\sigma] = [E]\{\Delta\varepsilon\} \qquad [10]$$

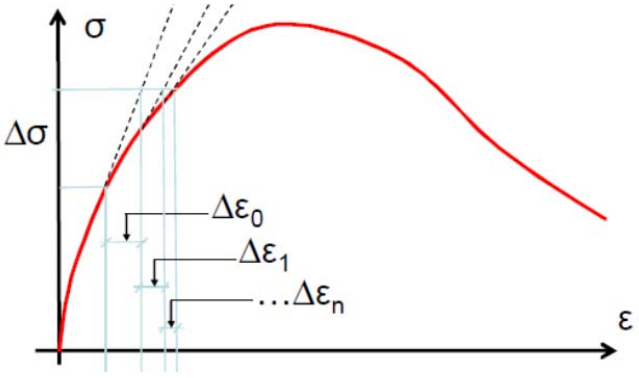

Figure 41 - Non-Linear Iterative Solution Process

Firstly, ordinary iteration processes can have the effect that the predictions for displacement increments become excessively large, especially if the prescribed load increment is fixed. This problem is overcome with the use of an Arc-length method (a form of Newton-Raphson iteration), which means, in effect: snap through or snap back behaviour can be analysed, DIANA User's Manual – Analysis Procedures. The advantage is that the analysis can pass a snap back point, Figure 42, and continue the analysis until failure, unlike deformation control, which cannot.

With regard to other available methods (such as Newton-Raphson), this over estimation of displacements proved to be a problem in preliminary analyses and the Arc-length Method (using load-control) yielded better (and faster) convergence than other iteration methods (using displacement control).

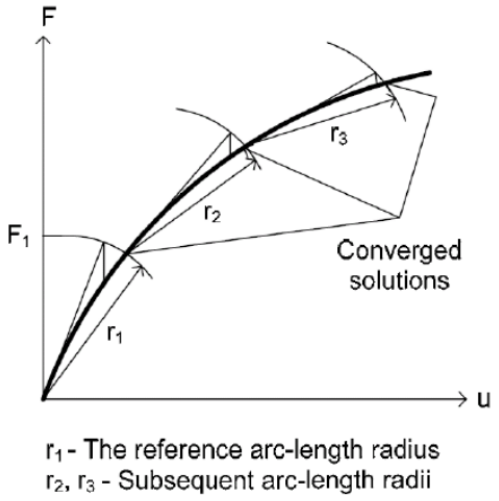

Figure 42 - Arc-length Method

Two methods of iteration are available within the Arc-length method, the Spherical Path Method and the Updated Normal Plane Method. The latter was implemented in the analysis.

A simplistic explanation of the procedure would be that the Arc-length method (specifically the Updated Normal Plane Method) constrains the norm (the radii, Figure 42) of the incremental displacements to a prescribed value. This is done by the simultaneous adaptation of the size of the increment within the iteration process. It should be noted that the increment size is not fixed at the start of the increment.

The starting point would be that there is a defined external force vector and an increment of that external force vector. For every iteration step, the incremental vector's load factor is then updated.

Geometrically this constraint means that the increment must be perpendicular to the total increment at the previous iteration, hence the method is called the Updated Normal Plane Method, DIANA User's Manual – Analysis Procedures, Release 9.4, Dec 4, 2009.

4.5. FE Model Schematisation

Figure 43 shows the schematisation of the proposed biaxial FEM model. The interfaces, master nodes, supports and the slave nodes can be seen.

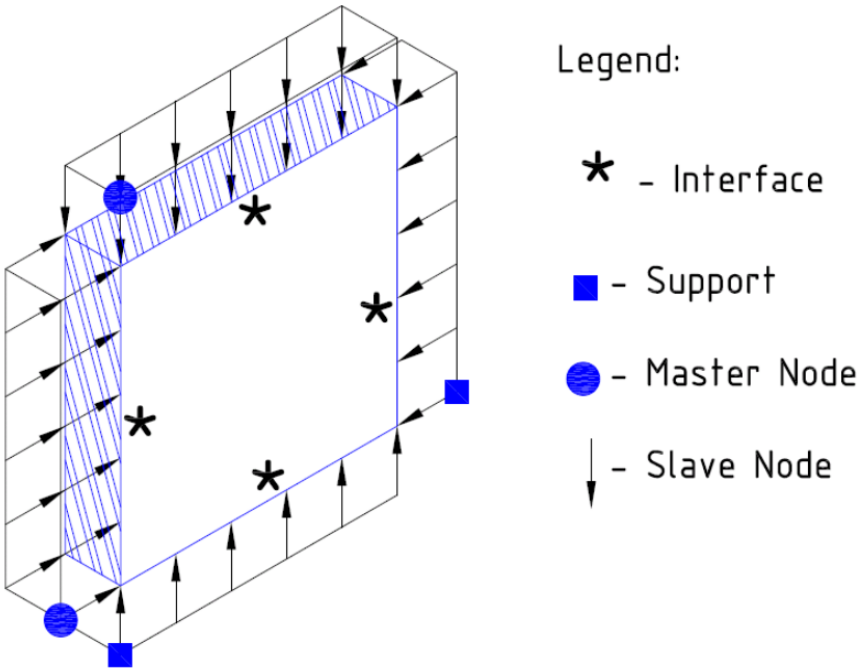

Figure 43 - Schematisation of proposed biaxial model

4.6. Finite Element Model Results

Whereas Figure 3 shows the load ratios applied in physical tests, where the term "load ratio" represents the ratio of magnitude of the applied load and magnitude of the applied load in the orthogonal direction, Figure 44 shows the load application ratios for the Diana FE model.

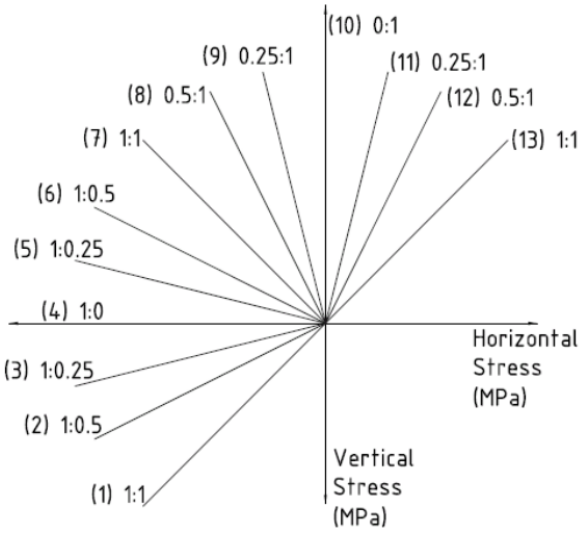

Figure 44 - Load application ratios used in Diana FE model

The material properties for all materials used in the Diana FE model are given in Table 3.

Table 3 - Material properties - parameters used in Diana FE model

Material	Parameters
Concrete	σ_C = 30 MPa
	gc = 10 N/m
	E = 12 GPa
	v = 0.3
	σ_{TY} = 3 MPa
	σ_{TU} = 5 MPa
Steel platens	E = 200 GPa
	v = 0.32

Interfaces	k_s = 3 MPa k_n = 10 GPa

Table 4 - Finite element results (Refer to Figure 3 for test points P1-P13), Diana analysis

	P1	P2	P3	P4	P5	P6	P7	P8	P9	P10	P11	P12	P13
σ_X (MPa)	-35.4	-35.3	-33.0	-30.1	-17.3	-7.9	-3.6	-1.8	-0.9	0.0	0.9	1.7	3.4
σ_Y (MPa)	-35.4	-17.7	-8.5	0.0	4.5	3.9	3.7	3.6	3.5	3.5	3.5	3.4	3.4

Table 4 gives the results from the Diana FEM analysis. These values are plotted to give the failure envelope, Figure 45. The computed ultimate resistance values are shown together with physical test results done on SHCC, using solid load platens (same loading platen type as in the model). Note that the physical data is only for the compression-compression zone, Figure 45. The biaxial failure envelope for each zone, compression-compression, compression-tension and tension-tension is discussed along with hardening, softening and confinement behaviour.

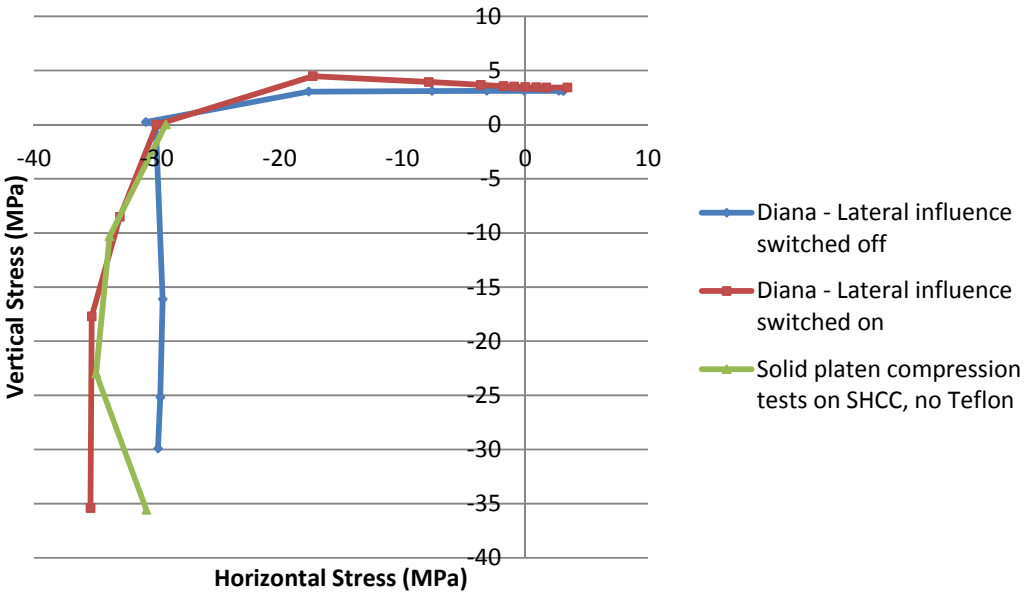

Figure 45 – Biaxial failure envelope of FEM results (Diana analysis) compared to physical tests without Teflon

4.6.1. Biaxial Compression

Stress vs. deformation curves were obtained for each of the compression-compression load cases (compression zone, Figure 44) in both principal directions of loading. Figure 46 shows the compressive results and will be used to discuss the uniaxial and biaxial load ratios. Note that only the horizontal results are given for the discussion. The horizontal load is considered the dominant direction of loading.

Figure 47 shows the failure envelope for compression-compression and will be used to discuss confinement and biaxial strength in compression.

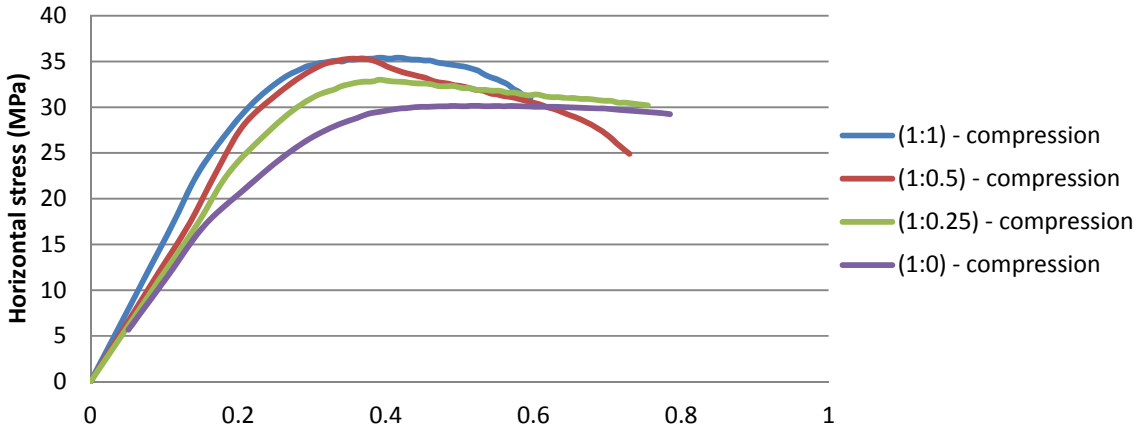

Figure 46 - Horizontal stress vs. horizontal deformation (compression-compression), Diana analysis

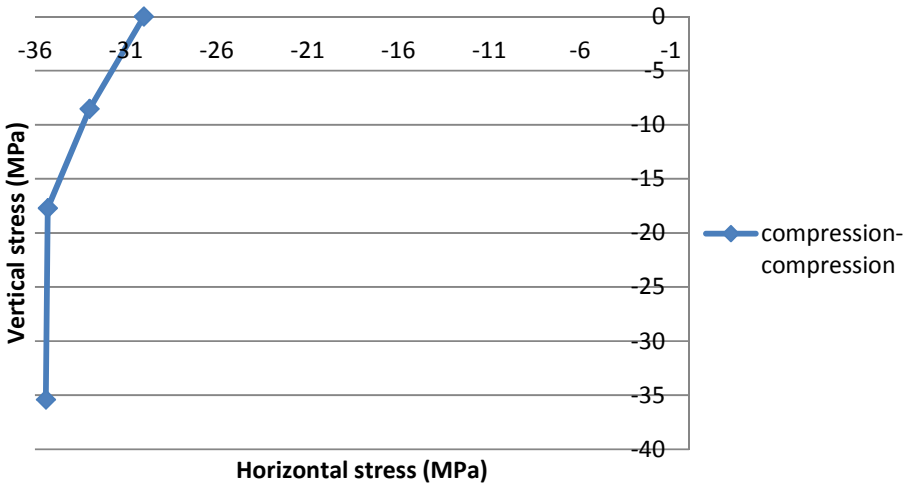

Figure 47 - Biaxial failure envelope (compression-compression), Diana analysis

4.6.1.1. Uniaxial Compression

The uniaxial FEM result yielded a compressive stress peak of 30.01MPa, Figures 46, 47. With reference to the loading scheme, this is the point 4 in Figure 44, noting that in this zone the dominant stress is horizontal. The model yielded an accurate uniaxial strength for SHCC.

4.6.1.2. Biaxial Compression

Referring to Figure 46, the curves indicate, clearly, that there is a definite increase in strength in the biaxial ratios of load application. The highest strength values are obtained at ratios of $\sigma_2 = \sigma_1$ where σ_1 is the dominant, horizontal stress. This is an expected result as others have found this maximum stress to be at a ratio of 0.5 and lower (Yin et al. 1993, Hussein and Marzouk, 2000).

Figure 47 shows how the confinement effect, increases the biaxial strength by about 23%. This result is similar, although somewhat larger than that found by physical testing of SHCC, using solid testing platens. The computed curve simulates the physical results (Figure 45) closely, except for the ratio of 1:1. This ratio should not have a larger strength when compared to the other. A study by Swaddiwudhipong and Seow (2006) on modelling steel fibre cement composites yielded similar looking curves (experimental and predicted), Figure 48.

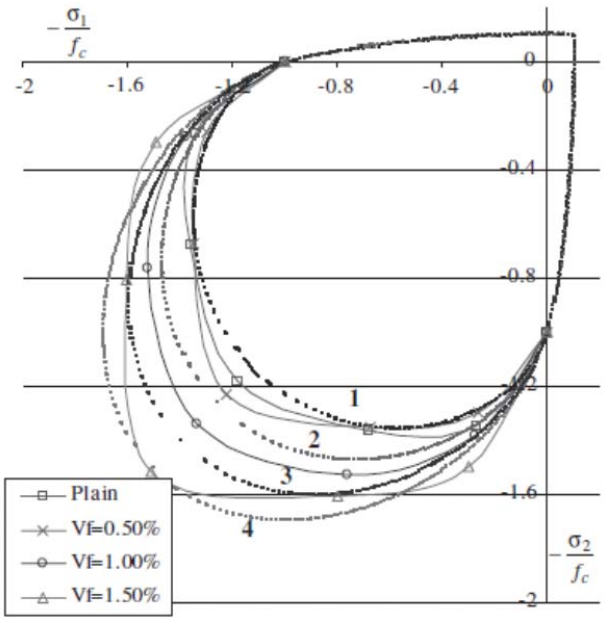

Figure 48 - Experimental and predicted (model) biaxial curves (Swaddiwudhipong and Seow, 2006)

4.6.2. Biaxial Compression-Tension

Figures 49, 50 and 51 show the results for the tension-compression zone. The tests in this zone correspond to the points 4 through 10 in Figure 44. The loading ratios vary from horizontally dominant (higher curves) to vertically dominant (lower curves) in Figures 49 and 50. Horizontal stress represents compression and vertical stress represents tension.

Figure 49 gives the horizontal stress vs. horizontal deformation of the tension-compression zone. It can be seen that the stress range is in the order of about 18MPa, as compared to Figure 50, where the stress range is much smaller.

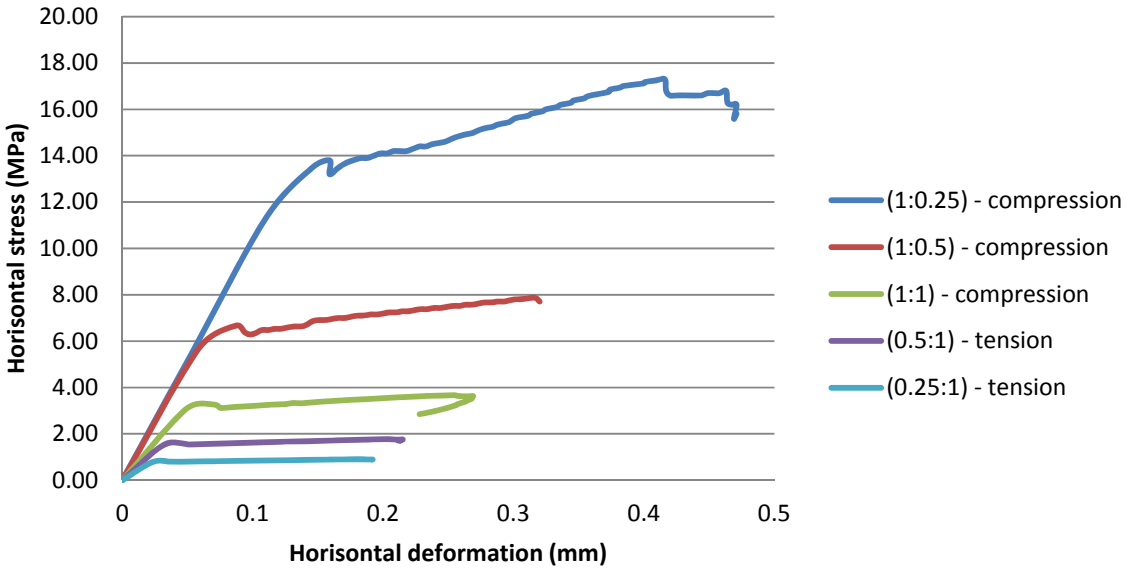

Figure 49 - Horizontal stress vs. horizontal deformation (compression–tension), Diana analysis

Closer inspection of the curves (Figure 49) where the horizontal stress is dominant yields that hardening does occur in compression, this could be as a result of the influence brought about by the tension in the other principal direction. All three curves show an initial weakening, followed by an increase to a later peak and consequent failure.

The results for vertical stress vs. vertical deformation are given in Figure 50. As can be seen, the peak stress range is in the order of 1 MPa, the curves are much more closely spaced and all five curves show hardening behaviour.

It should be noted that for the tests, the tension strength was the limiting factor and because the concrete is much weaker in tension than in compression, the curves in Figure 50 have a smaller range than in Figure 49. From Figures 49 and 50, it can be concluded that the ductility in tension is reduced with increasing orthogonal compression.

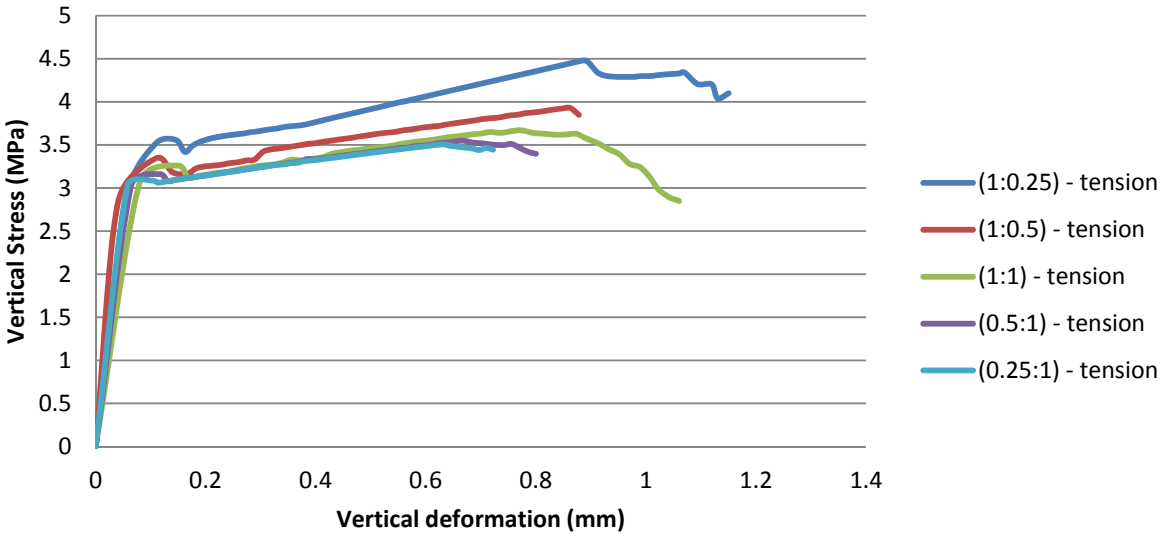

Figure 50 - Vertical stress vs. vertical deformation (compression-tension), Diana analysis

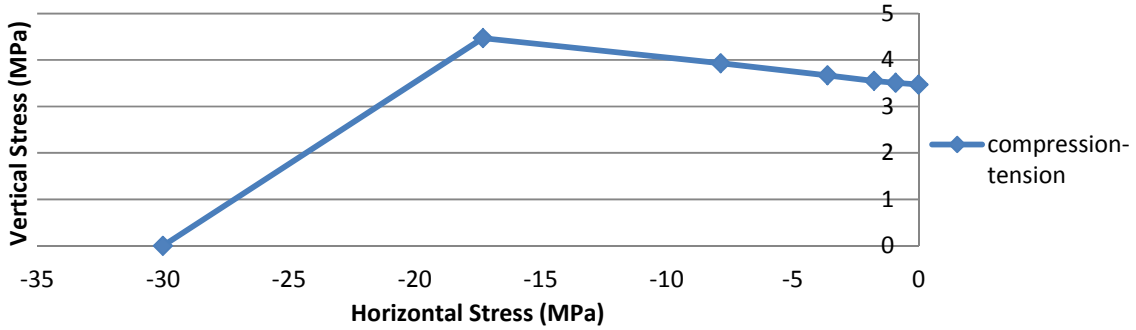

Figure 51 - Biaxial failure envelope (compression-tension), Diana analysis

Inspection of Figures 50 and 51 shows that in compression-tension, the strongest biaxial (vertically) ratio is 1:0.2558. Of importance is the fact that the curve does not strictly follow the Rankine-Von Mises limit function, shown in Figure 34, and clearly shows that there is a difference in vertical strength at different load ratios. This indicates an increase in biaxial strength brought about by the confinement effect.

It can be noted that the distribution of the points is not as exactly placed on the loading ratios (Figure 44) as it seems to be in compression tests (Figure 45). This is discussed in physical test results, section 5.

4.6.3. Biaxial Tension

4.6.3.1. Biaxial Tension-Tension

Figure 52 shows horizontal tensile stress vs. horizontal lengthening curves that show similar spreading to that found in Figure 49. In Figure 52, higher strengths are reached at higher ratios. As discussed above, this occurs due to the dominance of the horizontal and vertical axes changing as the load in either direction is increased. As the ratio of load application increases, so the influence that that axis has increases.

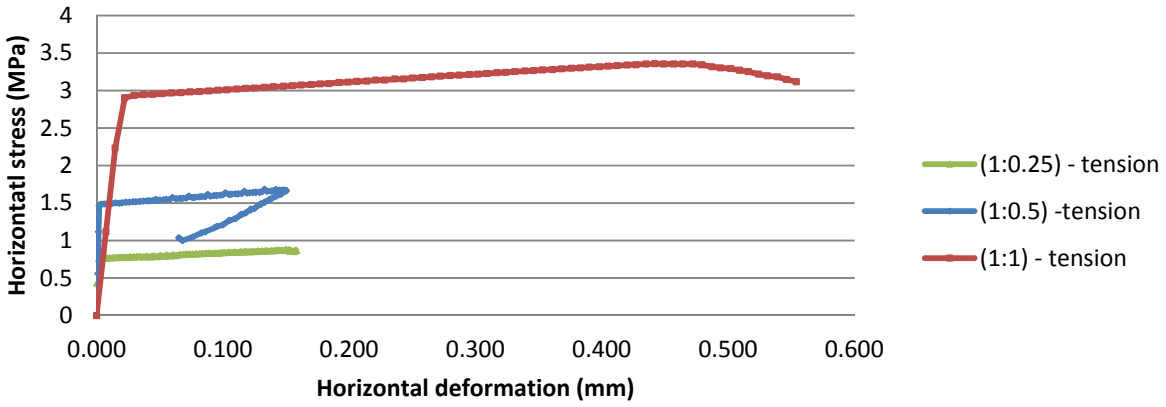

Figure 52 - Horizontal stress vs. horizontal deformation (tension-tension), Diana analysis

Figure 53 shows the vertical stress vs. vertical displacement for the tension zone.

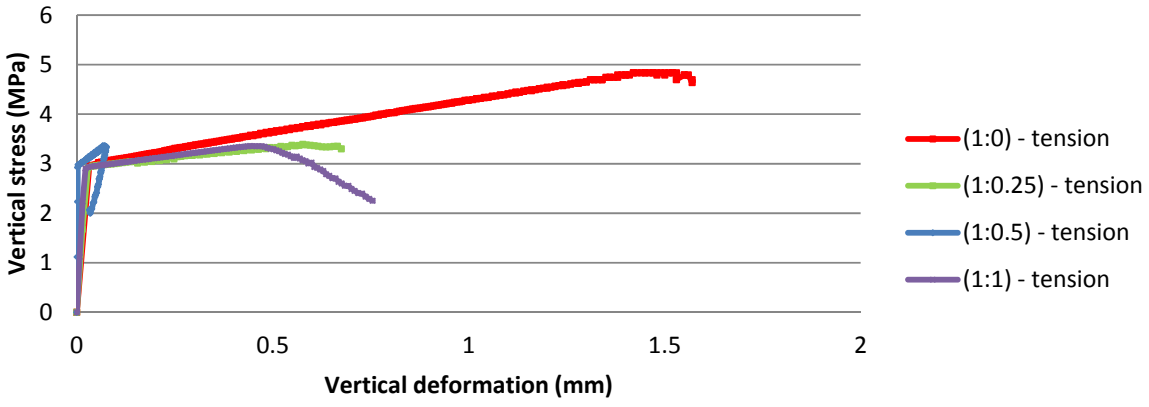

Figure 53 - Vertical stress vs. vertical displacement (tension-tension), Diana analysis

Figure 54 shows the biaxial tension-tension failure envelope. Comparing Figure 54 to the tension-tension zone in Figure 34 (the Rankine-Von Mises limit function); the biaxial tension failure envelope does not strictly follow the limit function.

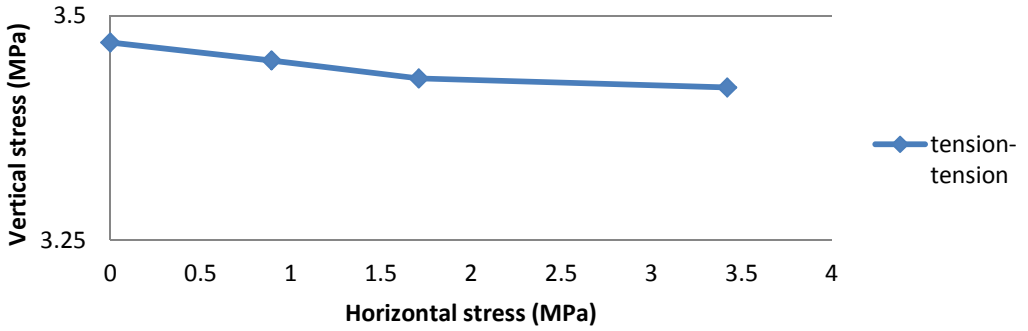

Figure 54 - Biaxial failure envelope (tension-tension), Diana analysis

4.6.3.2. Uniaxial Tension

Figure 55 shows the results of a uniaxial tension test (vertical) performed in Diana. If Figure 55 is compared to Figure 33 (the input stress-strain law), it is reassuring to note that it can be seen that the response is exactly the input. A linear-elastic zone is followed by hardening until a peak stress of 4.84MPa (1.42mm deformation), where after softening follows.

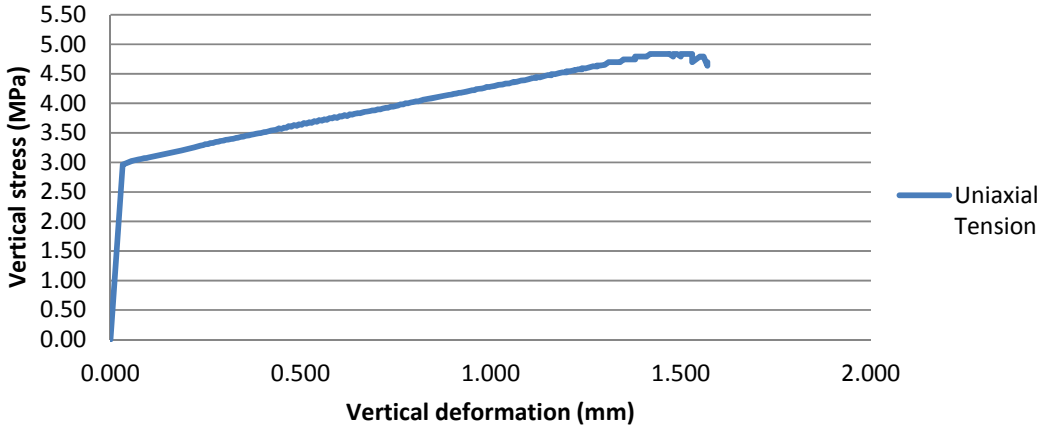

Figure 55 - Vertical stress vs. vertical deformation (tension only), Diana analysis (Point 10, Figure 44)

From Figure 55, the yield point can be calculated as σ_Y = 2.96MPa with a corresponding vertical deformation of 0.032mm/mm.

4.6.4. Completed Failure Envelope

Figure 56 shows the complete failure envelope which was obtained by the Diana analysis.

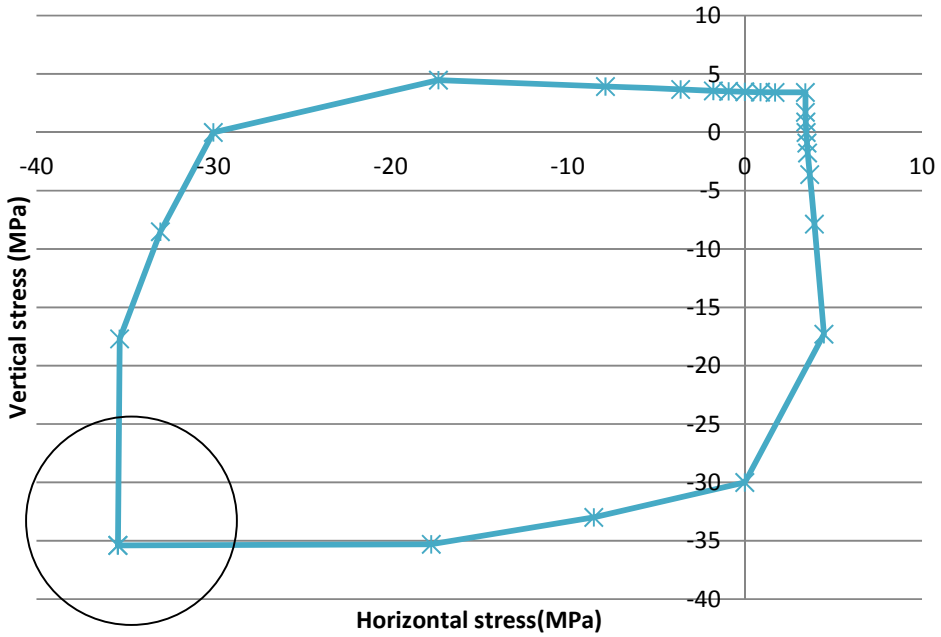

Figure 56 - Complete biaxial failure envelope for SHCC, Diana analysis

Figure 56, the complete biaxial failure envelope is obtained from Figures 47, 51 and 54. The only objection would be the area shown in the circle in Figure 56. From results, physical and numerical, by others, see Figures 2 and 48, this area is often curved, i.e. the ratio 1:1 is usually not the ratio with the highest biaxial resistance value.

This could mean that the maximum stress ratio is within this circled area and more test points are needed to show if the line is in fact curved and not straight. Five more test points are added and the new higher resolution curve is given in Figure 57.

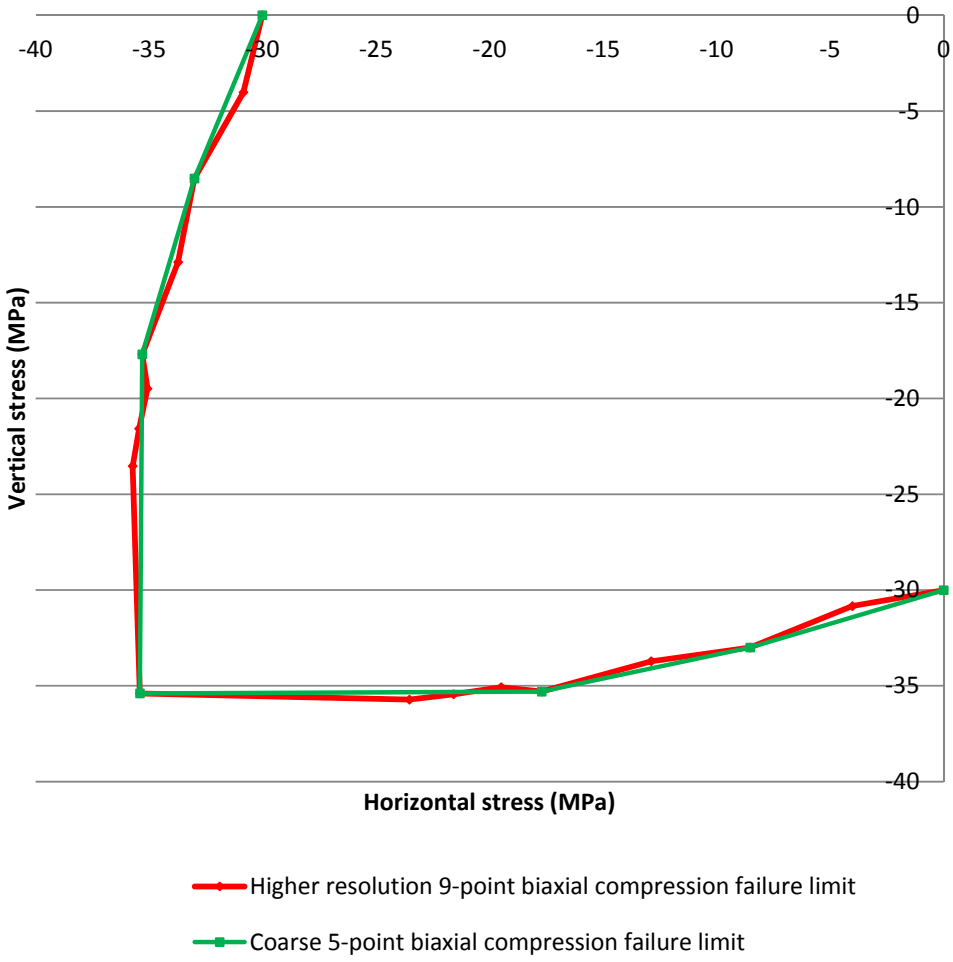

Figure 57 - Higher resolution biaxial compression curve, Diana analysis

It can be seen in Figure 57 that a higher resolution only slightly improves the solution near the 1:1 ratio, however, a slight curving of the red line can be noticed in area close to the 1:1 ratio.

4.7. Improvements to tensile load application FE model in tension

In the original model, the load was transferred onto the specimen by means of load control by applying a load to a master node on each of the sides of the sample. The slave nodes then followed the master node. The load application occurred at the sample edge, therefore, in the tension quadrants the effect of the jaws that grip the sample, Figure 23, around the sides on the sample were ignored. The improved model is changed to apply the load at the edge of the jaws. Note that the restraint caused by the jaws in the out-of-plane direction is not included. Figure 58 shows the load application.

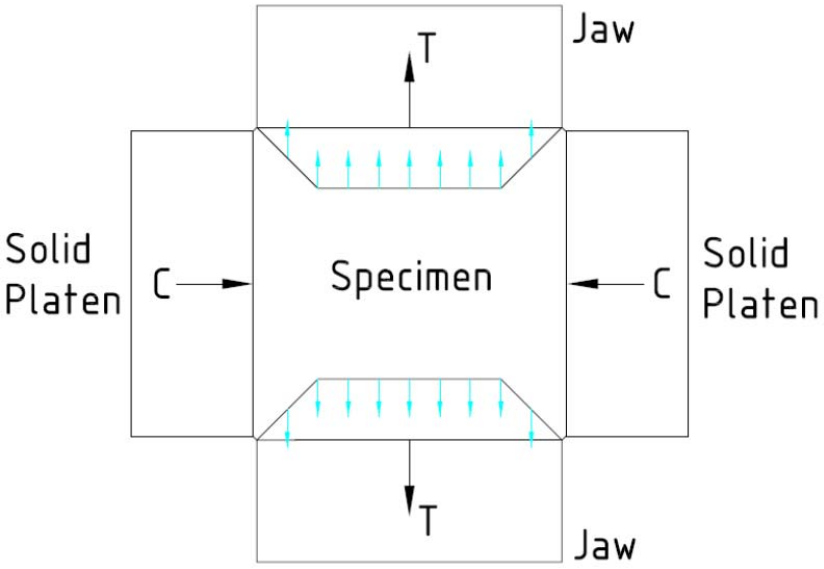

Figure 58 - Compression-tension scenario showing loading at tension jaw edges

By correcting the specific loading conditions in the model for the tensile tests, a more realistic stress distribution may be calculated, as would occur in the specimens in the physical experiments.

The failure patterns in the physical tensile tests indicate an influence of the non-uniform stress distribution in the specimen close to the jaws. The localising, failure crack occurred close to the tension jaws in most tensile specimens, in both tension-compression and tension-tension. This, together with a limited number of cracks formed in tension, may be ascribed to the non-uniform stress distribution in the jaw region.

4.7.1. Stress Uniformity

It was assumed for the original model that a uniform stress distribution exists as a result of the loading (simple loading), within the specimen. With the tension jaws in place, the stress distribution is no longer uniform as the loading is applied onto the nodes on the SHCC specimen at the platen edge (corrected loading), see Figure 58.

A Diana result from the compression-tension zone, point 5 (Figure 44), is investigated in order to show the non-uniform stress distribution. Figure 59 shows the variation in vertical stress along the breadth of the specimen (at 25mm from the edge of the sample, roughly a quarter of the total specimen height) for the simple loading and corrected loading.

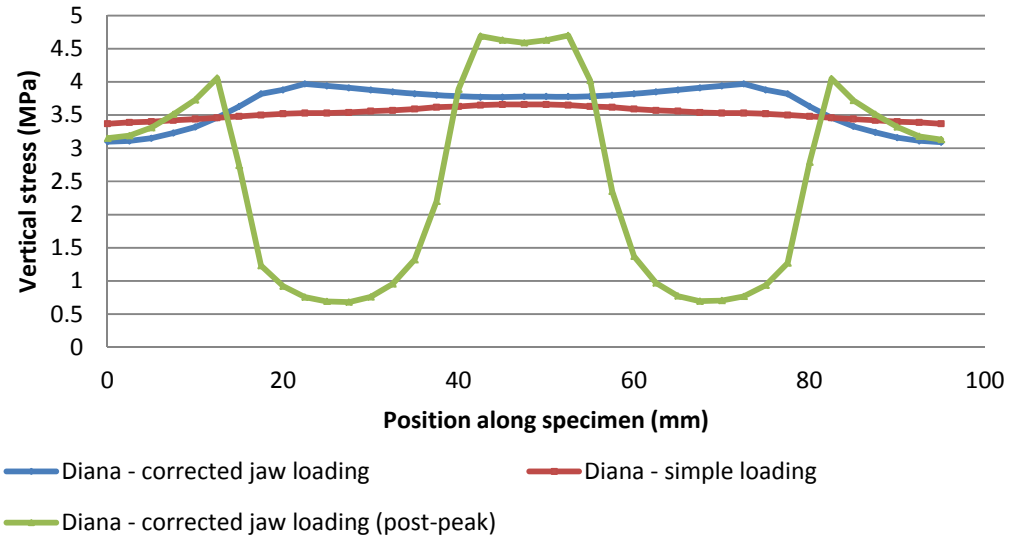

Figure 59 - Vertical stress variation along specimen breadth (Point 5, Figure 44)

Three curves are shown in Figure 59. The red curve represents the simple loading case, it can be seen that there is a slight variation (0.3MPa or 9% variation), indicating that for simple loading the vertical stress variation is close to uniform. The blue curve represents the corrected jaw loading case, where it can be seen that the variation is much bigger (0.72MPa or 23% variation), indicating that the stress variation is no longer uniform.

The red and blue curves both depict the stress distribution in the specimen at the load peak. The green curve represents what the blue curve becomes, post-peak. At the peak, the elements on and close to the jaw edge (the load was applied to these elements) fail and after the peak the stress around these elements becomes excessively large and the entire specimen fractures along the jaw line.

The shear stress along the breadth of the specimen is given in Figure 60. Again, three curves are shown, the red curve represents (peak) shear stress for simple loading and the blue curve represents the corresponding shear stress for the corrected loading. It can be seen from the blue curve that the shear stress in the corrected loading case is irregular, with the green curve representing the post-peak exaggeration of the influence of the jaw edges.

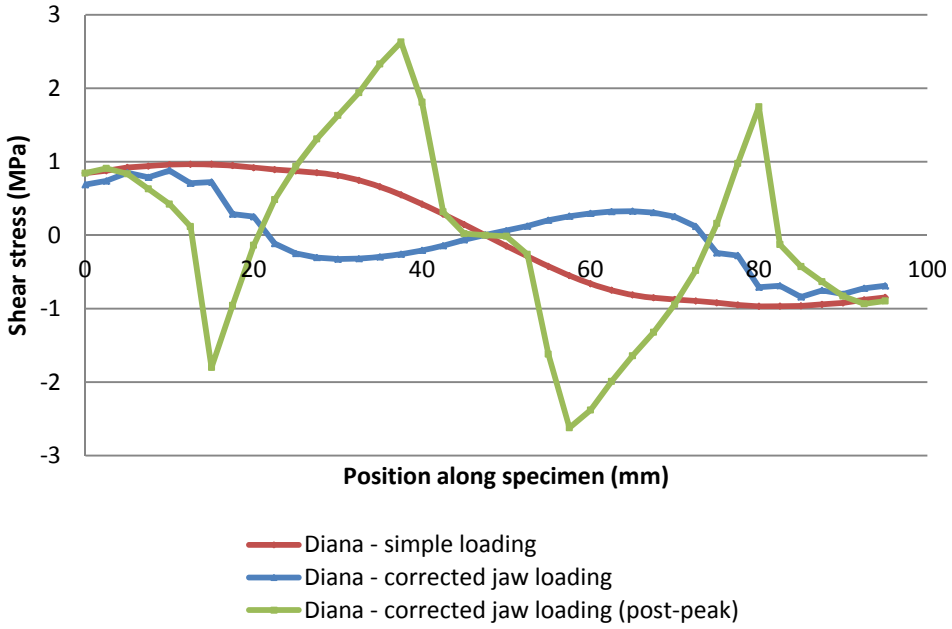

Figure 60 - Shear stress variation along specimen breadth (Point 5, Figure 44)

4.7.2. FEM model failure envelope – correct loading

An analysis was performed after the tension jaws were incorporated into the model and the result obtained is given in Figure 61 alongside the original result. By inspection of Figure 61 it is clear that there is a difference in tension strength of the Diana models and the physical tests. This is because at the creation of the model, the ultimate tensile strength was given as 5MPa, which would be the case for a standard tension test. As the biaxial setup test specimens cross sections are different from the standard dumbbells, so the tension capacity will differ. The Diana model could be tailor fitted to the physical results, after they are known, so as to be used as a predictive model.

Noticeable on Figure 61, is the significant increase in tensile strength between the specimens with simple loading (green curve) and corrected loading (red curve). The non-uniform stress distribution will weaken the specimens and should thus give a lower tensile strength, which is the opposite of what is seen in Figure 61.

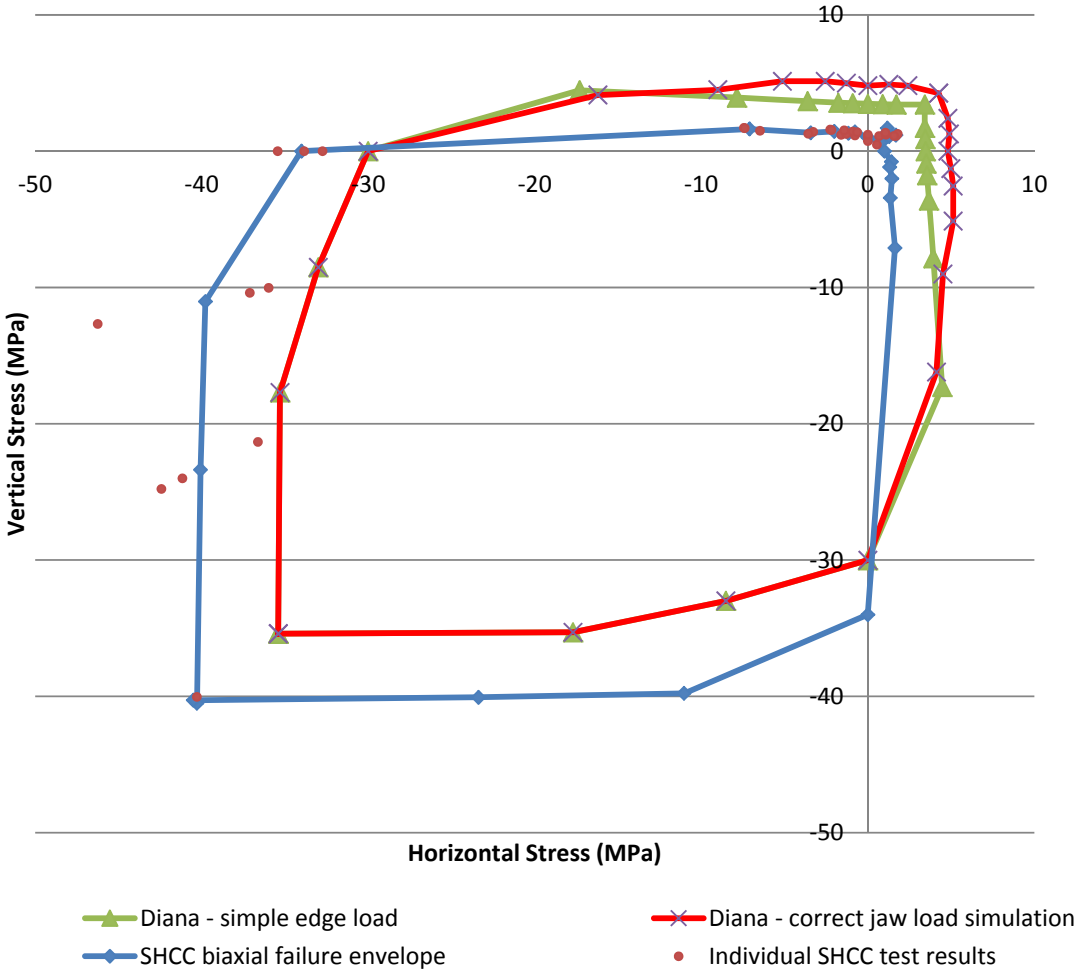

Figure 61 - Biaxial failure envelope comparison, numerical and physical results

If a non-uniform stress distribution causes a smaller tensile resistance, the red curve (corrected loading) should be inside the green curve (simple loading). The question is whether this is a numerical problem or if the "shortening of the effective length" over which the tensile stress acts is the cause. The principal stress concentrations are investigated on the specimen face and shown in Figures 62 and 63, respectively.

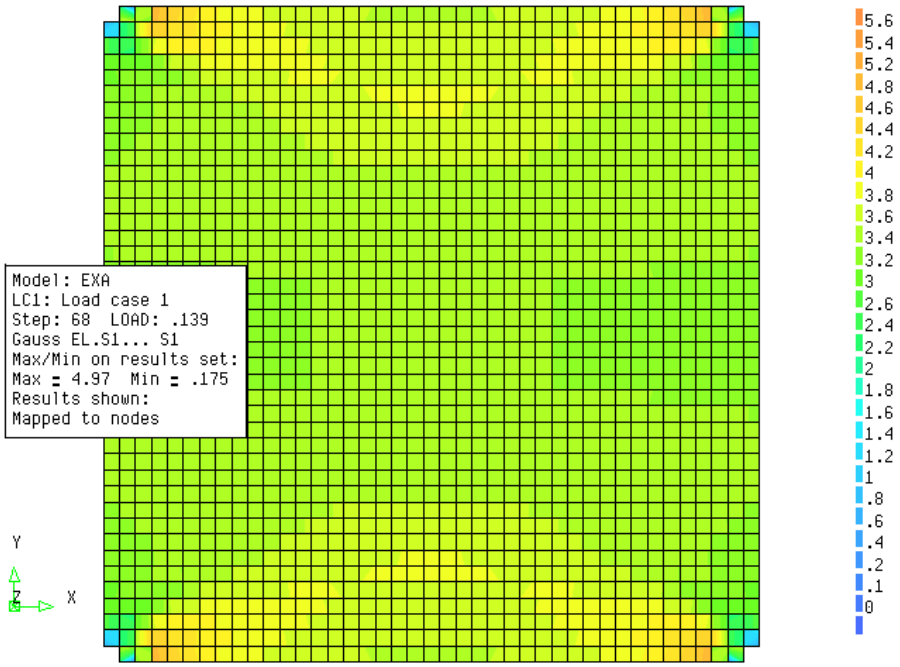

Figure 62 - Principal stress levels (MPa) in specimen, simple load application (Point 5, Figure 44)

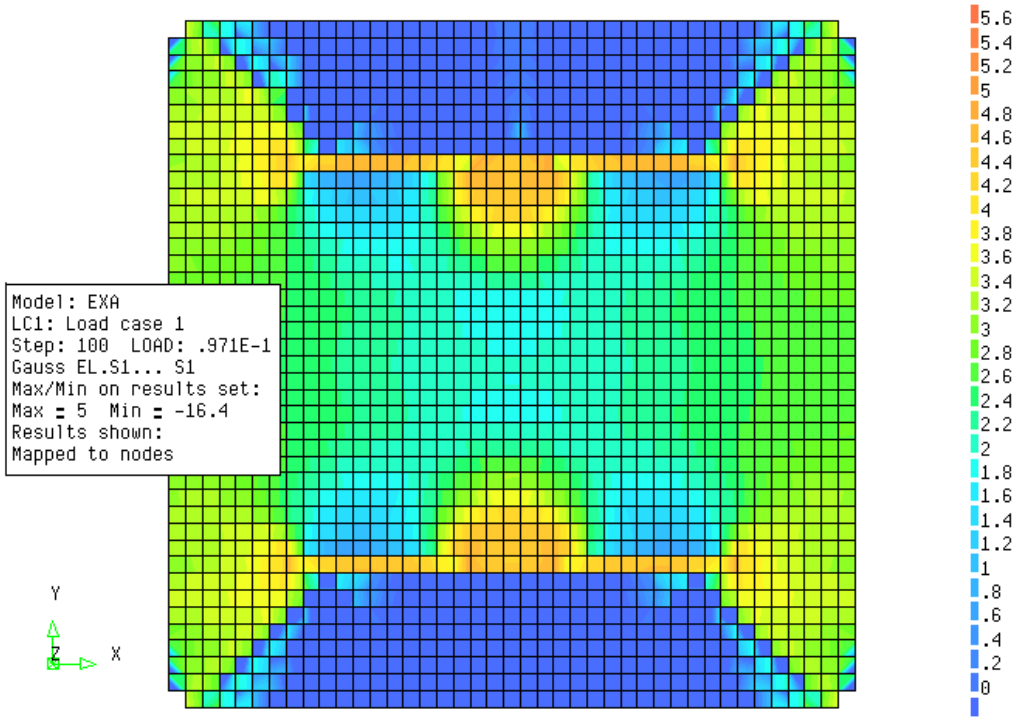

Figure 63 - Principal stress levels (MPa) in specimen, correct load application (Point 5, Figure 4)

Figure 62 shows the principal stress (vertical stress) distribution for the simple load case, depicted by the red curve in Figure 59, visually. Figure 63 shows clearly the effects of the jaws. If the stress values are compared, it is clear that higher stress values occur in Figure 63, around the jaw edges and specifically at the corner of the jaws. The blue regions inside the jaw show, as expected, that the material is in compression.

If the centre region of Figure 62 is compared to that of Figure 63, the average principal tensile stress in Figure 62 is 3MPa, and the average principal stress Figure 63 is 3.6MPa. This result confirms with a visual representation that the peak stress in the specimens tested with the jaws is higher than for the simple loading. It is proposed that this is as a result of the "effectively smaller" specimen size as a result of the jaws which decrease the effective length of the specimen by 40%.

4.8.Discussion

4.8.1. Compression

Analysis of the compressive model yields results that agree with the parabolic compressive model input, Figure 46, as prescribed in Figure 33.

Inspection of the compression-compression zone in Figure 47 shows how the model clearly incorporates the effects of confinement, whilst also portraying the ideal concrete behaviour successfully. The total strain model and selected stress-strain laws simulate the biaxial compressive behaviour of SHCC to some extent, with the largest discrepancy at the compressive biaxial stress ratio of 1:1.

4.8.2. Tension

Strain hardening behaviour is exhibited in cases where tensile stress is present, Figures 49, 50, 52, 53 and 55. The tension model was prescribed to model hardening behaviour, followed by softening behaviour. Figure 53 and 55 show that softening behaviour does occur, most clearly for the case of $\sigma_2 = \sigma_1$. Thus the conclusion is made that the tension behaviour of the material follows the model input.

4.8.3. Failure Envelope

Referring to Figures 47, 51 and 54, the confinement effect is modelled successfully; the model shows a very pronounced increase in biaxial compressive strength. The model results seem to concur with model data done by others (Swaddiwudhipong and Seow, 2006) and the general shape of physical data.

The result indicates that point 1 ($\sigma_2 = \sigma_1$) has the highest biaxial strength, which disagrees with the results found by others, (Van Mier, 1984, Ehm and Schneider, 1985, Yin et al. 1990 and 1993, Hussein and Marzouk, 2000).

It is important to note that the model in Diana can only be used if specific material models such as cracking, confinement and material law are part of its library where material behaviour has to be prescribed by the user. The model used in this study does not perfectly match measured response of SHCC in Figure 61 (results are also somewhat unconservative). Higher stress values were obtained than physical testing, meaning a different failure envelope, but the analysis did yield an expected shape.

Comparison between the numerical model results and the physical results is thus not recommended as the input to the numerical model is based on uniaxial results and not biaxial results. A future study or investigation could be to use the physical data obtained in this study as an input to the numerical model. The input will no longer be of standardised test results but of the biaxial test results. This would yield a new failure envelope which should match the failure envelope obtained from physical testing more closely and thus could be used for comparison. The results obtained from the numerical model are thus not compared to physical results in this thesis.

5. Biaxial Experimental Results

5.1.Summary of Experiments

A total of 39 samples were tested in the biaxial setup. At each point on the curve in Figure 3, three SHCC samples were tested. The samples were cast, allowed to cure in 100% humidity and cut to size as described in section 3.5. The age of the concrete at testing was 56days. See Appendix E for results.

5.2. Biaxial Strength

As described in section 3.4, the specimen deformations are captured optically with a 3D optical measurement system, Aramis, during the biaxial test. The hydraulic system enables one to plot stress in time and the optical system enables one to plot strain in time. The two data sets are then synchronised to yield stress-strain curves.

5.2.1. Compression-Compression

5.2.1.1. Stress

The biaxial stress results for the compression-compression zone are plotted alongside previous testing data in Figure 64.

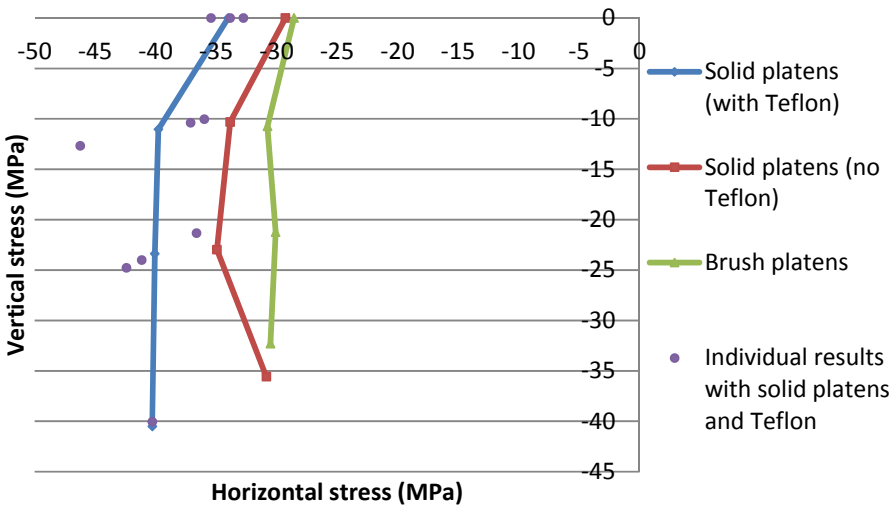

Figure 64 - Biaxial compression failure envelope

The clearly noticeable differences in the biaxial strength curves are brought about by the different boundary conditions investigated and the fibre orientation as discussed in section 2.6.1. Solid mild steel

platens were compared to brush-type platens for thin-cast specimens (2D fibre orientation). The result is given alongside that of cast and cut specimens (3D fibre orientation) the combination of solid mild steel platens with Teflon strips between the platen face and that of the specimen.

It is very important to note that the curves for solid-and brush-type platens without Teflon were for cast samples and not for cut samples as is the case for the solid platens with Teflon tests. Thus, there is a difference in general in the strength between the samples, cut samples yielding higher strengths, refer to section 3.5.2 for discussion on the fibre orientation effects on resistance.

It is clear from the results that the brush-type platens yield the lowest results, this is due to penetration and deformation of the bristles of the platens, refer to the discussion in section 3.6.

There is a marked difference in attained compression strength between the tests performed with solid platens (without Teflon) and the combination of the solid platens with Teflon sliding layers. The idea of the Teflon sliding layers is to minimise the frictional force between the sample and the loading platen. This avoids friction-induced confinement, which has been shown by several authors to lead to higher apparent compressive strength. This indicated that the strengthening by fibre alignment also in the thickness direction is dominant. It is expected that the use of solid platens without Teflon to test cut specimens will lead to higher apparent strength than shown with the blue curve.

Whereas the green and red curves are the test results for solid platens without the use of Teflon, the results are from thin-cast specimens (2D fibre orientation) and not larger cast and then cut specimens (3D fibre orientation). Thus they cannot be directly compared to the blue curve.

What is noticeable in all three cases, but less significantly for the cast specimens with brush platens, is the increase in biaxial strength compared to the uniaxial strength. This is further evidence of the confinement effect discussed in sections 2.4.1 and 2.4.2.

It can be seen on the blue curve that only one test result is given. This is because the other tests could not be completed as the specimens did not fail. In order not to damage the test setup, these tests were stopped.

Figures 65 and 66 show the stress-displacement relationships (horizontal and vertical) for test of ratio 1:0.577 (Point 2, Figure 3), obtained from the Instron actuators.

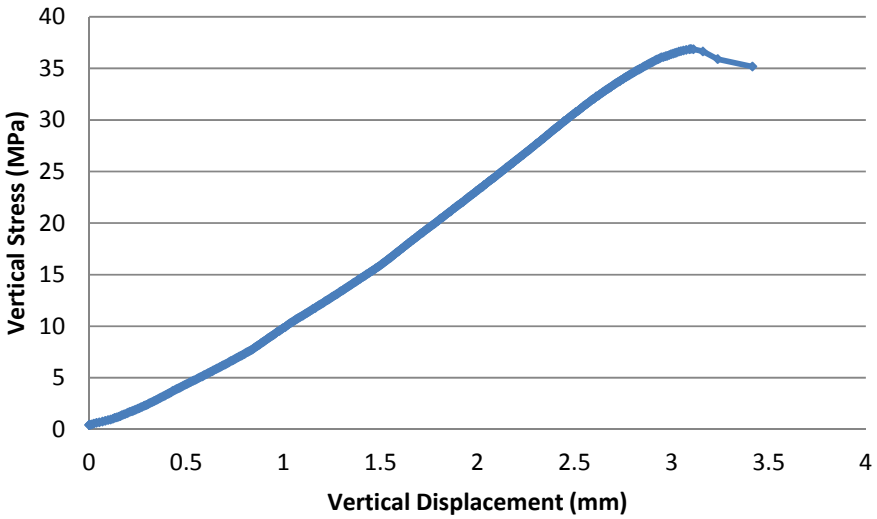

Figure 65 - Vertical position vs. load for test with load ratio 1:0.577 (compression-compression)

In Figure 65, the vertical actuator applied a compressive load on the specimen. The sample deformed by 3.1mm (shortened vertically), at a peak compressive strength of 36.89MPa. Figure 66 gives the corresponding horizontal behaviour.

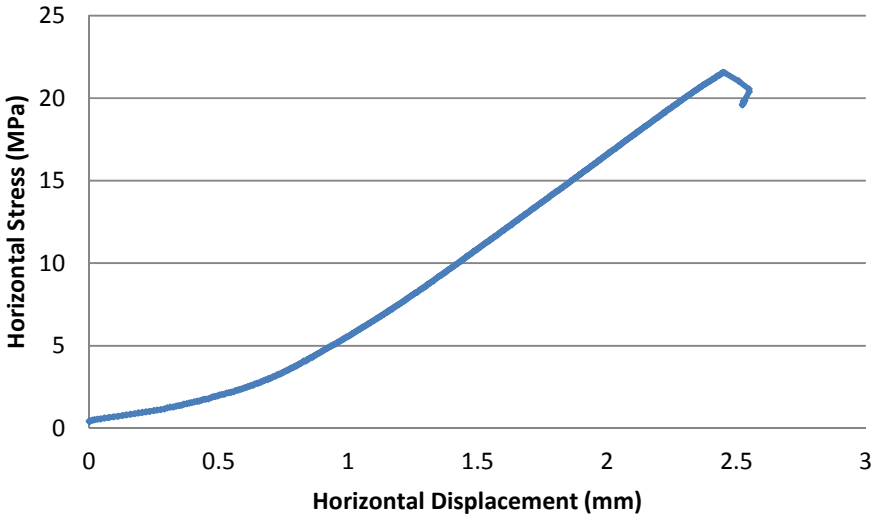

Figure 66 - Horizontal position vs. load for test with load ratio 1:0.577 (compression-compression)

In Figure 66, the horizontal actuator applied a compressive load on the specimen. The sample deformed by 2.45mm (shortened horizontally), at a peak compressive strength of 21.56MPa.

Noticeable in Figures 65 and 66 is the softening after the peak; where there is an increased deformation but at a reduced resistance. Figure 65 shows a longer softening branch before unloading, whereas in Figure 66, there is only a short softening branch before unloading starts.

5.2.1.2. Strain

Unfortunately it has to be reported that no strain information can be shown for the compressive tests as technical difficulties with the ARAMIS measuring system lens calibration prohibited the capturing of any useful results in the compression-compression zone at the time of testing.

Please refer to section 5.2.2.2 for a set of biaxial strain data in compression-tension.

5.2.2. Compression-Tension

In this zone, the vertical actuator applied a tensile force on the specimen and the horizontal actuator applied a compressive force. The failure envelope for this zone of testing is given in Figure 67.

5.2.2.1. Stress

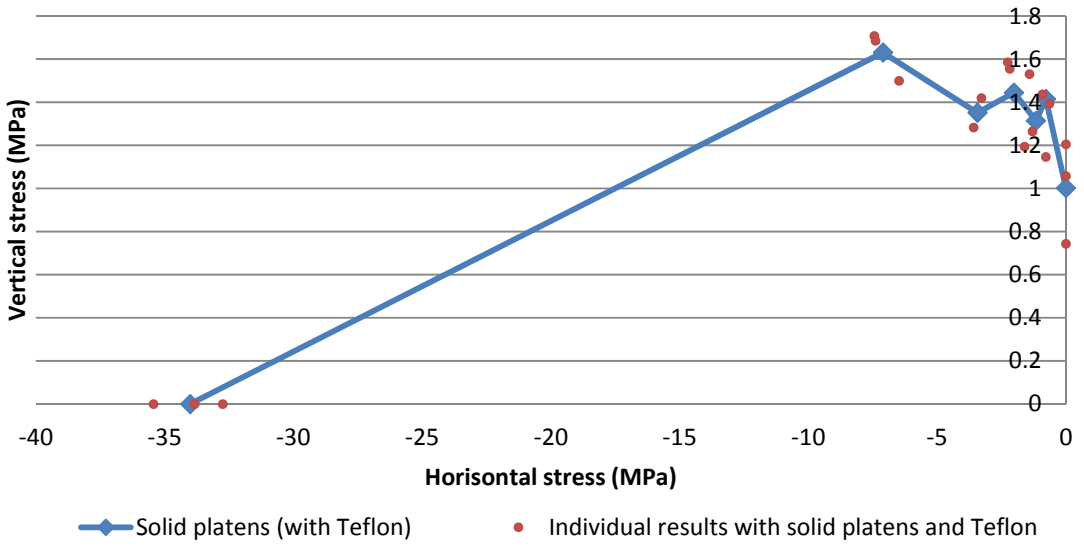

Figure 67 - Biaxial compression-tension failure envelope

If the curve in Figure 63 is compared to the Rankine limit function (tension limit function) in Figure 34, it becomes clear that the biaxial failure envelope result for the compression-tension zone is not merely a constant limiting function. This conclusion means, in effect, that the failure criterion function is more

conservative that what is actually possible in this zone. This implies that a new function should be determined for this zone, which allows for the confinement affect to be incorporated and does not simply limit the behaviour to a maximum principal stress.

Inspection of the curves in Figure 67 shows that the points at which failure occurred do not correspond to the points of loading indicated in Figure 3. This is as a result of the control of the hydraulic system. What this means is that the load is prescribed for the dominant actuator and a fraction of that load is prescribed for the other actuator. During the test, the two actuators apply the load independent of one another. A solution to ensure a more accurate load distribution would be for the dominant actuator to act as a master and the other actuator as a slave. This setup was not yet available during testing.

The result in Figure 67 shows that in the compression-tension zone, that the maximum strength occurs at a ratio $\sigma_v = 0.268\sigma_h$.

5.2.2.2. Strain

The strain results given by the Aramis system and the stress results given by the Instron system were synchronised for the strength ratio $\sigma_v = 0.268\sigma_h$ (Point 5, Figure 3). Figure 68 shows the vertical tensile stress-strain relationship.

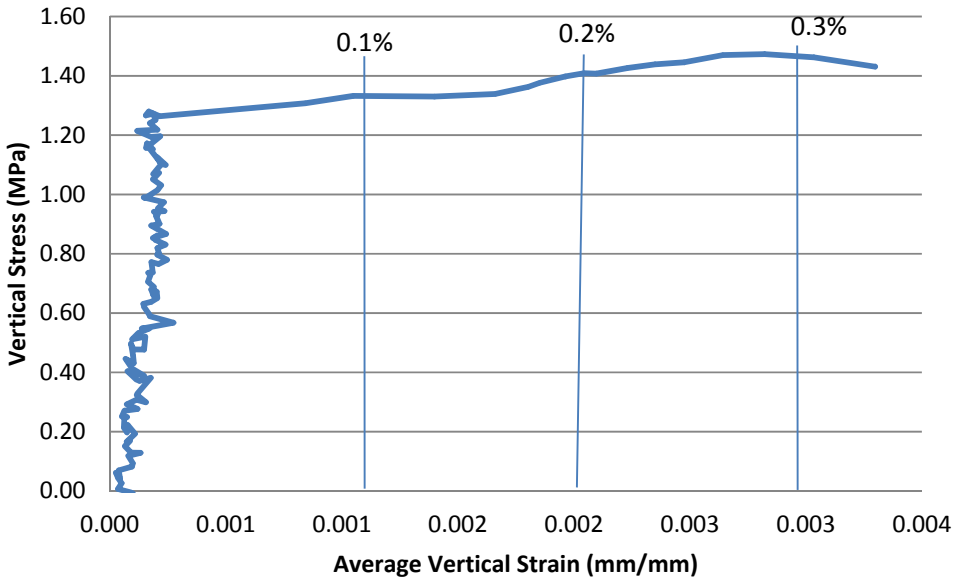

Figure 68 - Biaxial compression-tension stress-strain relationship for the vertical tensile axis (Point 5, Figure 3)

The horizontal stress-strain relationship (compressive) is not given as it is the tensile capacity (vertical) of the SHCC which was exceeded first at a corresponding compressive peak of 6.53MPa, which is far below the compressive capacity and within the linear-elastic zone.

The stress-strain curve in Figure 68, obtained from synchronising the ARAMIS results with the Instron results, is compared to the stress-strain curve found by using the Instron data (LVDT measurements are used to calculate strain) in Figure 69.

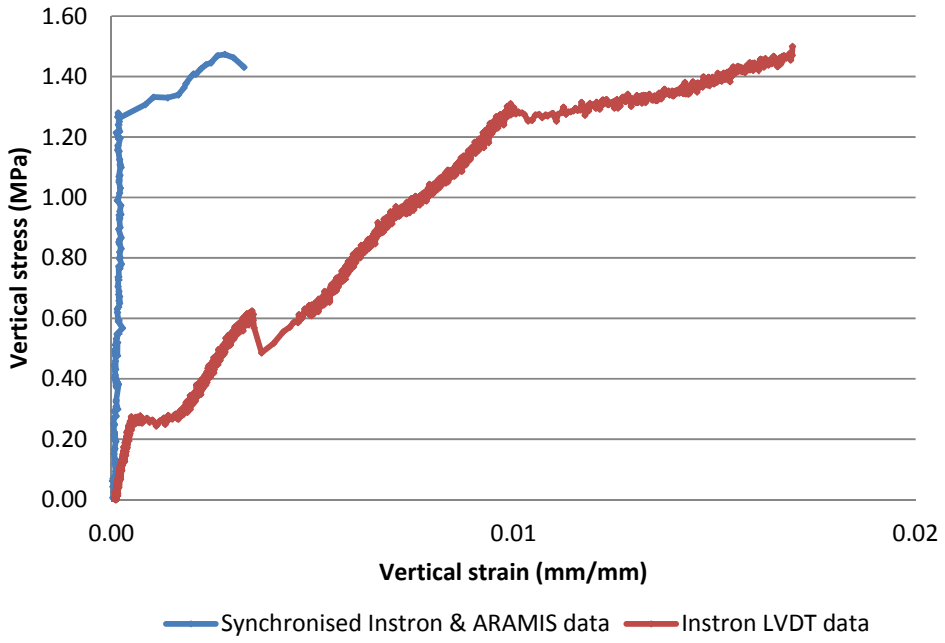

Figure 69 - Comparison of synchronised data (Instron & ARAMIS) stress-strain relationship and Instron LVDT data

In Figure 69, there is a clear difference in stiffness between the red and blue curve. The Instron actuator (red curve) measures total movement of the actuator face (with internal LVDT's) and the force is measured by an internal load cell. The red curve thus includes the small deflections undergone by the head-pieces and frame (section 3.2, Figures 21 & 22) as well as the deformation of the sample. The head pieces (and the setup) are not infinitely stiff and thus undergo some deflection. The Instron data can thus not be used independently of the ARAMIS data to represent strain because an incorrect stiffness, strain and thus stress-strain relationship will be obtained.

5.2.2.3. Cracking

Cracking as a result of the biaxial state of compression-tension (with tension vertically) was investigated by plotting deformation along a vertical line on the specimen. The deformation was investigated at 0.1% strain, 0.2% strain and 0.3% strain, refer to Figure 68. At the point of each of these respective strains, there is a specific time step in both the Instron and Aramis data and so, the deformation measured along the vertical line, for that particular time step can be found.

Plotting the deformation along a line on the specimen allows us to actually see where cracks occur, as well as tell us how wide the crack is. On the specimen face, a mask is defined in which Aramis measures deformation. This mask is then sectioned and results calculated at the sections, refer to Figure 70.

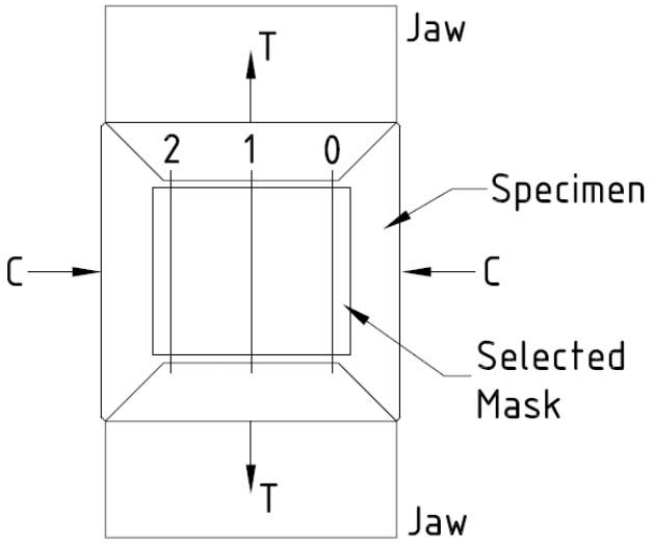

Figure 70 - Sample in tension jaws, showing extended grip on specimen face and Aramis sections

The deformation along section lines 0, 1 and 2 was calculated from the ARAMIS data and are given as Figures 71, 72 and 73. For this study, a local deformation exceeding 10μm (0.01mm) is considered to be a crack. Thus, in Figures 71, 72 and 73, a jump in deformation greater 0.01mm indicates a crack. The corresponding vertical position indicates the position on the sample within the defined mask.

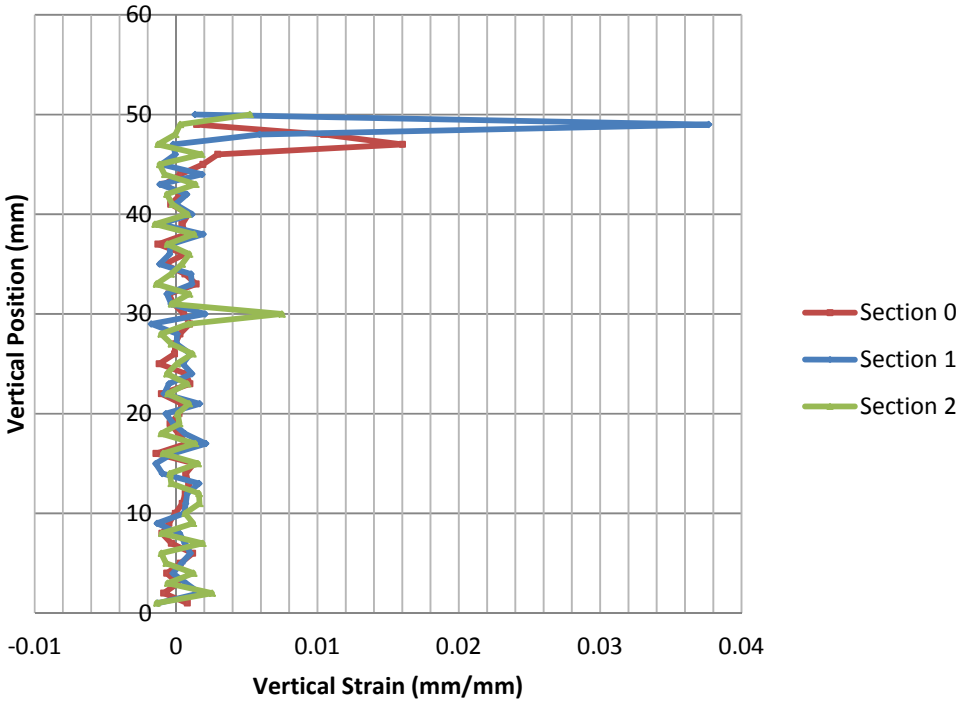

Figure 71 - Vertical strain vs. vertical position, 0.1% average vertical strain

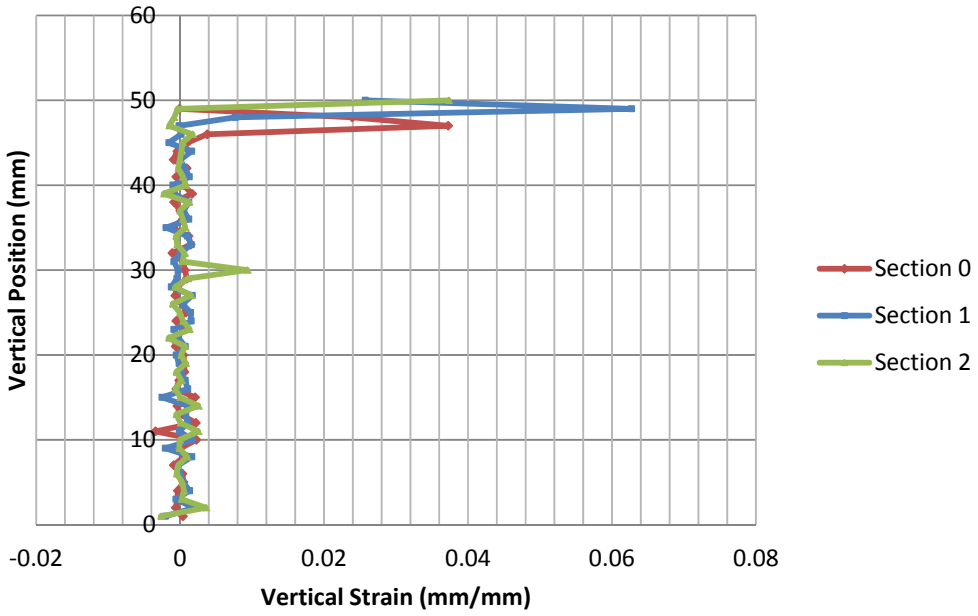

Figure 72 - Vertical strain vs. vertical position, 0.2% average vertical strain

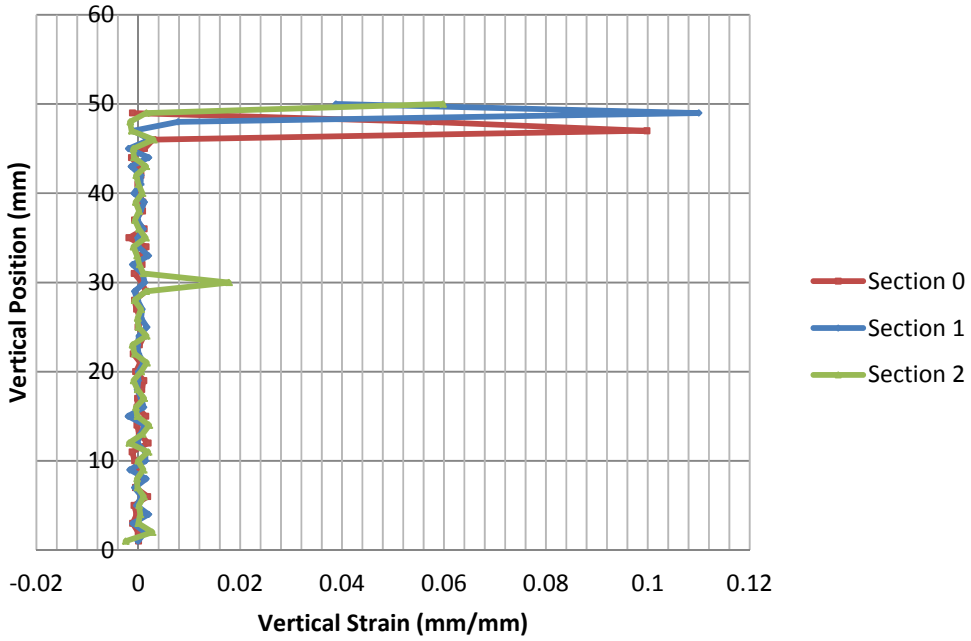

Figure 73 - Vertical strain vs. vertical position, 0.3% average vertical strain

Inspection of the deformations at each of the respective total strains clearly shows where the cracks form, how they enlarge and their widths. If an average is taken of the cracks for each respective strain, the number of cracks for each respective strain can be counted, Figure 74. The result is then that for 0.1%, 1 crack occurs, for 0.2%, 1 crack occurs and for 0.2%, 1.5 cracks occur.

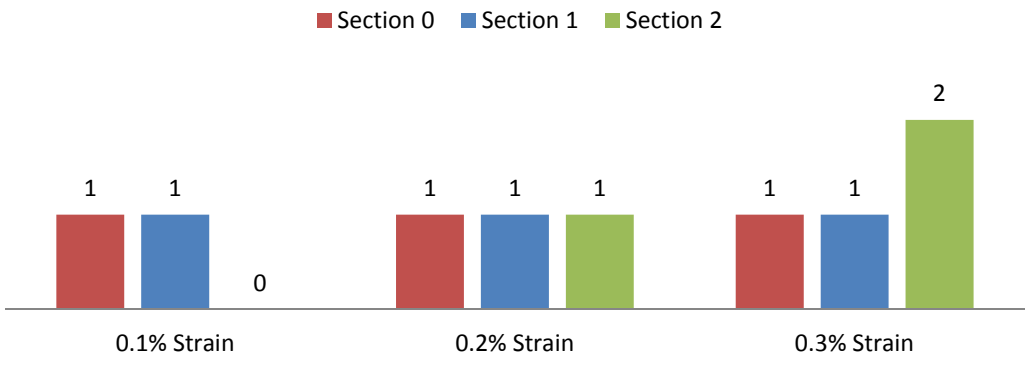

Figure 74 - Histogram showing number of cracks (n_c) at respective sections

5.2.2.3.1. Crack width

The peak tensile stress of 1.41MPa occurred at a corresponding total average strain of 0.00303. This stress peak occurred at 125s, but it was not the maximum strain point. The maximum strain was calculated to be 0.0033 at 126s, Figure 68. The fracture of the specimen however, happened at the point of contra flexure, the turning point where the stress resistance of the sample started to decrease. Thus, at the peak resistance of the sample, the crack width corresponds to the width that can be measured on Figure 73. It can be seen on Figures 71-73 that the crack starts in the top-middle of the specimen and propagates outward, the rightward crack growing faster than the leftward. Deformations for sections 0, 1 and 2 are: 0.1mm, 0.105mm and 0.06mm.

5.2.2.3.2. Crack Position

It is noted that all the cracks in Figures 71, 72 and 73 occur at the top of the section. It is important to realise that this is only one test result and thus only one fracture. The discussion above only shows the crack growth in time, the position of an existing crack remains the same. During testing it was found that specimens predominantly break at the top edge, but there were specimens that cracked and fractured at the bottom edge. The cause was investigated as possibly being the order in which the edges were glued to the jaws, but this seemed to have no effect as the “wet” time of the epoxy was long enough to be able to apply the epoxy on both edges without the epoxy hardening. See section 6 for validity of the ARAMIS crack measurement at the hand of physical crack observations.

5.3. Stress Field Uniformity

At the hand of the discussion on cracking (section 5.2.2.3) and crack position (section 5.2.2.3.2), the reason for the crack position is greatly determined by the stress field uniformity within the sample. As a result of the tension jaws, which are glued onto and over the specimen edges, there is no longer a uniform stress distribution. This non-uniformity causes stress concentrations around the jaw-edges (especially at the specimen corners where the jaw edge is at 45 degrees). A possible solution to this effect is given in section 7.

5.3.1. Tension-Tension

5.3.1.1. Uniaxial Tension

Uniaxial results were obtained from two sources. The first is the standard dumbbell tensile test and the second, uniaxial tests performed in the biaxial setup. Figure 75 shows the tension results for 4 standard dumbbell uniaxial tensile tests, performed on SHCC at age 28 days.

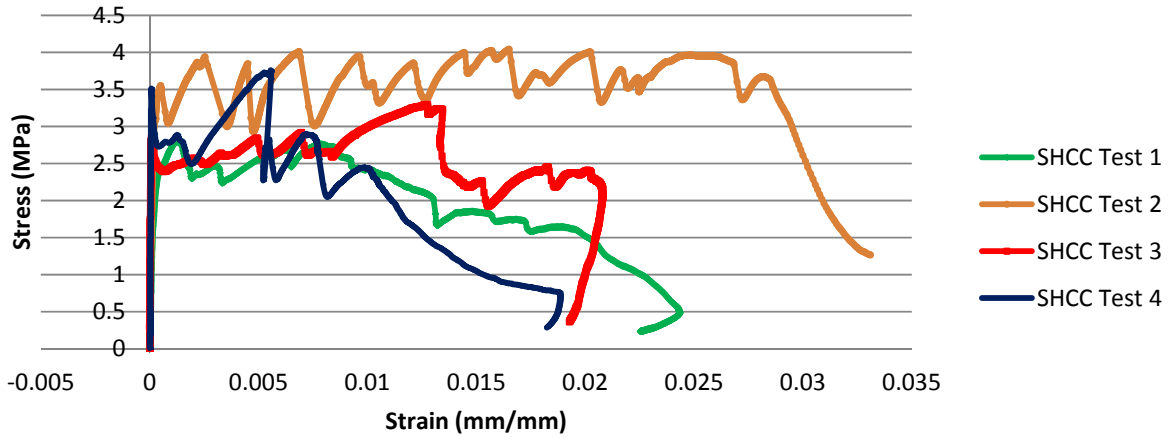

Figure 75 - Uniaxial tension result for a standard dumbbell test on SHCC

Figure 75 shows an increase in resistance, followed by a subsequent change in slope of the curves, to an ultimate resistance. This is a clear indication of strain hardening in uniaxial tension. Figure 76 shows the uniaxial results for SHCC in the biaxial setup.

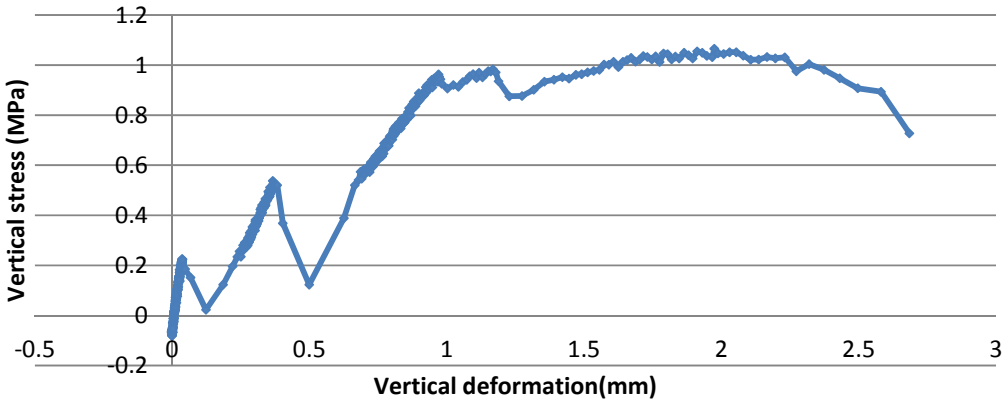

Figure 76 - Vertical displacement vs. vertical stress for uniaxial tension (Point 10, Figure 3)

Figure 76 shows definite drops in resistance where after increases in resistance occurred at different slopes, indicating that hardening does occur in the uniaxial tension testing in the biaxial setup. If Figure 75 is compared to Figure 76, the vertical stress measured for the test specimens used in this study differ as a result of the different cross section. The biaxial test specimens have a much greater cross sectional area than the standard dumbbell test specimens, the fibre orientation is also an important factor, see section 3.5.2. It can also be seen that the test starts with negative tension; this is because a 1kN compressive preload was applied to the specimen in order to spread the epoxy resin evenly across the bonding surfaces.

5.3.1.2. Biaxial Tension

In order to investigate the mechanical behaviour of SHCC in biaxial tension, the load-deformation relationship must be known. Figure 77 shows vertical tensile stress vs. vertical displacement measured by the vertical actuator. A plateau in resistance is reached at about 0.4MPa (0.15mm displacement) and is followed by a second rise at a different slope up to a point of 1.26MPa, indicating strain hardening.

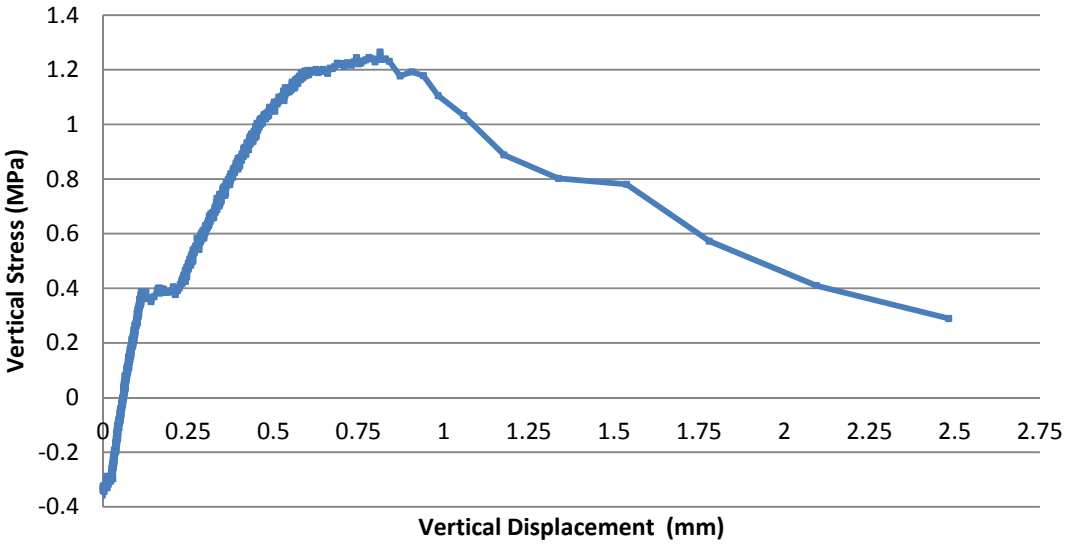

Figure 77 - Vertical displacement vs. vertical stress (Point 12, Figure 3)

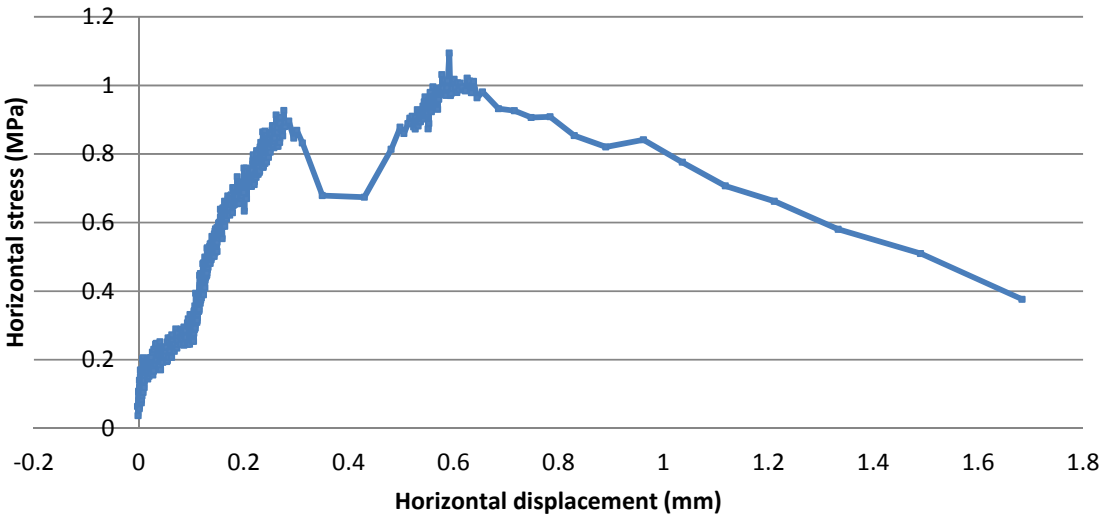

Figure 78 - Horizontal displacement vs. horizontal stress (Point 12, Figure 3)

Figure 78 shows the horizontal actuator data for stress vs. displacement. There is a definite drop in resistance at about 0.2mm displacement, indicating crack formation. Fibres bridge the crack and so allows for increased resistance after the initial weakening, followed by a second peak of 1.1MPa. This indicates that strain hardening does occur in biaxial tension.

5.3.1.3. Stress

The biaxial failure envelope for the tension-tension zone is given in Figure 79. The strength values of the tests performed in the biaxial setup are much lower than the uniaxial dumbbell test results. This is not simply the effect of only the specimen cross sectional area and the fibre orientation, but also as a result of the non-uniform stress distribution caused by the glued connection with varied shape along the edge (cut away at 45 degrees at the ends).

Figure 79 shows how the results indicate that the Rankine failure limit function (Figure 34) is not followed, but a more curved distribution is obtained, rather than the straight Rankine limit function. The maximum biaxial strength occurs at the ratio of 1:0.577, point 12 on Figure 3.

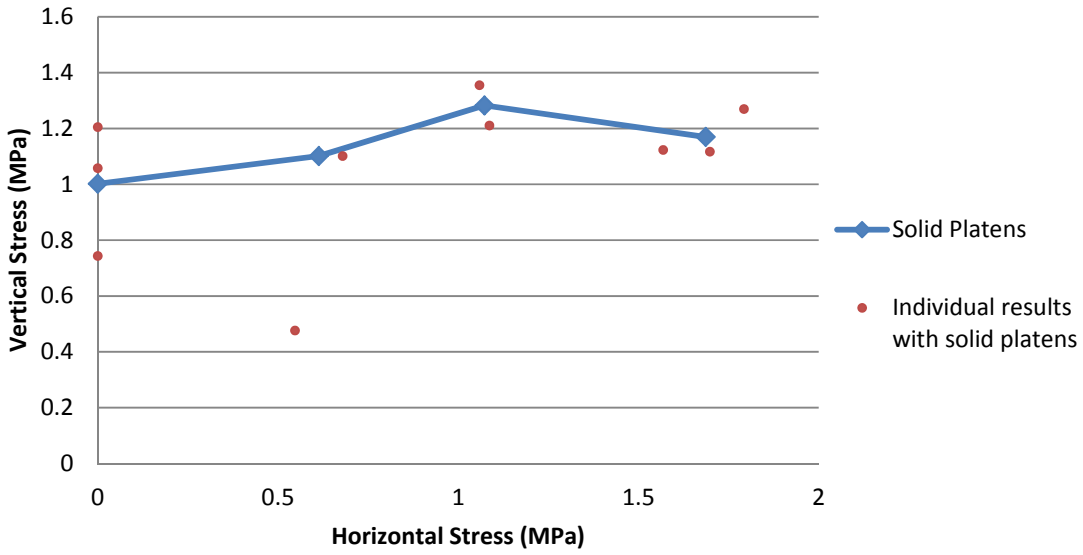

Figure 79 - Biaxial tension failure envelope

The result for the second point on the failure envelope has been adjusted to exclude the statistical outlier that might have occurred as a result of a weakness in the sample or the epoxy to specimen interface (lowest red dot) - the epoxy resin failed in the third test.

5.3.1.4. Strain

Unfortunately it has to be reported that no strain information can be shown for the tension-tension tests performed in the biaxial setup as technical difficulties with the ARAMIS measuring system lens calibration prohibited the capturing of any useful results in the compression-compression zone at the time of testing.

5.3.1.5. Cracking

A thorough analysis of cracks and width is not possible; however, multiple cracking of the SHCC specimens is discussed in chapter 6. The validity of crack patterns and visual observations cannot be discussed for the tension-tension quadrant.

5.4. Proposed Biaxial Failure Envelope for SHCC

Figure 80 gives the proposed biaxial failure envelope for SHCC. The results of the tests are plotted as the red dots and the average of the results give the blue failure envelope. The results at the 13 load ratios (represented by points 1 to 13 on Figure 3) are plotted and mirrored about the 45degree line, to give the full 360degree failure envelope.

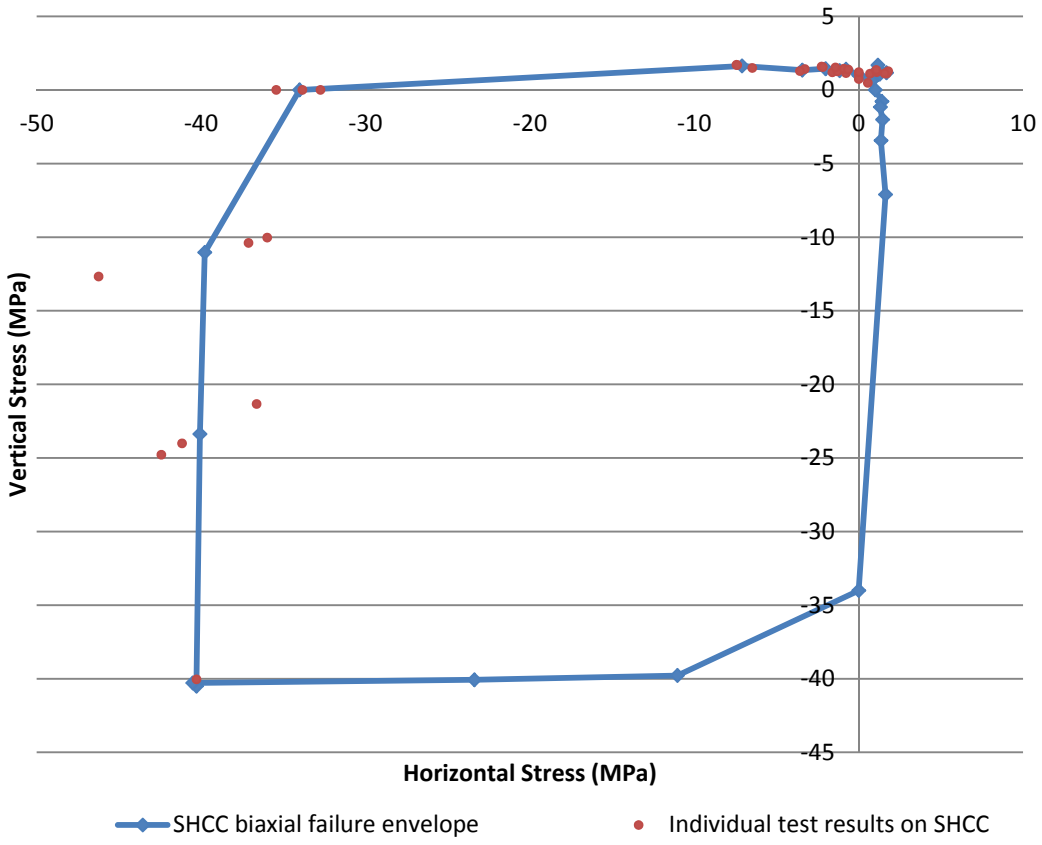

Figure 80 - Biaxial failure obtained by physical tests on SHCC in biaxial setup

It has to be reported that only one test result was possible for the 1:1 test ratio on Figure 80. With reference to section 3.3, the test ended with the loading platens colliding after the specimen fractured. The SHCC failed suddenly and as the actuator (force-controlled) seeks resistance from the specimen; the limitation on allowable displacement was exceeded. No further tests were performed as damage to the actuator could occur, prohibiting further testing. It is recommended that a different solution be found in order to allow more test results in the zone where the load ratio is close to 1:1. See Appendix E for a complete set of results.

6. Failure Mechanisms

Much information about the characteristics of SHCC is well-known in uniaxial compression and tension. This thesis expands that knowledge about the characteristics of SHCC to include the characteristics and failure mechanisms in biaxial states of stress. The failure mechanisms of SHCC under biaxial loading are important as the manner in which the material fractures under load is investigated.

Cracking is investigated and in particular, the presence of multiple cracking because one of the characteristics of SHCC is that it is designed to have multiple cracking. Crack patterns and the propagation thereof tell us where cracks form as well as how boundary conditions and load application affect the fracture mechanics of a specimen. Fibre orientation also affects the fracture mechanics of a specimen; the manner in which the fibres bridge cracks (to form stable cracks) and then ultimately fail, tell us how crack growth occurs.

6.1.Compression

Compression does not cause multiple cracking in SHCC under uniaxial load, but nevertheless causes a significantly higher ductility than in normal concrete. It is investigated whether this remains the case in biaxial compression.

6.1.1. Uniaxial compression

Uniaxial compression tests yielded specimens which failed in shear. This shear failure occurred in all ratios from uniaxial to biaxial. Figure 81 shows uniaxial failure and Figures 82 and 83 show biaxial compression failure.

Figure 81 - Uniaxial compression failure (Point 4, Figure 3)

This shear-type failure agrees with Torrenti & Djebri (1995), who found that for metal fibre concretes in biaxial compression that failure occurred by the formation of a shear band inclined 20-45 degrees with respect to the direction of greatest loading. Hussein & Marzouk (2000) reported a similar result for high strength concrete, stating that cracks formed at an angle of 20-30 degrees to the direction of applied load and referred to the failure as a fault-type failure.

6.1.2. Biaxial compression

There is a different failure mechanism found in compression tests on specimens with 2D fibre orientation (thin-cast) and compression tests on specimens with 3D fibre orientation (larger cast and cut). Figure 82 shows the failure mechanism of a thin-cast specimen with 2D fibre orientation. The front view of the specimen can be seen on the left, and the side view (showing splitting) can be seen on the right.

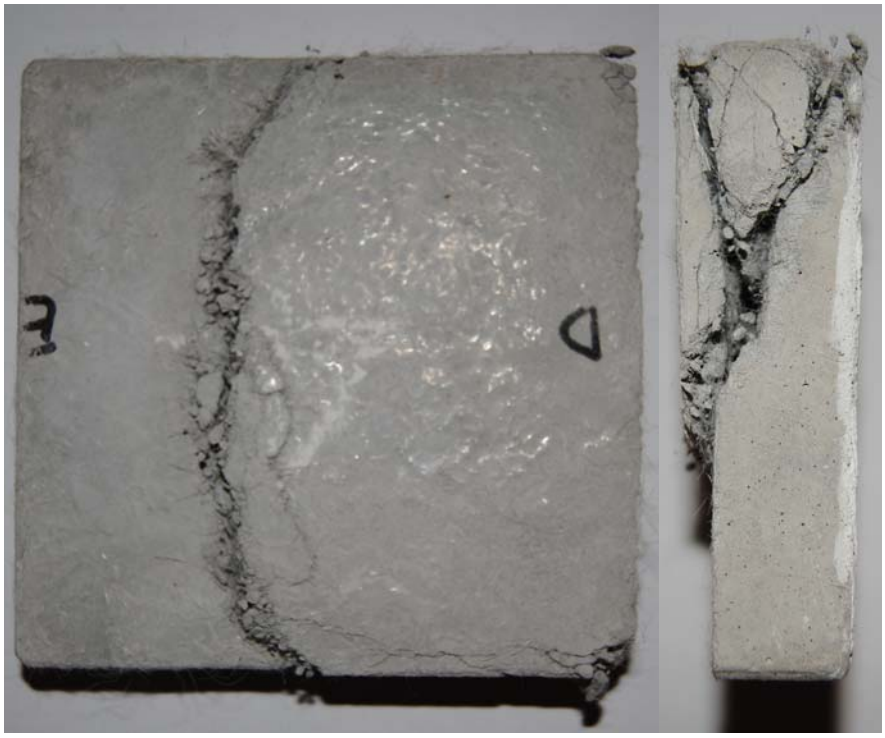

Figure 82 - Biaxial compression failure of a thin-cast SHCC specimen (Point 4, Figure 3)

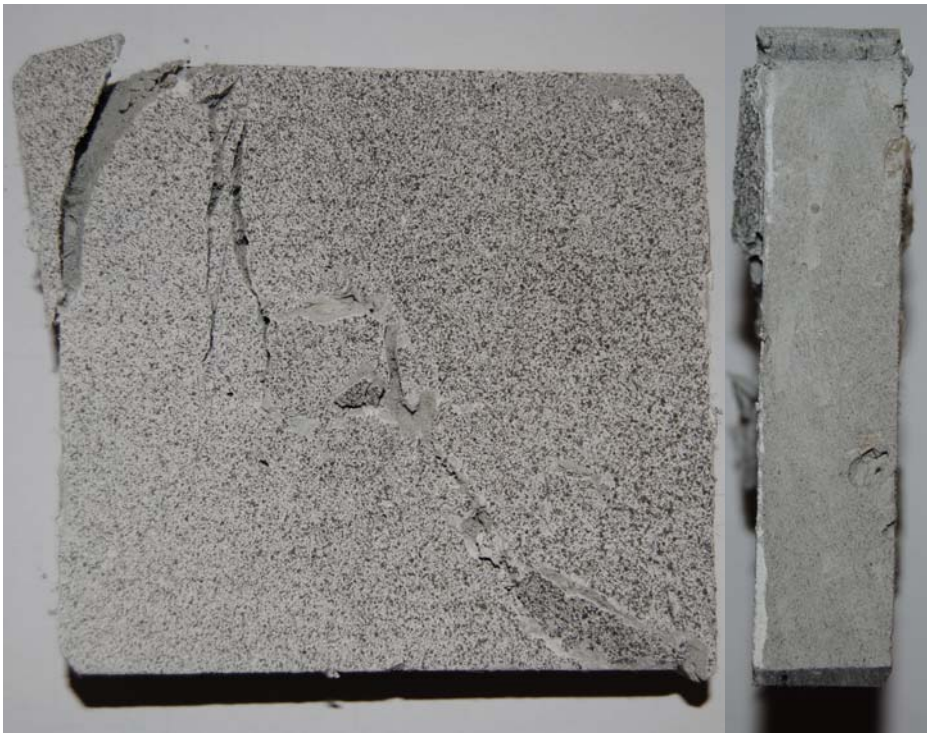

Figure 83 - Biaxial failure of a larger-cast and cut SHCC specimen (Point 3, Figure 3)

Figure 83 shows the biaxial failure of a larger-cast and cut SHCC specimen with 3D fibre orientation. The front view of the sample can be seen on the left and the side view on the right. Comparison of Figures 82 and 83 show that there is a marked difference in the failure mechanism.

Failure occurs in Figure 82 by a splitting-type fracture, discussed in section 2.6.1. The side view shows how the specimen split open in a Y-shape and a wedge of material opened up the Y until failure. This split occurred due to the low amount of fibres oriented in the out-of-plane direction.

The failure mode in Figure 83 the sample becomes crushed in the plane of loading. There is no splitting of the specimen due to the fibres being 3D orientated and thus preventing this splitting. Shear fracture occurs as a combination of shear modes I and II.

6.2. Compression – Tension

Tests in the compression-tension zone were performed with the vertical axis applying tension and the horizontal axis applying compression, shown in Figures 84 and 85. Generally, failure occurred in a single crack at either the top edge of the specimen or the bottom edge, close to the edge of the tension jaws.

The reason for cracks forming at this position could be as a result of the significant stress concentration at the tension-jaw edge. The shape of the jaw causes a stress distribution which is significantly higher at the corners than in the centre region of the specimen, thus a uniform stress distribution is not achieved under tensile load with the use of the jaws.

A factor which could also possibly play a role is the difference in Poisson ratio between the part of the specimen glued to the clamps and the free part of the specimen. The part of the SHCC material within the clamps cannot contract under tension as much or as fast as the free part and so the interface between these two zones is a line of weakness, and hence cracks form there.

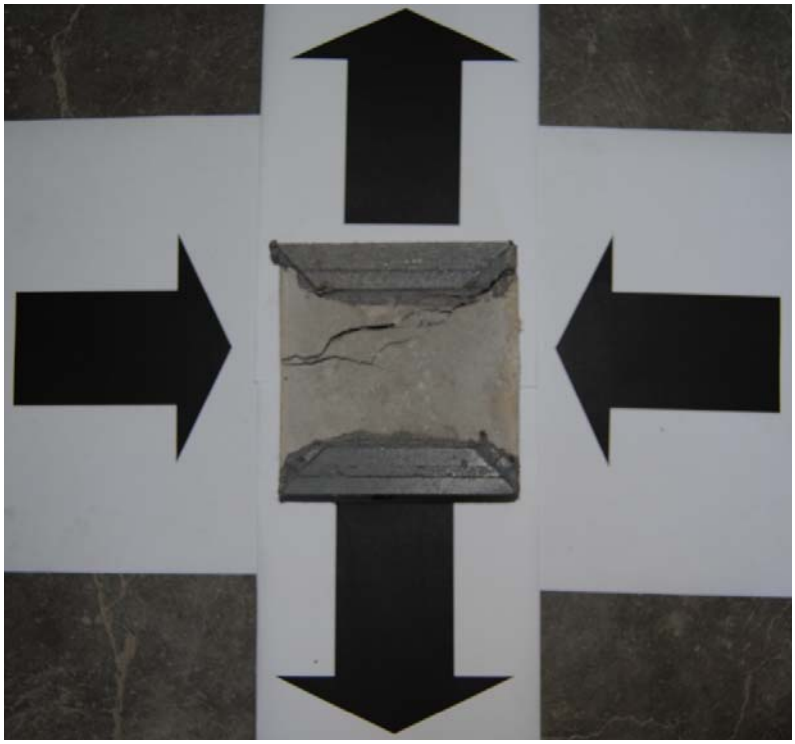

Figure 84 - Biaxial compression-tension failure (Point 6, Figure 3)

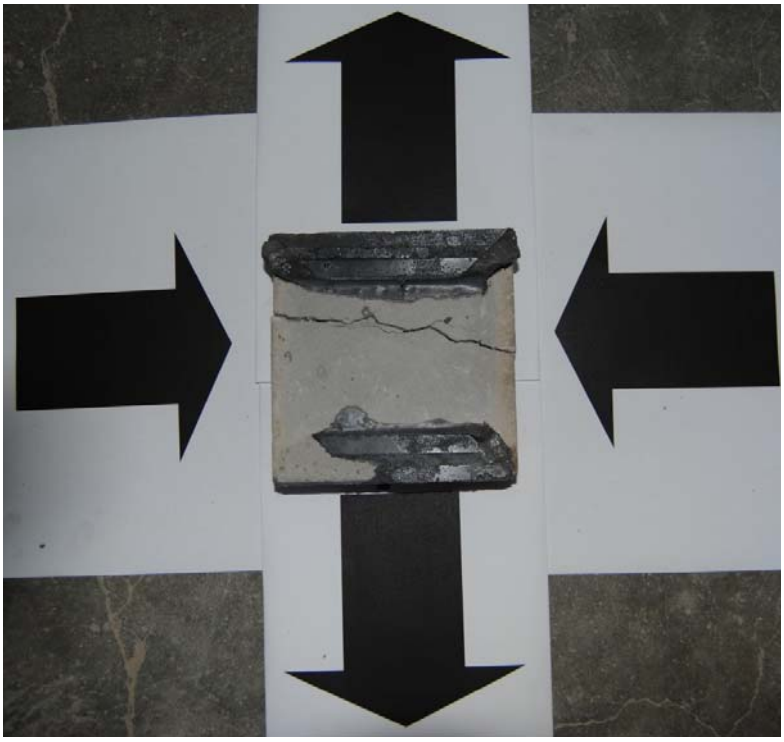

Figure 85 - Biaxial compression-tension failure (Point 9, Figure 3)

In cases where the tension force was dominant, say point 9 on Figure 3, the failure mechanism changed from a localised crack close to the jaw edge to cracks and fracture more towards the centre of the specimen. This fracture would imply a more uniform stress distribution was achieved for that specific test, Figure 85.

From Figures 84 one must conclude that the tension clamping jaws have a major influence on the failure behaviour and causes an undesired failure mechanism. On Figure 85, the jaws seemed to have no influence, cracking and fracture occurred away from the jaws, which would be the ideal failure mode.

It must be reported that not all the specimens performed in the ideal manner in Figure 85, and on Figure 84 it can be seen that the cracks start at the corner, on the jaw to specimen interface. Figure 86 illustrates the worst case, the failure mechanism caused by the non-uniform stress distribution as a result of the jaws.

Figure 86 - Failure mechanism caused by tension jaws in biaxial compression-tension (Point 8, Figure3)

6.3. Tension – Tension

Tests were performed in the tension-tension zone where the vertical axis load was kept constant and the horizontal axis load was increased from zero to match the vertical load. Specimen fracture did not occur in the same manner each time and some samples failed in a very similar way to compression-tension failure, Figure 87.

6.3.1. Uniaxial Tension

Figure 87 shows a test specimen indicating the uniaxial tension failure mechanisms.

Figure 87 - Uniaxial tension failure (Point 10, Figure 3)

6.3.2. Biaxial Tension

As can be seen from Figure 88, the crack pattern is dictated by the non-uniform stress distribution effect caused by the jaws. Cracks start in the corners and propagate through the specimen with some secondary cracks, in both directions, occurring at loading ratios that are close to the same magnitude.

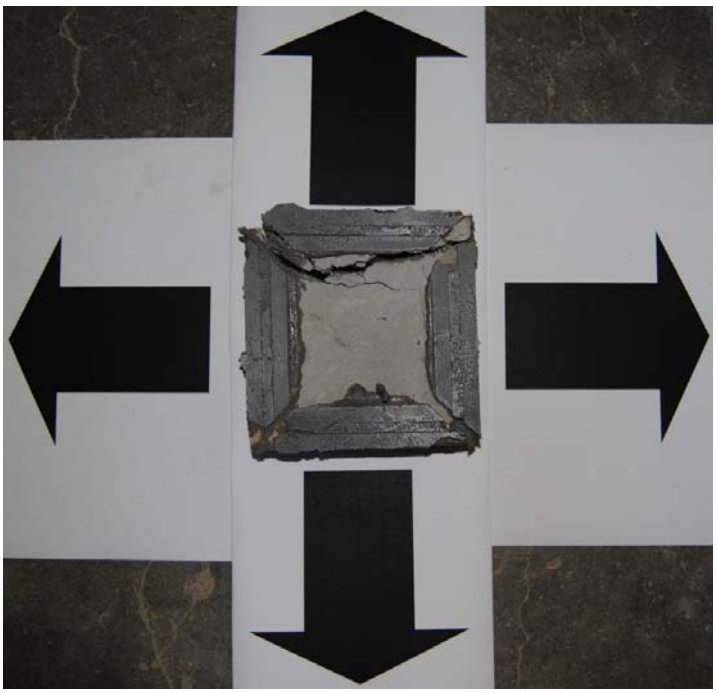

Figure 88 - Biaxial tension-tension failure (Point 11, Figure 3)

Figures 89 and 90 show a more expected crack pattern, where secondary cracks formed as well. The cracks formed independent from the mechanism caused by the jaws and cracks even propagated through the epoxy resin.

In Figure 90, cracks occurred around both the top and right jaw, with a large diagonal crack causing failure. The expected crack pattern for tension-tension testing is diagonally across the specimen, without the influence of the mechanism caused by the jaws.

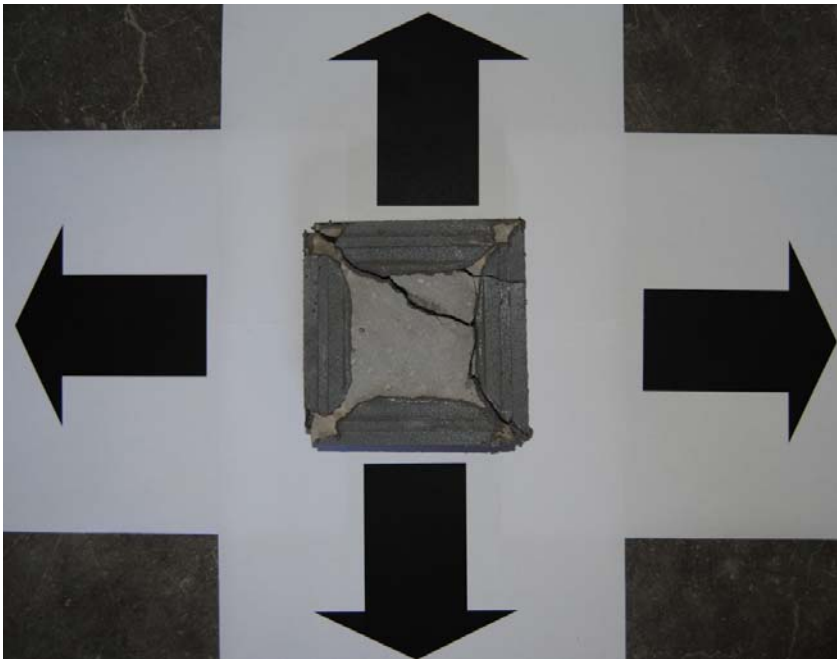

Figure 89 - Biaxial tension-tension failure (Point 12, Figure 3)

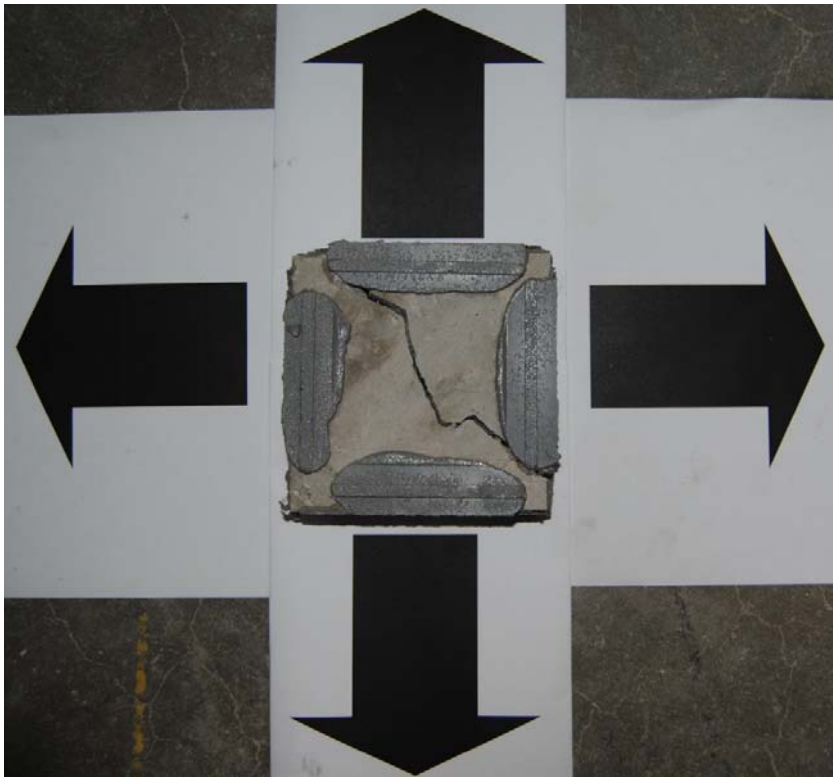

Figure 90 - Expected biaxial tension-tension failure (Point 12, Figure 3)

6.4. Multiple Cracking

It is of great importance to know whether each of the specimen failures occurred as one single crack, or if more cracks arose/developed.

Close-up photographs of the loading cases shown in Figures 81-90 were taken to investigate the cracking patterns in all the loading regimes. See Appendix F for multiple cracking results of all test specimens.

6.4.1. Compression-compression

A specimen which has failed under biaxial compression loading is shown in Figure 91, which is the back side of the specimen shown in Figure 83.

Figure 91 - Multiple crack formation on specimen that has failed in biaxial compression (Point 3, Figure 3)

The left image is taken of the top left corner of the specimen and the right image is of the bottom right corner of the specimen. Multiply cracks can be seen clearly, as indicated by the white arrows.

6.4.2. Compression-Tension

A close up view of a specimen that failed under vertical tension and horizontal compression (Point 5, Figure 3) is shown in Figure 92.

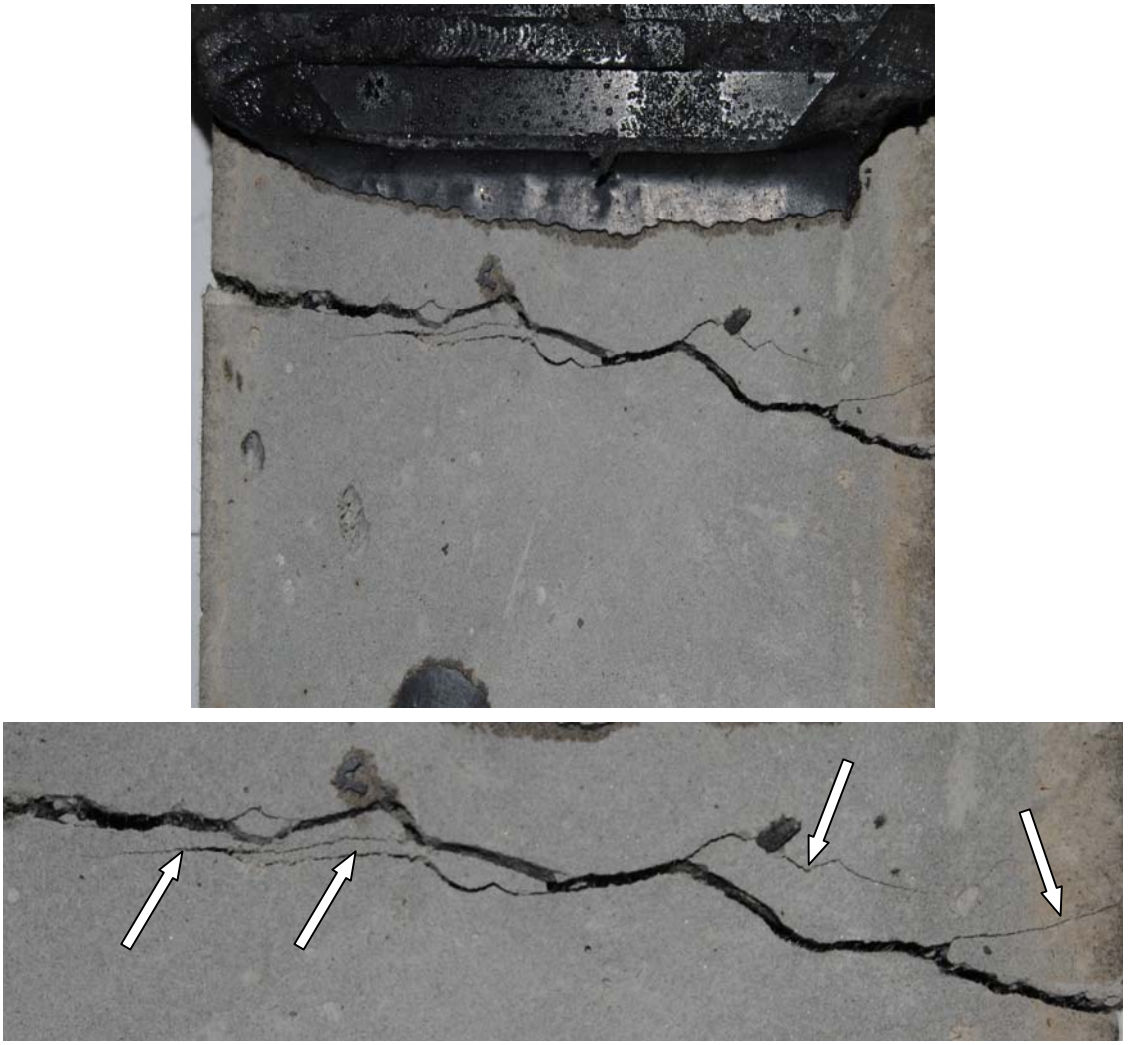

Figure 92 - Multiple crack formation on specimen that has failed in compression-tension (Point 5, Figure 3)

Inspection of Figure 92 indicates that in biaxial compression-tension, multiple cracks occurred on the specimen. The white arrows on the bottom image (enlargement of the cracks on top image) show that there are four secondary cracks which formed on the specimen, around the single large crack. it should be noted that saturated multiple cracking did not occur on this specimen, the fine cracks mostly occurred close to the dominant large cracks.

6.4.3. Tension-Tension

A close up view of a specimen (Point 12, Figure3) that failed under biaxial tension is shown in Figure 93.

Figure 93 - Multiple crack formation on a specimen that has failed in biaxial tension (Point 12, Figure 3)

As can be seen by the number of white arrows, numerous cracks formed as secondary cracks. Saturated multiple cracking did not occur on this specimen but rather fine cracks close to the dominant large cracks. The failure occurred as a result of the large diagonal crack and the large vertical crack on the right.

See Appendix F for results and comments on multiple cracking for the entire set of SHCC specimens tested in the biaxial setup.

6.5. Ductility under Biaxial Load

Whereas much is known about the ductility of SHCC under uniaxial load, in standard tests, not much is known about the ductility of SHCC under biaxial load. It is well known that in uniaxial tensile tests on dumbbell specimens, saturated multiple cracking occurs. SHCC thus possesses much ductility as it deforms significantly (elongates) at a reduced resistance after initial cracking.

In order to compare ductility of SHCC under uniaxial tension, Figure 94 shows a comparison of a standard test result at 28 days and a uniaxial test, performed in the biaxial test setup at 56days. It should be noted that the curing strategies for all specimens (standard-and biaxial tests) were the same.

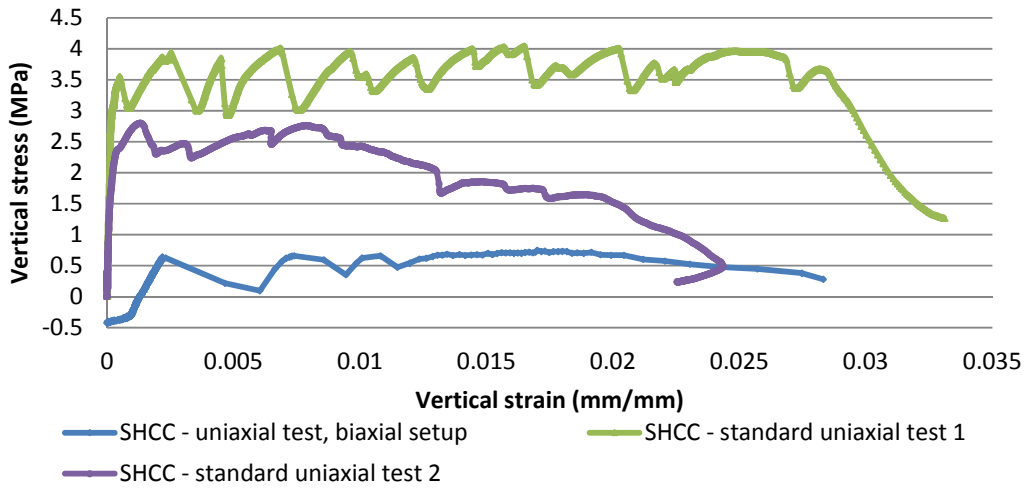

Figure 94 – SHCC stress-strain behaviour comparison of standard uniaxial tension tests and a uniaxial tension test performed in biaxial setup

In Figure 94, the most noticeable difference in stress-strain relationship is that the biaxial setup test (blue curve) yielded a much lower ultimate tensile strength. The ultimate strains reached by the respective tests are in the same order of magnitude, but at significantly different resistances. If the fracture energy is considered (see section 4.3.1.2, the biaxial setup test has far less energy than the standard tests, and thus has a lower ductility, which agrees with what is noticed in crack patterns. From the discussions on multiple cracking in the various loading quadrants, section 6.4 and Appendix F, it is concluded that multiple cracking does occur in SHCC under biaxial load, but it is not saturated multiple cracking. All the tension-tested specimens thus show fewer cracks than the standard dumbbell tests, which would be an indication that the SHCC biaxial test specimens are less ductile than the standard specimens.

7. Experimental Setup Improvements

7.1. Failure mechanism

The solution to the physical undesired failure mechanism is more complicated than in the computational model. It would require a thorough understanding of the pros and cons of casting and cutting samples and the difficulties involved in creating a sample of a different, more complex shape.

In this study, the larger cast member idea was preferred and thus a solution using cut out samples is proposed. Figure 95 shows the proposed sample in the clamps; compare to figure 23, for the compression-tension scenario. Note the curves at the corners of the sample; which will prevent cracks propagating from a corner. The unknown parameters H1, H2 and R need to be investigated in future studies.

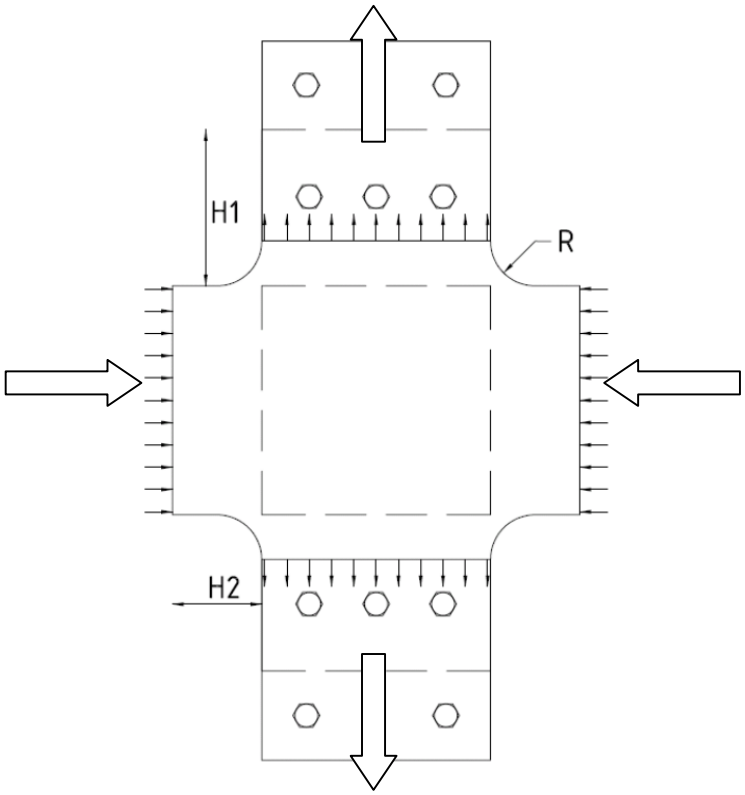

Figure 95 - Proposed improvements to specimen shape that would improve load distribution

Note, the holes on the specimen are for pins, so that the specimen is no longer glued in but three pins connect the specimen to the loading platen. This is in order to avoid the inconsistency of glue application, setting and curing. The holes should of course be far enough from the measuring space in order to avoid influencing the uniform stress field. This solution can be investigated in future studies.

7.2. Load Control

The load control implemented in the biaxial test setup consisted of two Instron hydraulic actuators working in parallel. It is proposed that for future applications and biaxial tests, a different method of control be considered where the actuators are dependent on one another.

This proposed system should measure the resistance in one direction (which gives the specimen stiffness in that direction) and apply a load in the perpendicular direction proportional to this resistance. This would mean that the loading will be truly proportional and thus the failure points on the biaxial failure envelope will coincide with the load ratios (Figure 3).

8. Conclusions

8.1. General

Testing concrete biaxially holds many challenges such as uniformity in the load distribution, frictional effects, fibre orientation effects, ensuring accurate boundary conditions and load control, to name but a few. It is however possible to successfully test concrete biaxially in all compression and tension regimes, and to get realistic results.

8.2. Friction

Friction plays a very important role in load transfer; it cannot be ignored nor completely circumvented. As discussed, section 3.2.1, loads are applied to the specimen by means of loading platens. The platens must therefore apply a uniform load onto the specimens, in doing so, inherently, friction is generated.

8.2.1. Brush-type platens

Brush-type platens were investigated in compression testing, section 3.6. Apart from very expensive manufacturing, the brush platens did not perform well. In compression, the platen bristles penetrated the concrete matrix to such an extent that it caused a failure mechanism.

The platens also could not withstand a high compressive load. If the bristles are too short, the desired movement which the bristles should allow does not occur. If the bristles are too long, they tend to buckle under compression. A length where both of these cases would be avoided, to an extent, was chosen. Due to the failure mechanism caused by the brush bristle penetration (section 3.6), the concrete could become wedged in between the bristles and so cause permanent deformation to the bristles, rendering them useless.

From biaxial compression results, it can be seen that the lowest biaxial strength values are obtained for the brush-type platens, section 5.2.1.1, Figure 64..

8.2.2. Solid platens

Solid platens without any surface treatment were investigated. It was found that friction played a major role and in combination with the identified failure mechanism caused by casting samples, wedging

occurred where the surface of the specimen in contact with the platens remained completely intact, even after failure, section 3.6, Figure 31.

It was also discovered that the solid loading platen had to be wider than the specimen because local crushing at the contact surface caused a block the width of the platen to remain in contact with the platen and become wedged into the sample, section 3.6, Figure 31.

Higher biaxial strength values were obtained in biaxial testing than brush-type platens, section 5.2.1.1, Figure 64.

8.2.3. Solid platens with Teflon sliding layers

Solid platens, wider than the specimen, in combination with Teflon sliding layers proved very successful. Samples could fracture without interference, often through the entire sample, tearing the Teflon. This is proof that the loading platen surface in combination with the Teflon does not cause a failure mechanism but allows the specimen to fracture as a result of loading only.

The combination of solid platens with Teflon sliding layers yielded far higher results than either of the brush-type or solid platens without Teflon, concluding that the combination is effective in load transfer without detrimental effects of friction, section 5.2.1.1, Figure 64.

8.3. Fibre Orientation

Biaxial compression tests were performed on cast samples and on cut samples. Test results and specimen failure indicated that fibre orientation plays a major role in biaxial strength as well as the failure mechanism under biaxial load, sections 2.6.1 and 3.5.2.

The tests performed on specimens with a 3D fibre orientation yielded biaxial strengths about 15% higher than tests performed on specimens with a 2D fibre orientation, section 5.2.1.1, Figure 64. This result is a combination of the Teflon sliding layers and the fibre orientation and tests without the Teflon sliding layers will have to be performed to isolate the effects of only the fibre orientation.

8.4. Strain Hardening

For the case of compression-tension, the stress-strain curves were studied and the load-deformation curves were studied for the tension-tension case.

8.4.1. Compression-tension

In Figure 68, section 5.2.2.2, there is a definite change in gradient of the stress-strain curve accompanying a continued increase in resistance and strain. This is clear proof of strain hardening in the compression-tension state. It has to be concluded that the SHCC does show strain hardening in a biaxial compression-tension state.

8.4.2. Tension-tension

Strain could not be studied for uniaxial or biaxial tension. Increased resistance at a different slope was found to occur in SHCC tested under uniaxial conditions in the biaxial setup, Figure 74, section 5.3.1.1, and biaxial conditions, Figures 77 and 78, section 5.3.1.2. This increased resistance at a different slope is proof of strain hardening in the tensile regime.

8.5. Multiple Cracking

Close-up photographs of the loading cases shown in Figures 91-93 were taken to investigate the cracking patterns in all the loading regimes. All specimens were scrutinized and the results are given in Appendix F. Numerous multiple cracks were counted for all loading regimes, uniaxial and biaxial. It is concluded that multiple cracking does occur in SHCC, for the specific specimen size, under biaxial conditions but it must be stated that this is not saturated multiple cracking. The shape of the specimen definitely plays a part in this absence of saturated cracking. The dumbbell specimens are designed to have localised cracking in the narrower “neck” section where the saturated cracking occurs. The biaxial test specimens are not designed to have localised cracks and thus the failure is dominated by a single large crack which is surrounded by multiple finer cracks.

8.6. Ductility

The difference in ductility of SHCC in standard uniaxial tension tests and uniaxial tests performed on specimens in the biaxial setup is discussed in section 6.5. It can be concluded that saturated multiple cracking does not occur and that the uniaxial response curve of a biaxial setup test has a lower fracture energy than a standard test, thus SHCC is less ductile in the biaxial setup. The lower ductility in the biaxial setup can also be attributed to the difference in cross sectional area in the test specimens (as discussed in 8.5).

8.7.Biaxial failure envelope for SHCC

The proposed biaxial failure envelope for SHCC is given as Figure 80, section 5.4. It can be concluded that the confinement effect is proved to occur in SHCC under biaxial loading in all three quadrants; compression-compression, compression-tension and tension-tension.

References

Addis, B. "Fundamentals of Concrete," Cement and Concrete Institute, ISBN 0-9584085-3-X, 2007.

Bažant, Z.P., Oh, B.H., "Crack band theory for fracture of concrete," Materials and Structures, 16(93):155–177, 1983.

Bentur, A., Mindess, S. "Fibre Reinforced Cementitious Composites," 2nd Edition, Modern Concrete Technology 15, Taylor and Francis, ISBN 978-0-415-25048-1, 2007.

BS EN 1992-1-1:2004, Incorporating corrigendum January 2008, Eurocode 2: Design of concrete strutctures – Part 1-1: General rules and rules for buildings, ICS 91.010.30; 91.080.40, ISBN 978 0 580 61759 1.

Calixto, J.M.F., "Microcracking of High Performance Concrete Subjected to Biaxial Tension – Compression Stresses," Materials Research, Vol. 5, No. 3, 295-299, 2002.

De Koker, D., van Zijl, G.P.A.G., "Extrusion of Engineered Cement-Based Composite Material," 6th RILEM Symposium on Fiber-Reinforced Concretes (FRC) – BEFIB 2004 20-22 September 2004, Varenna, Italy, pp1301-1310.

Diana 2002. Diana Finite Element Analysis User's Manual, release 8.1, TNO Building, The Netherlands.

Ehm, C., Schneider, U. "The High Temperature Behaviour of Concrete Under Biaxial Conditions," Cement and Concrete Research. Vol. 15, pp. 27-34, 1985.

Elser, M., Tschegg, E.K., Stanzl-Tschegg, S.E., "Biaxial Fracture Tests on Concrete – Development and Experience," Cement & Concrete Composites 17 (1995) 57-75, Elsevier, 1994.

Elser, M., Tschegg, E.K., Stanzl-Tschegg, S.E., "Fracture Behaviour of Polypropolene-Fibre-Reinforced Concrete under Biaxial Loading: An Experimental Investigation," Composites Science and Technology 56 (1996) 933-945, Elsevier, 1996.

Gao Song, "Matrix Manipulation to Study ECC Behaviour," MScEng-thesis, University of Stellenbosch, 2005.

Hannant, D.J., "Fibre cements and fibre concretes," Wiley, Chichester, UK, ISBN 0 471 99620 3, 1978.

Hu, X.D., Day R., Dux, P., "Biaxial Failure Model for Fibre Reinforced Concrete," DOI: 0.1061/(ASCE)0899-1561(2003)15:6(609), Journal of Materials in Civil Engineering, ASCE/November/December 2003/609, 2003.

Hussein, A., Marzouk, H. "Behaviour of High-Strength Concrete under Biaxial Stresses," American Concrete Institute Materials Journal, January-February 2000

Illston, J.M., Domone, P.L.J., "Construction Materials Their Nature and Behaviour," Third Edition, Spon Press, ISBN 0-419-25860-4, 2001.

Kölle, B., Phillips, D.V., Zhang, B., Bhatt P., Pearce, C.J. "Experimental Investigation of the Biaxial Properties of High Performance Steel Fibre Reinforced Concrete," 6th Rilem Symposium on Fibre-Reinforced Concretes (FRC), BEFIB 2004, Varenna, Italy, 2004.

Kuraray (2011). http://www.kuraray.co.jp/kii/english/ accessed on 5 September 2011.

Li, V.C., Mishra, D.K. and Wu, H., Matrix design for pseudo-strain-hardening fibre reinforced cementitious composites. *Materials and Structures*, 28, 586-595, 1995.

Li, V.C., Wang, S., Wu, C., "Tensile strain-hardening behaviour of Polyvinyl Alcohol Engineered Cementitious Composites (PVA-ECC)," ACI Materials Journal, Nov. - Dec. 2001, pp. 483-492, 2001.

Molapo, T.K., "The behaviour of Strain-hardening cement composites under biaxial compression," Master's degree thesis, Stellenbosch University, 2010.

Murugappan, K., Paramasivam, P., Tan, K. H., "Failure envelope for steel fiber concrete under biaxial compression," J. Mater. Civ. Eng, 5(4), 436-446, 1993.

Naaman, A.E., Reinhardt, H.W., "Proposed classification of HPFRC composites based on their tensile response," *Materials and Structures*, 39, pp. 547–555, 2006.

Rots, J.G., "Computational modelling of concrete fracture," Dissertation, Delft University of Technology, Delft, The Netherlands, 1988.

Selby, R. G., Vecchio, F. J., "Three-dimensional Constitutive Relations for Reinforced Concrete," Tech. Rep. 93-02, Univ. Toronto, dept. Civil Eng., Toronta, Canada, 1993.

Shah, S.P., Srnivasan, R., DeFord, D., "The Use of Extrusion Rheometry in the Development of Extruded Fiber-Reinforced Cement Composites," Concrete Science and Engineering, Vol. 1 No. 11, 1999.

Stander, H., “Interfacial bond properties for ECC overlay systems,” MScEng-thesis, University of Stellenbosch, 2007.

Swaddiwudhipong, S., Seow, P.E.C., “Modelling of Steel Fibre Reinforced Concrete Under Multi Axial Loads,” Cement & Concrete Research 36 (2006) 1354-1361, Elsevier, 2006.

Torrenti, J.M., Djebri, B., “Behaviour of Steel-Fibre-Reinforced Concretes Under Biaxial Compression Loads,” Cement & Concrete Composites 17 (1995) 261-266, Elsevier, 1995.

Traina, L.A., Mansour, S.A., Discussion on “Biaxial tests of plain and fibre concrete” by Yin, W.S., Su, E.C.M., Mansour, M.A., and Hsu, T.T.C., ACI Material Journal, 87(2), 179-180, 1990.

Van Mier, J.G.M. “Strain-softening of Concrete Under Multiaxial Loading Conditions,” Ph.D Dissertation, Eindhoven University of Technology, Netherlands, (Nov., 1984).

Van Zijl, G.P.A.G., “Computational modeling of SHCC,” Report ISI2009-20, Institute of Structural Engineering, Stellenbosch University, 2009.

Van Zijl, G.P.A.G., “Improved mechanical performance: Shear behaviour of strain hardening cement-based composites (SHCC),” *Cement and Concrete Research,* 37(8), pp. 1241-1247, 2007.

Van Zijl, G.P.A.G., Boshoff, W.P. “Mechanisms of creep in fibre-reinforced strain-hardening cement composites (SHCC),” 2008.

Van Zijl, G.P.A.G., Boshoff, W.P., “FRC in South Africa - application fields, new developments and outlook,” Proceedings of International Concrete Conference and Exhibition (ICCX 2008), Sun City, South Africa, February 2008, pp. 46-52, 2008.

Van Zijl, G.P.A.G., Stander, H., “SHCC repair overlays for RC: Interfacial bond characterization and modelling,” CDROM Proceedings International Conference on Concrete Repair, Rehabilitation and Retrofitting (ICCRRR 2008), University of Cape Town, South Africa, pp. 995-1003, 2009.

Yin, W.S., Su, E.C.M., Mansour, M.A., and Hsu, T.T.C., “Fiber-Reinforced Concrete Under Biaxial Compression,” Engineering Fracture Mechanics Vol. 35, No. 1/2/3, pp. 261-268, 1990.

Yin, W.S., Su, E.C.M., Mansour, M.A., Hsu, T.T.C., “Biaxial tests of plain and fibre concrete,” ACI Material Journal, 86(3), 236-243, 1989.

Appendix A – Eurocode Information

Table 3.1, BS EN 1992-1-1 2004

Strength classes for concrete														Analytical relation / Explanation
f_{ck} (MPa)	12	16	20	25	30	35	40	45	50	55	60	70	80	90	
$f_{ck,cube}$ (MPa)	15	20	25	30	37	45	50	55	60	67	75	85	95	105	2.8
f_{cm} (MPa)	20	24	28	33	38	43	48	53	58	63	68	78	88	98	$f_{cm} = f_{ck}+8$(MPa)
f_{ctm} (MPa)	1,6	1,9	2,2	2,6	2,9	3,2	3,5	3,8	4,1	4,2	4,4	4,6	4,8	5,0	$f_{ctm}=0,30\times f_{ck}^{(2/3)} \leq C50/60$ $f_{ctm}=2,12\ln(1+(f_{cm}/10))$ $> C50/60$
$f_{ctk,0,05}$ (MPa)	1,1	1,3	1,5	1,8	2,0	2,2	2,5	2,7	2,9	3,0	3,1	3,2	3,4	3,5	$f_{ctk,0,05} = 0,7\times f_{ctm}$ 5% fractile
$f_{ctk,0,95}$ (MPa)	2,0	2,5	2,9	3,3	3,8	4,2	4,6	4,9	5,3	5,5	5,7	6,0	6,3	6,6	$f_{ctk,0,95} = 1,3\times f_{ctm}$ 95% fractile
E_{cm} (GPa)	27	29	30	31	33	34	35	36	37	38	39	41	42	44	$E_{cm} = 22[(f_{cm})/10]^{0,3}$ (f_{cm} in MPa)
ε_{c1} (‰)	1,8	1,9	2,0	2,1	2,2	2,25	2,3	2,4	2,45	2,5	2,6	2,7	2,8	2,8	see Figure 3.2 [NDP]$\varepsilon_{c1}(^0/_{00}) = 0,7\, f_{cm}^{0,31} \leq 2,8$ [NDP]
ε_{cu1} (‰)	3,5									3,2	3,0	2,8	2,8	2,8	see Figure 3.2 for $f_{ck} \geq 50$ Mpa $\varepsilon_{cu1}(^0/_{00})=2,8+27[(98-f_{cm})/100]^4$
ε_{c2} (‰)	2,0									2,2	2,3	2,4	2, 5	2,6	see Figure 3.3 for $f_{ck} \geq 50$ Mpa $\varepsilon_{c2}(^0/_{00})=2,0+0,085(f_{ck}-50)^{0,53}$
ε_{cu2} (‰)	3,5									3,1	2,9	2,7	2,6	2,6	see Figure 3.3 for $f_{ck} \geq 50$ Mpa $\varepsilon_{cu2}(^0/_{00})=2,6+35[(90-f_{ck})/100]^4$
n	2,0									1,75	1,6	1,45	1,4	1,4	for $f_{ck} \geq 50$ Mpa $n=1,4+23,4[(90-f_{ck})/100]^4$
ε_{c3} (‰)	1,75									1,8	1,9	2,0	2,2	2,3	see Figure 3.4 for $f_{ck} \geq 50$ Mpa $\varepsilon_{c3}(^0/_{00})=1,75+0,55[(f_{ck}-50)/40]$
ε_{cu3} (‰)	3,5									3,1	2,9	2,7	2,6	2,6	see Figure 3.4 for $f_{ck} \geq 50$ Mpa $\varepsilon_{cu3}(^0/_{00})=2,6+35[(90-f_{ck})/100]^4$

Appendix B - Design Drawings

Drawing nr 1: Biaxial Frame Setup

Drawing nr 2: Bearing system 1

Drawing nr 2: Bearing system 2

Drawing nr 3: Bearing system 3 and 4

Drawing nr 3: Tension jaws

NR.	DATE	REVISIONS	C.ENG.	E.C.P.
0	YYYY/MM/DD	DISCRIPTION		
0	YYYY/MM/DD	DISCRIPTION		
0	YYYY/MM/DD	DISCRIPTION		
0	YYYY/MM/DD	DISCRIPTION		
0	YYYY/MM/DD	DISCRIPTION		
0	YYYY/MM/DD	DISCRIPTION		

DRAWN BY	DATE		
W Swanepoel	2009/09/16		
APPROVED BY ENGINEER	DATE		
Name	YYYY/MM/DD		
ARCHITECT	DATE		
Name	YYYY/MM/DD		

CLIENT

UNIVERSITY OF STELLENBOSCH

PROJECT DESCRIPTION

BIAXIAL BEHAVIOUR OF FIBRE REINFORCED CONCRETE

SCALE

-

DRAWING DESCRIPTION

FRAME DESIGN DETAILS

PLAN NR.

FINAL

REV. NR.

4

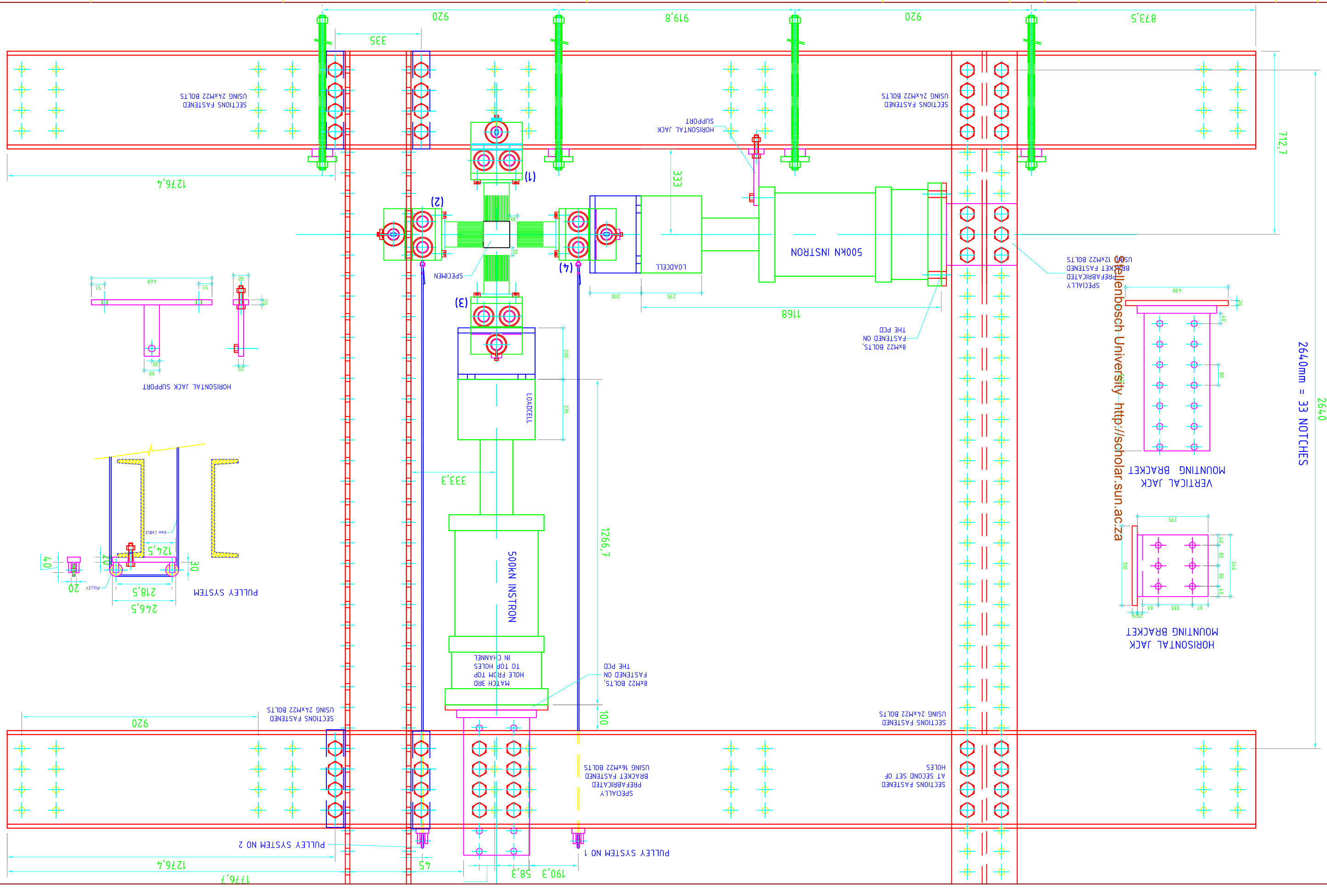

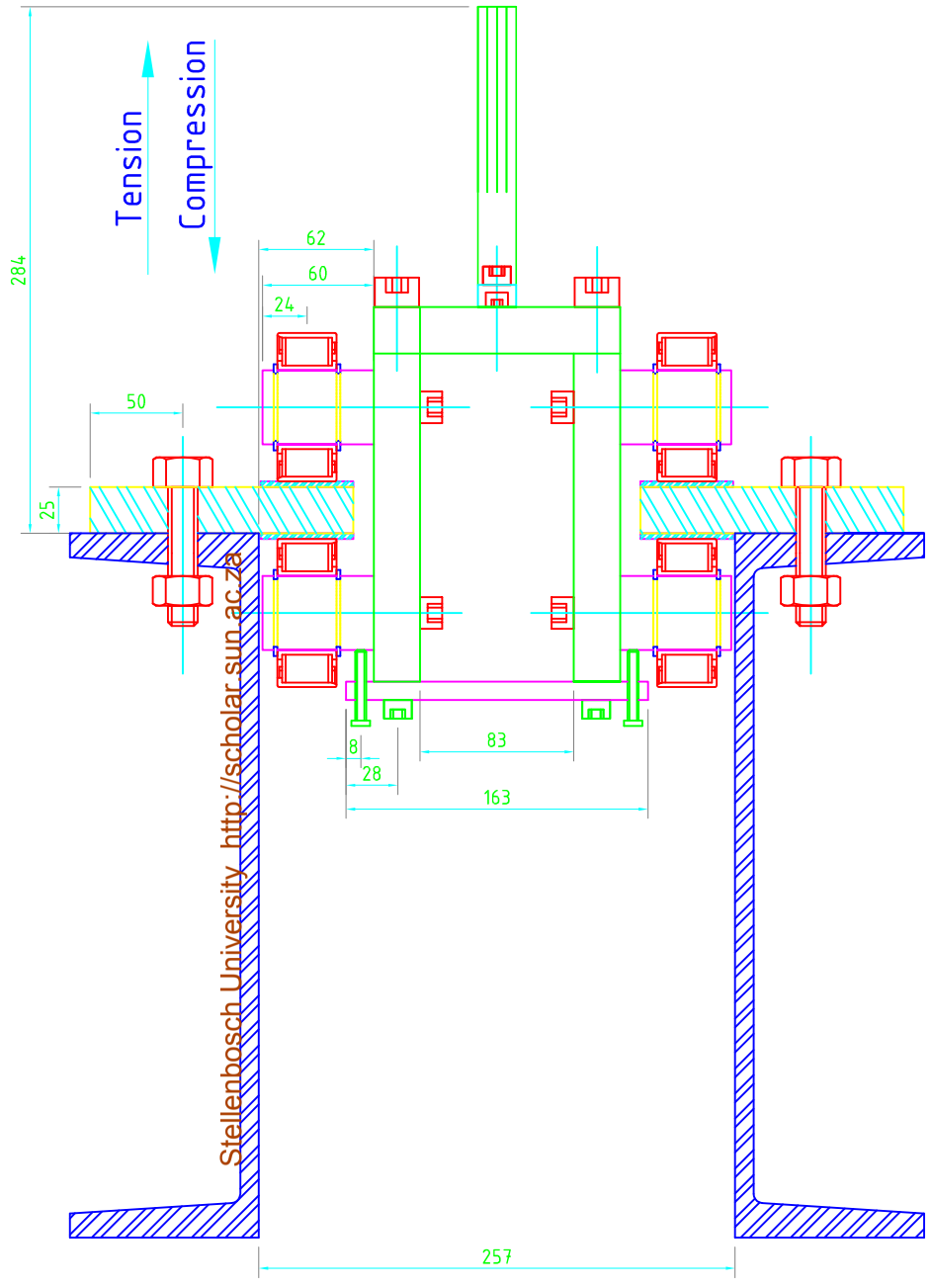

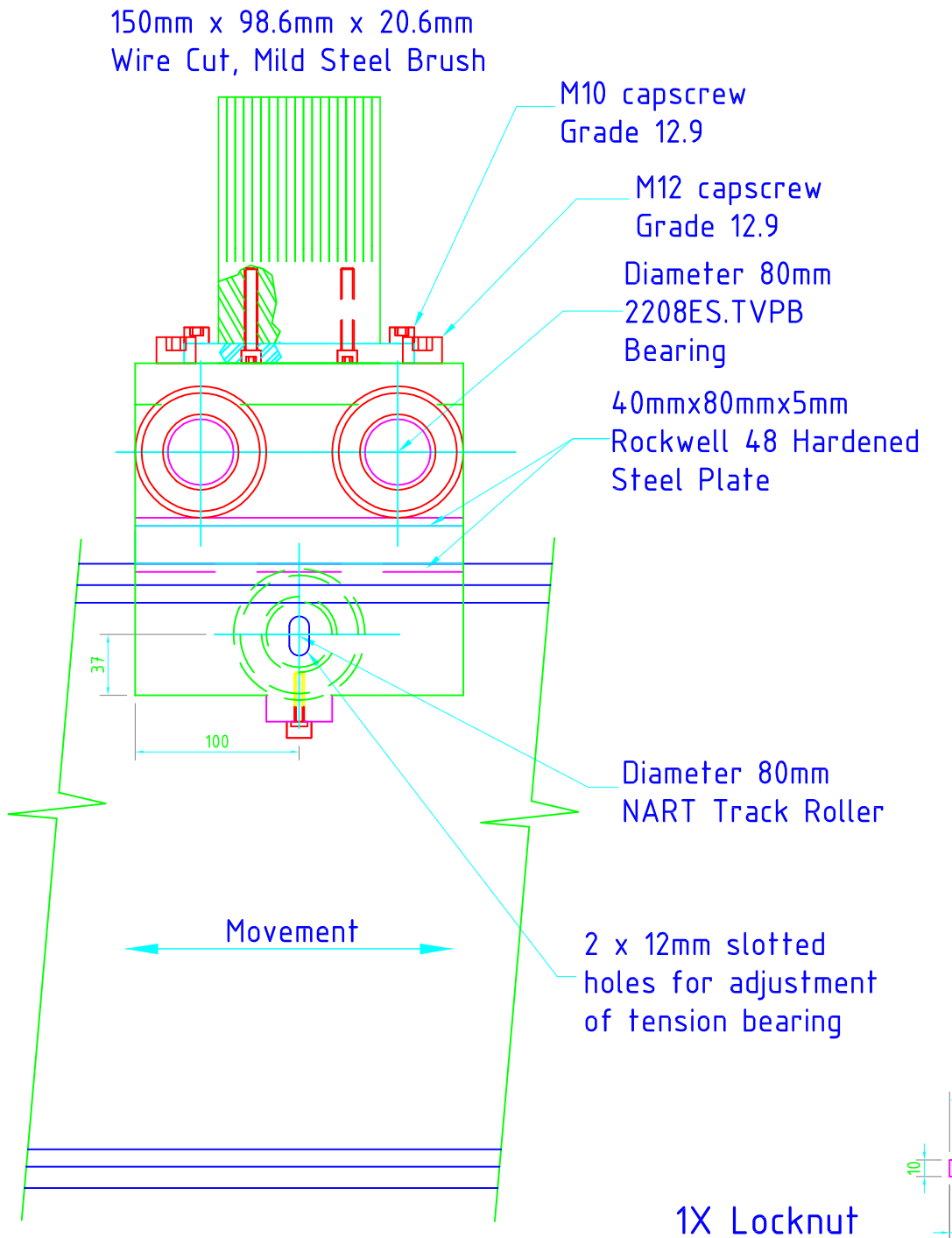

2X Bracket Side Plate

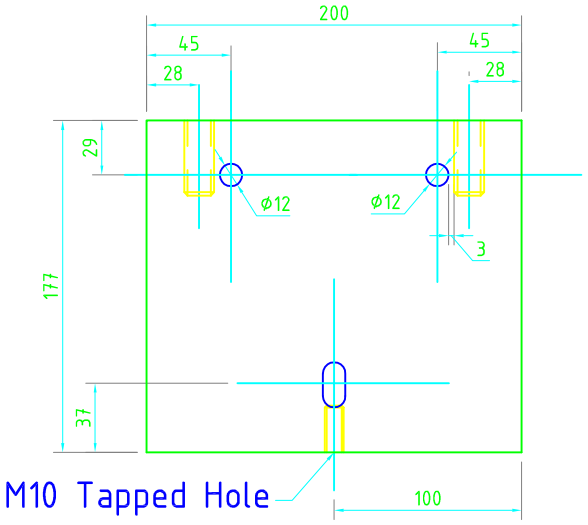

1X Bracket Face Plate

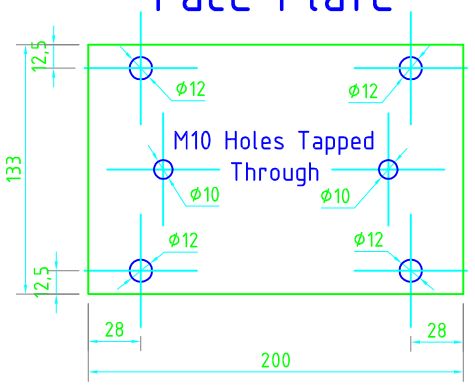

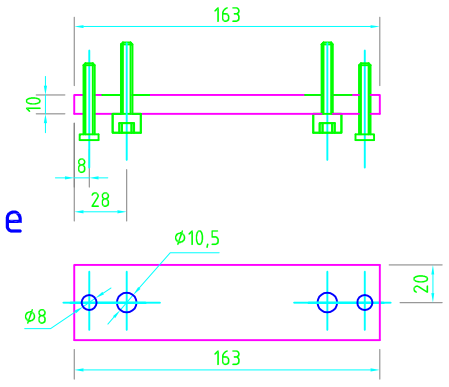

1X Locknut Mechanism Plate

6X Bearing Shaft

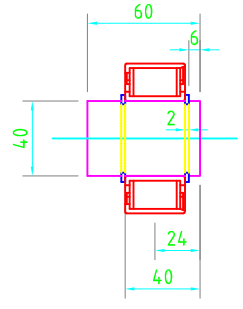

Bearing System No.1
(To Run on Bottom Two Tapered Flange Channel Sections)

NR.	DATE	REVISIONS	C.ENG.	E.C.P.
0	YYYY/MM/DD	DISCRIPTION		
0	YYYY/MM/DD	DISCRIPTION		
0	YYYY/MM/DD	DISCRIPTION		
0	YYYY/MM/DD	DISCRIPTION		
0	YYYY/MM/DD	DISCRIPTION		
0	YYYY/MM/DD	DISCRIPTION		

DRAWN BY — DATE: W Swanepoel — 2010/08/17
APPROVED BY ENGINEER — DATE: Name — YYYY/MM/DD
ARCHITECT — DATE: Name — YYYY/MM/DD

CLIENT: UNIVERSITY OF STELLENBOSCH

PROJECT DESCRIPTION: BIAXIAL BEHAVIOUR OF FIBRE REINFORCED CONCRETE

PLAN NR.: *FINAL*

REV. NR.: *6*

SCALE: -

DRAWING DESCRIPTION: BEARING SYSTEM No.1 DESIGN DETAILS

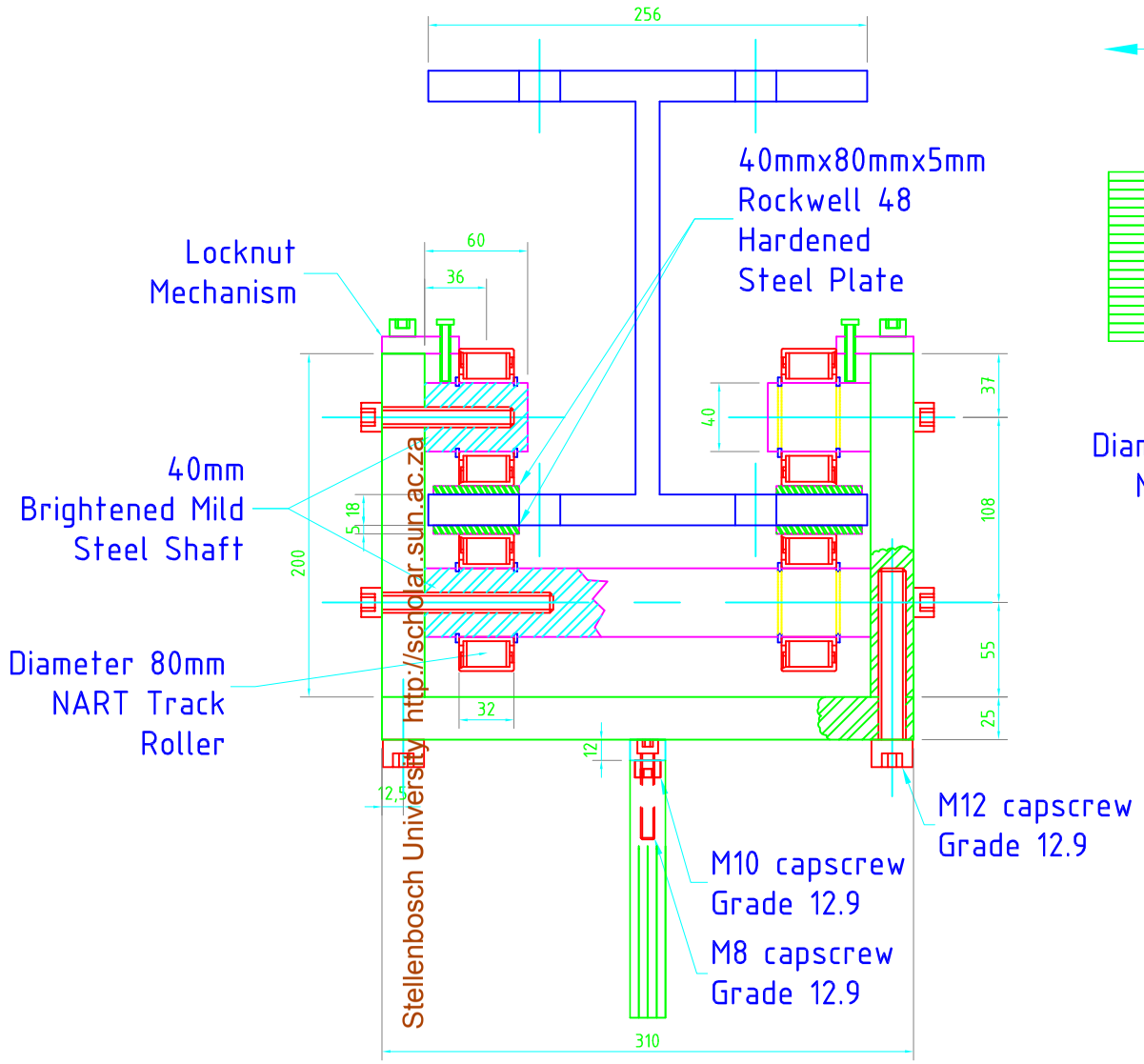

150mm x 98.6mm x 20.6mm
Wire Cut, Mild Steel Brush

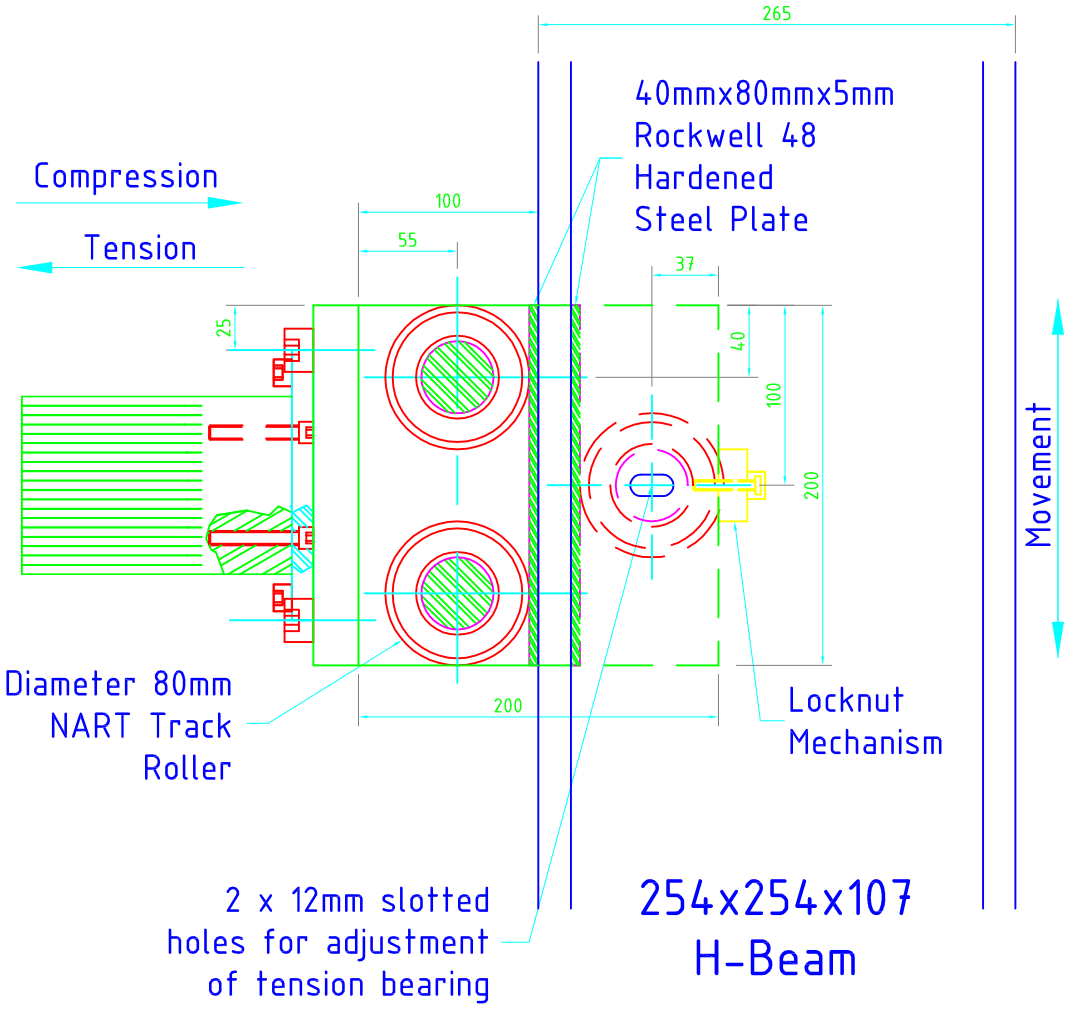

254x254x107
H-Beam

Movement

1X Bracket
Face Plate

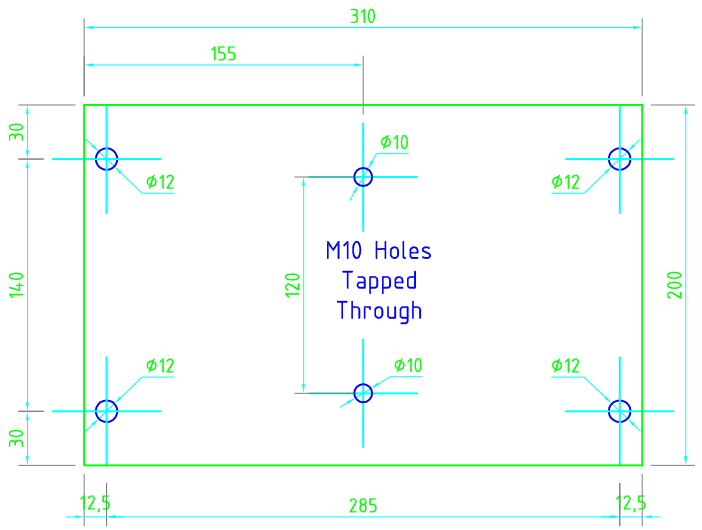

2X Bracket
Side Plate

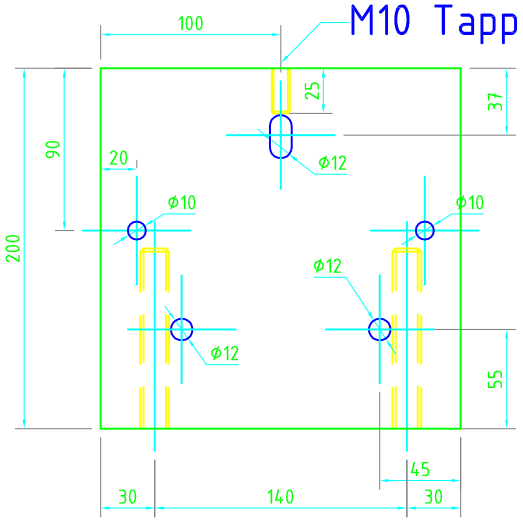

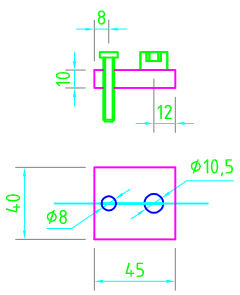

2X Locknut
Mechanism Plate

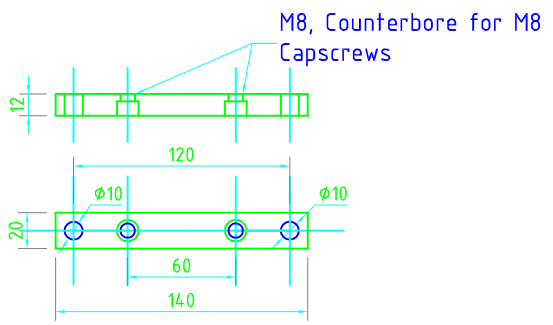

1X Keysteel Brush
Footpiece

Bearing System No.2
(To Run on Vertical 254x254x107 H-Beam)

NR.	DATE	REVISIONS	C.ENG.	E.C.P.
0	YYYY/MM/DD	DISCRIPTION		
0	YYYY/MM/DD	DISCRIPTION		
0	YYYY/MM/DD	DISCRIPTION		
0	YYYY/MM/DD	DISCRIPTION		
0	YYYY/MM/DD	DISCRIPTION		
0	YYYY/MM/DD	DISCRIPTION		

DRAWN BY — DATE: W Swanepoel — 2009/10/08
APPROVED BY ENGINEER — DATE: Name — YYYY/MM/DD
ARCHITECT — DATE: Name — YYYY/MM/DD

CLIENT: UNIVERSITY OF STELLENBOSCH

PROJECT DESCRIPTION: BIAXIAL BEHAVIOUR OF FIBRE REINFORCED CONCRETE

PLAN NR.: *FINAL*

REV. NR.: 4

SCALE: -

DRAWING DESCRIPTION: BEARING SYSTEM No. 2 DESIGN DETAILS

Made up
I-section
200x200x20

M10 Bolt
Grade 8.8

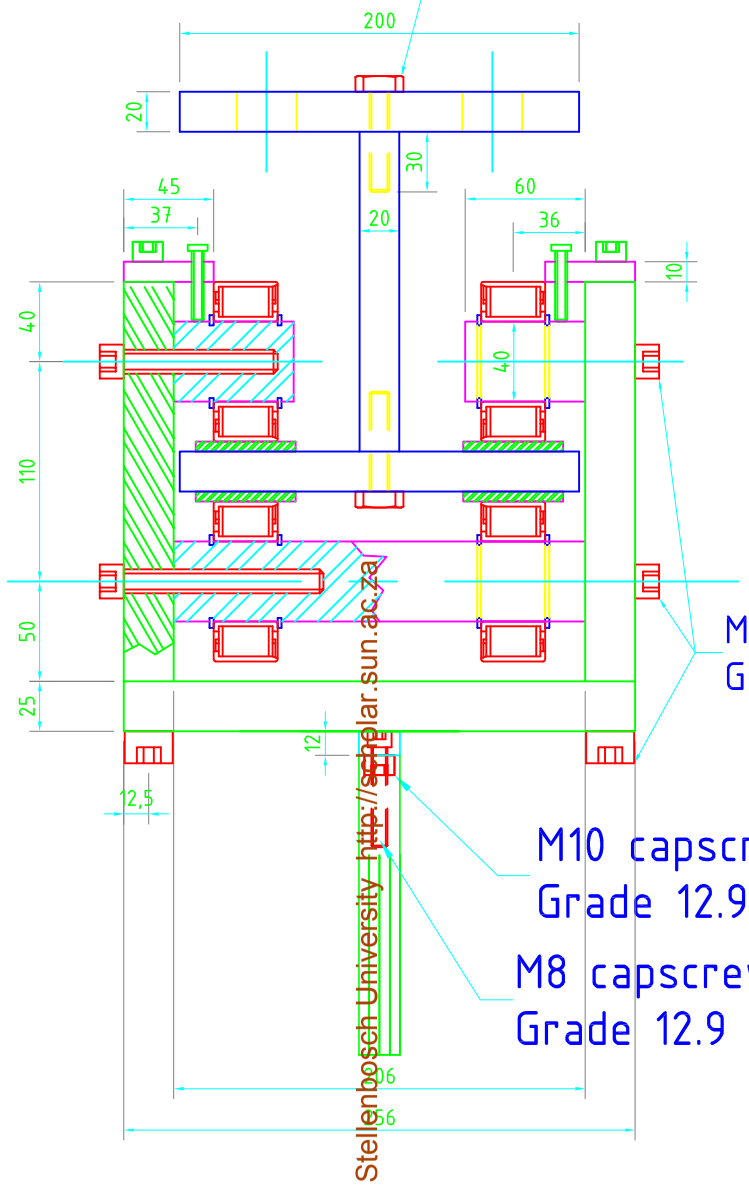

M12 capscrews
Grade 12.9

M10 capscrew
Grade 12.9

M8 capscrew
Grade 12.9

M10 capscrew
Grade 12.9
Countersunk

Movement

M20 Holes for
Bolts Fixing
Made up Section
onto Jack Face

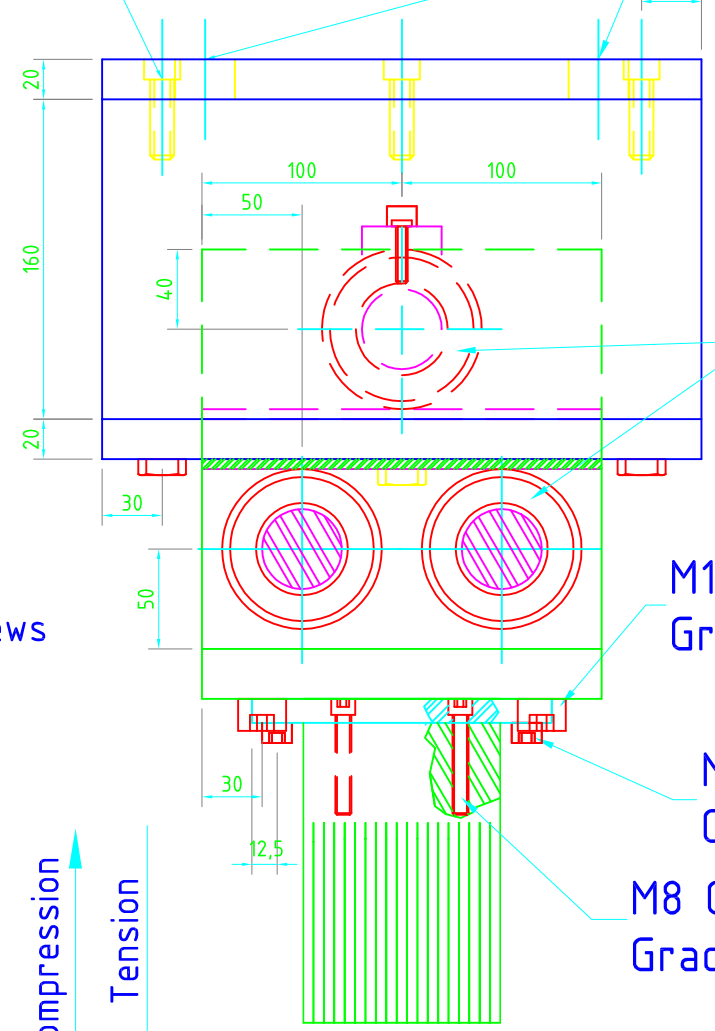

Diameter 80mm
NART Track
Roller

M12 Capscrews
Grade 12.9

M10 Capscrews
Grade 12.9

M8 Capscrews
Grade 12.9

Compression

Tension

150mm x 98.6mm x 20.6mm
Wire Cut, Mild Steel Brush

Bearing System No.3 & 4
(To Run on Made up H-Sections on Jack Faces)

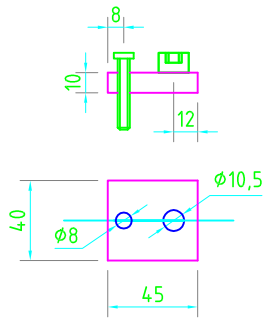

2X Locknut
Mechanism Plate

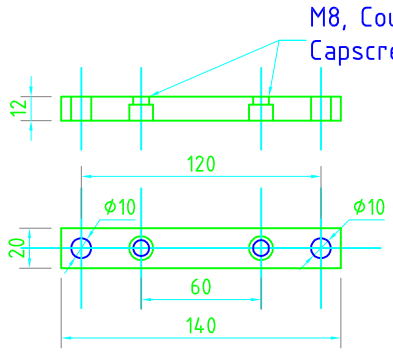

1X Keysteel Brush
Footpiece

4X Bracket
Side Plate

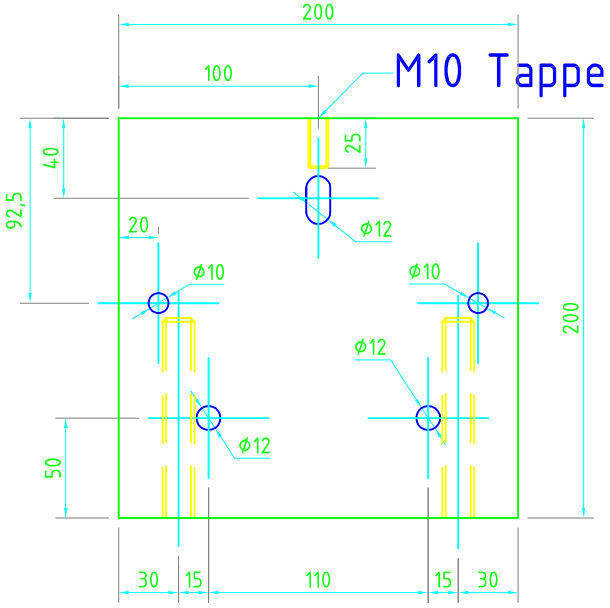

2X Bracket
Face Plate

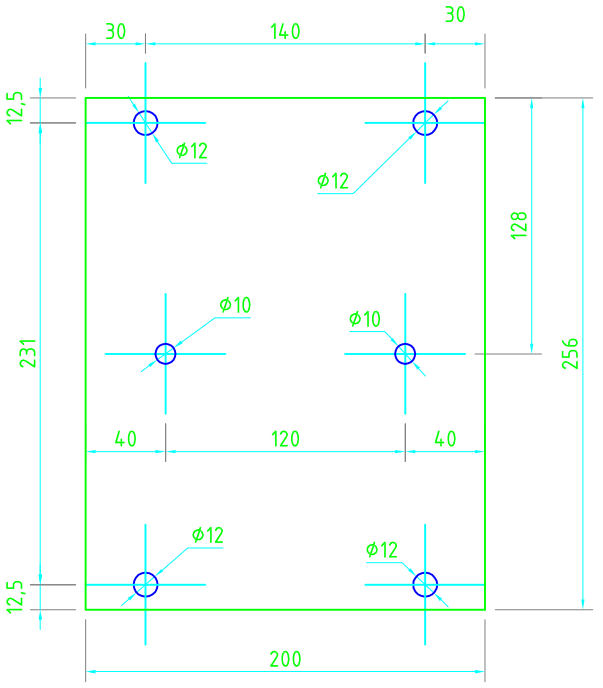

NR.	DATE	REVISIONS	C.ENG.	E.C.P.
0	YYYY/MM/DD	DISCRIPTION		
0	YYYY/MM/DD	DISCRIPTION		
0	YYYY/MM/DD	DISCRIPTION		
0	YYYY/MM/DD	DISCRIPTION		
0	YYYY/MM/DD	DISCRIPTION		
0	YYYY/MM/DD	DISCRIPTION		

DRAWN BY	DATE
W Swanepoel	2009/10/08
APPROVED BY ENGINEER	DATE
Name	YYYY/MM/DD
ARCHITECT	DATE
Name	YYYY/MM/DD

CLIENT: UNIVERSITY OF STELLENBOSCH

PROJECT DESCRIPTION: BIAXIAL BEHAVIOUR OF FIBRE REINFORCED CONCRETE

PLAN NR.: *FINAL*

REV. NR.: 4

SCALE: -

DRAWING DESCRIPTION: BEARING SYSTEMS 2&3 DESIGN DETAILS

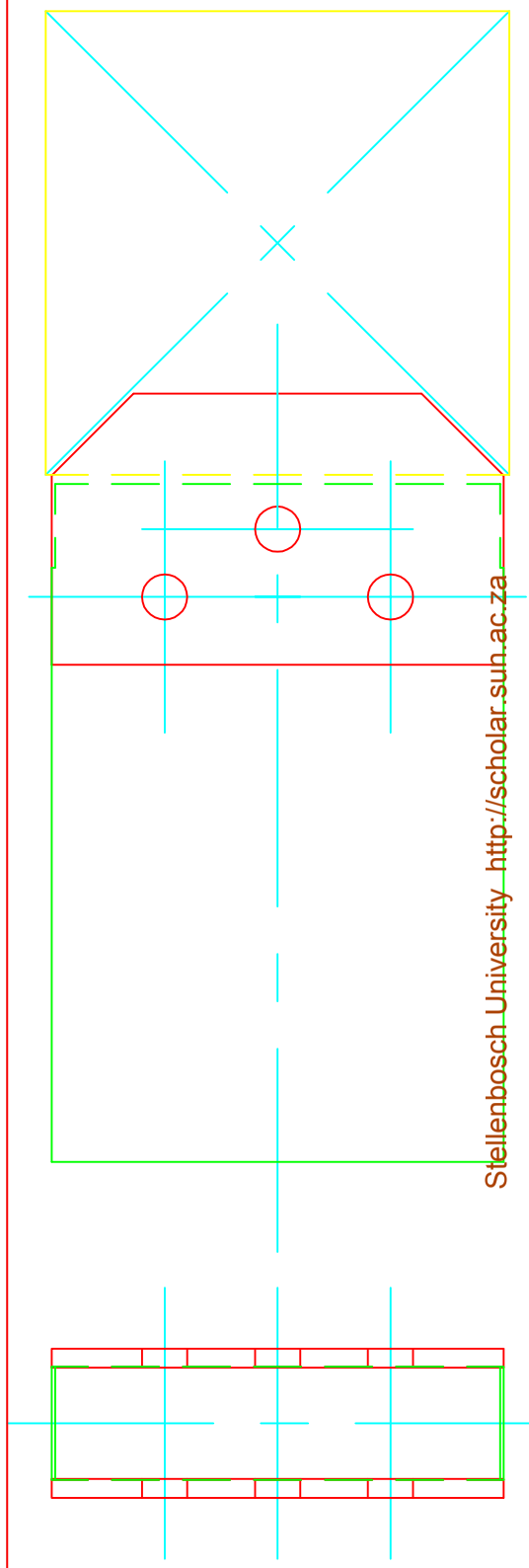

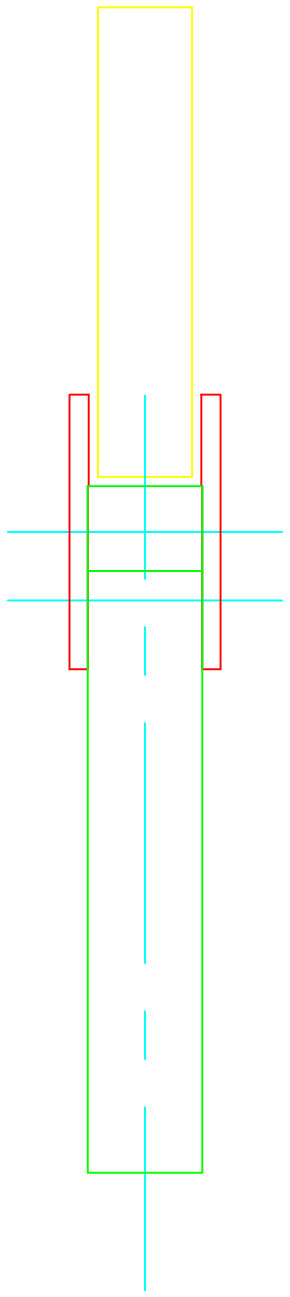

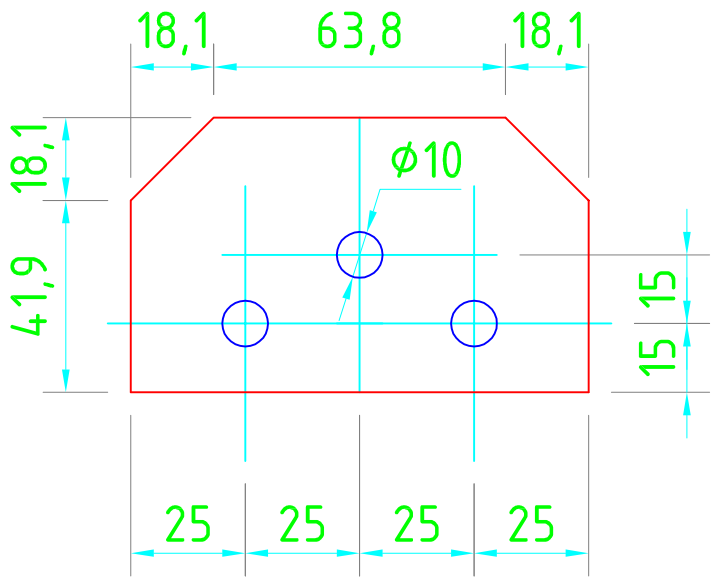

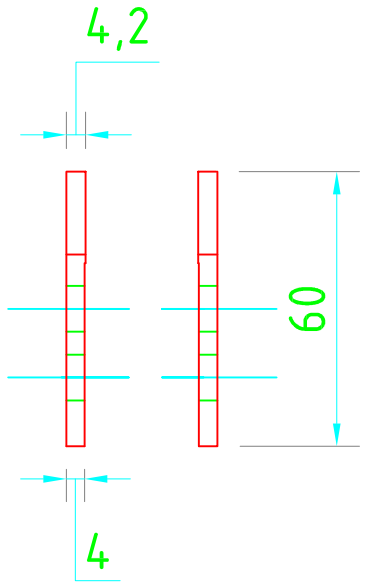

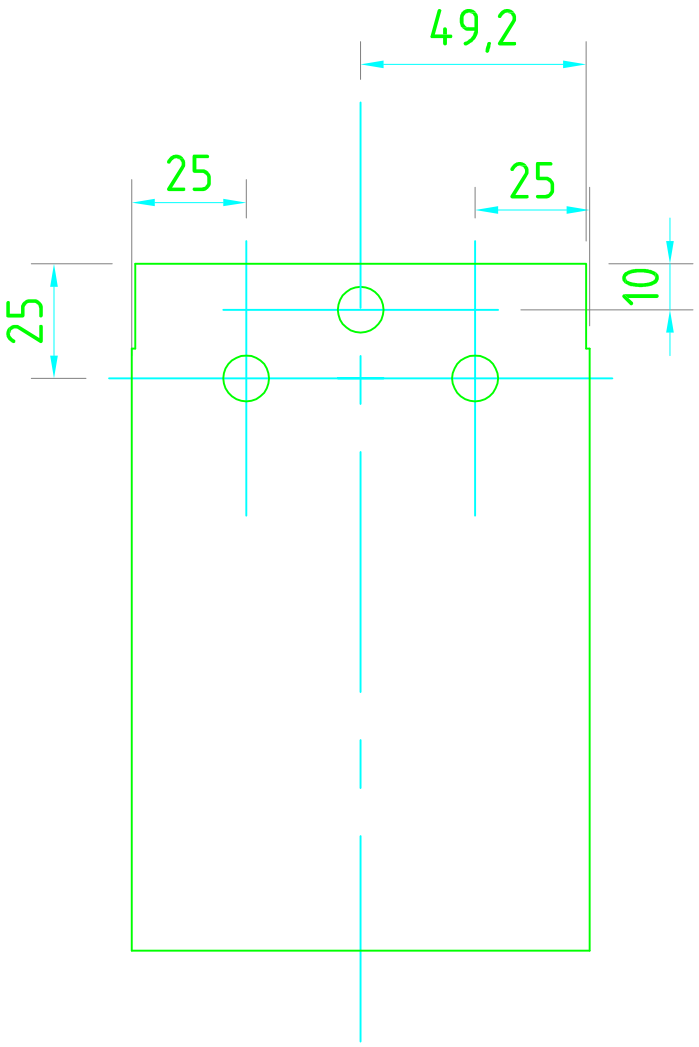

8 X STEEL PLATES TO BE BOLTED ONTO SIDES OF LOADING PLATENS

POSITIONS OF HOLES TO BE DRILLED INTO LOADING PLATENS

NR.	DATE	REVISIONS	C.ENG.	E.C.P.
0	YYYY/MM/DD	DISCRIPTION		
0	YYYY/MM/DD	DISCRIPTION		
0	YYYY/MM/DD	DISCRIPTION		
0	YYYY/MM/DD	DISCRIPTION		
0	YYYY/MM/DD	DISCRIPTION		
0	YYYY/MM/DD	DISCRIPTION		

DRAWN BY	DATE
W Swanepoel	2011/02/15
APPROVED BY ENGINEER	DATE
Name	YYYY/MM/DD
ARCHITECT	DATE
Name	YYYY/MM/DD

CLIENT: UNIVERSITY OF STELLENBOSCH

PROJECT DESCRIPTION: BIAXIAL BEHAVIOUR OF FIBRE REINFORCED CONCRETE

PLAN NR.: *FINAL*

REV. NR.: *0*

SCALE: -

DRAWING DESCRIPTION: TENSION TESTING LOADING PLATENS

Appendix C – Teflon Technical Information

CHEMSTIK® CF203 (Tygaflor 308A/03T)

CHEMFAB® CF203 is a highly competitive PTFE coated glass cloth. It provides good release properties over a wide range of applications.

Applications:

CHEMFAB® CF203 is typically used as a non-stik surface in applications where regular replacement is the norm.

Typical Properties	Unit	Value	Test Method
Base PTFE fabric weight:	g/mm²	130	FTMS 191A-5041
Base Thickness:	mm	0.070	FTMS 191A-5030
Adhesive Thickness:	mm	0.045	FTMS 191A-5030
180° Peel Adhesion Strength:	N/cm	5.3	ASTM D330-83
Tensile Strength:	N/cm	180 x 140	FTMS 191A-5102
Adhesive Type:	-	Silicone	-
Temperature Resistance:	°C	-73 TO +260	-
Standard Widths:	mm	1000	-

*Formerly **CF 700-3**, Tygaflor 308A.*

QUADRANT

Quadrant Chemplast Pty Ltd

Engineering Plastics for Heat & Corrosive Applications

52 Kraft Road, P.O. Box 8049 Elandsfontein Germiston Gauteng South Africa 1406
H/O Tel: (0)11 828 0950, H/O Fax: (0)11 828 0336 Reg. No: 1972/002265/07
Durban Branch Tel: (0)31 579 2377, Cape Town Branch Tel: (0)21 555 4596
E-mail: marketing@chemplast.co.za Web: www.quadrantchemplast.co.za

Appendix D – Epoxy Technical Information

Tests

Approval / Standards

European Technical Approvals for threaded rods:

European Technical Approval ETAG 001 Part 5 Option 7	
Galvanised anchor	Stainless steel anchor
EC Cert. 0679-CPD-0027	EC Cert. 0679-CPD-0028
ETA-05 / 103	ETA-05 / 104

Tested according to the ETAG001 TR023 for rebars

Testing according to ICC / ICBO standards.
ICC ES Legacy Report ESR-1382 Reissued December 1, 2006
Report Holder: Sika Corporation (USA)

Fire resistance:
Test report from the University of Brunswick
Report No. 3551/4926
Tests according DIN EN 1363-1 (ISO 834)

Product Data

Form

Colours

Part A: light green
Part B: black
Part A+B mixed: light grey

Packaging

300 ml standard cartridge, 12 per box.
Pallet: 60 boxes with 12 cartridges.

550 ml standard cartridge, 12 per box.
Pallet: 50 boxes with 12 cartridges.

Storage

Storage Conditions / Shelf-Life

15 months from date of production if stored properly in original unopened, sealed and undamaged packaging in cool and dry conditions at temperatures between +5°C and +20°C. Protect from direct sunlight.

All Sika AnchorFix®-2 cartridges have the expiry date printed on the label.

Technical Data

Density

Part A: 1.62 - 1.70 kg/l
Part B: 1.44 - 1.50 kg/l

1.60 - 1.68 kg/l (part A+B mixed)

Curing Speed

Temperature	Open Time T_{gel}	Curing Time T_{cur}
+20°C - +35°C	1 minute	40 minutes
+10°C - +20°C	4 minutes	70 minutes
+5°C - +10°C	8 minutes	100 minutes
0°C - +5°C	- *	180 minutes
-5°C - 0°C	- *	24 hours

*Min. cartridge temperature = +5°C

Sag Flow

Non-sag, even overhead.

Layer Thickness

3 mm max.

Appendix E – Biaxial testing results for SHCC

	Horizontal Force (kN)	Standard Deviation	Horiszontal Stress (MPa)	Vertical Force (kN)	Vertical Stress (MPa)
P1-1	-86.69		-40.32	-87.69	-40.79
P1-2			Test Failed		
P1-3			Test Failed		
Avg	-86.69	0	-40.32	-87.69	-40.79
P2-1	-46.20		-21.49	-79.30	-36.88
P2-2	-53.65		-24.95	-91.84	-42.72
P2-3	-51.98		-24.18	-89.11	-41.45
Avg	-50.61	1.817	-23.54	-86.75	-40.35
P3-1	-22.51		-10.47	-80.35	-37.37
P3-2	-27.45		-12.77	-100.11	-46.56
P3-3	-21.71		-10.10	-77.90	-36.23
Avg	-23.89	1.447	-11.11	-86.12	-40.06
P4-1	0.00		0.00	-70.90	-32.97
P4-2	0.00		0.00	-73.27	-34.08
P4-3	0.00		0.00	-76.71	-35.68
Avg		0	0.00	-73.63	-34.24
P5-1	-16.11		-7.49	3.70	1.72
P5-2	-14.03		-6.53	3.25	1.51
P5-3	-16.01		-7.45	3.65	1.70
Avg	-15.38	0.543	-7.15	3.53	1.64
P6-1	-7.11		-3.31	3.07	1.43
P6-2	-7.76		-3.61	2.78	1.29
P6-3			Test Failed		
Avg	-7.43	0.212	-3.46	2.93	1.36
P7-1	-3.48		-1.62	2.59	1.20
P7-2	-4.90		-2.28	3.43	1.60
P7-3	-4.72		-2.20	3.37	1.57
Avg	-4.37	0.360	-2.03	3.13	1.46
P8-1	-2.81		-1.31	2.74	1.27
P8-2	-3.06		-1.42	3.31	1.54
P8-3	-1.68		-0.78	2.48	1.15
Avg	-2.52	0.342	-1.17	2.84	1.32
P9-1	-1.97		-0.91	3.11	1.45
P9-2	-1.39		-0.64	3.02	1.40
P9-3			Test Failed		
Avg	-1.68	0.191	-0.78	3.06	1.43
P10-1	0.00		0.00	2.29	1.07
P10-2	0.00		0.00	1.61	0.75
P10-3	0.00		0.00	2.61	1.21
Avg		0	0.00	2.17	1.01
P11-1	1.18		0.55	1.03	0.48
P11-2	1.47		0.68	2.38	1.11
P11-3			Test Failed		
Avg	1.33	0.092	0.62	1.71	0.79
P12-1	2.35		1.09	2.62	1.22

P12-2	2.29		1.07	2.93	1.36
P12-3			Test Failed		
Avg	2.32	0.014	1.08	2.78	1.29
P13-1	3.68		1.71	2.42	1.12
P13-2	3.88		1.81	2.75	1.28
P13-3	3.40		1.58	2.43	1.13
Avg	3.65	0.115	1.70	2.53	1.18

Appendix F – Multiple Cracking Results for SHCC

	Multiple Cracking (Y/N)	Saturated (Y/N)	Comment
P1-1	Y	N	
P1-2	Test Failed		unsafe test
P1-3	Test Failed		unsafe test
P2-1	Y	N	
P2-2	Y	Y	saturated after crushing
P2-3	Y	N	
P3-1	Y	N	
P3-2	Y	N	
P3-3	Y	N	
P4-1	Y	N	
P4-2	Y	N	
P4-3	Y	N	
P5-1	Y	N	
P5-2	Y	N	
P5-3	Y	N	
P6-1	Y	N	
P6-2	N	N	
P6-3	Test Failed		epoxy-SHCC bond failed
P7-1	Y	N	
P7-2	Y	N	
P7-3	Y	N	
P8-1	Y	N	
P8-2	Y	N	
P8-3	N	N	
P9-1	Y	N	
P9-2	Y	N	
P9-3	Test Failed		epoxy-SHCC bond failed
P10-1	Y	N	
P10-2	Y	N	
P10-3	N	N	
P11-1	Y	N	
P11-2	Y	N	
P11-3	Test Failed		epoxy-SHCC bond failed
P12-1	Y	N	
P12-2	Y	N	
P12-3	Test Failed		epoxy-SHCC bond failed
P13-1	Y	N	
P13-2	Y	N	
P13-3	Y	N	very little